

# Biological and Biomimetic Formation and Organization of Magnetic Nanoparticles

Habilitationsschrift  
zur Erlangung der Lehrbefähigung  
für das Fach Chemie

vorgelegt dem Fakultätsrat der  
Mathematisch-Naturwissenschaftlichen Fakultät  
der Universität Potsdam

von

Dr. Damien Faivre

Geboren am 03.10.1977 in Saint Etienne, Frankreich

Präsident der Universität Potsdam

Prof. Oliver Günther, Ph.D.

Dekan der Mathematisch-Naturwissenschaftlichen Fakultät

Prof. Dr. Patrick O'Brien

Potsdam, den 29. April 2014

Gutachter:

1. Prof. Dr. Peter Fratzl
2. Prof. Dr. Joachim Bill
3. Prof. Dr. Hans Börner

This work is licensed under a Creative Commons License:  
Attribution – Noncommercial – No Derivatives 4.0 International  
To view a copy of this license visit  
<http://creativecommons.org/licenses/by-nc-nd/4.0/>

Published online at the  
Institutional Repository of the University of Potsdam:  
URL <http://opus.kobv.de/ubp/volltexte/2014/7202/>  
URN <urn:nbn:de:kobv:517-opus-72022>  
<http://nbn-resolving.de/urn:nbn:de:kobv:517-opus-72022>



## Acknowledgements

I want to start by a special thanks to those who have particularly guided me since my doctoral thesis. Dabei will ich mich chronologisch erst bei Dirk Schüler bedanken. Die Arbeit in der Gruppe war immer mit viel Freiheit verbunden, die weitere Schritte zur wissenschaftlichen Selbständigkeit ermöglichten. Seine Unterstützung nach meinem Weggang aus Bremen hat sich in eine freundliche Kooperation gewandelt, was ich sehr zu schätzen weiß. Ich möchte deswegen auch seinen jetzigen Mitarbeitern für ihre Zusammenarbeit danken.

Pour Peter Fratzl quelques mots en français comme une évidence pour souligner l'aspect multiculturel au-delà de l'aspect scientifique. Je ne saurai jamais assez le remercier pour m'avoir permis d'établir mon propre groupe au sein de son département. Ses connaissances multidisciplinaires font un vrai régal des courtes réunions que nous pouvons avoir et créer une atmosphère absolument unique dans l'aile de l'institut dédiée aux biomatériaux.

Allen ehemaligen Bremer Mitarbeitern der Arbeitsgruppe „magnetotaktische Bakterien“ danke ich für die gute Arbeitsatmosphäre. Insbesondere möchte ich mich bei André Scheffel und Claus Lang bedanken, auch weil Ihre Begegnungen das dortige Leben weit über die Wissenschaft beeinflusst hat. Umso schöner dass André jetzt im benachbarten Pflanzen Institut einen weiteren Teil seines Werdegangs begonnen hat. Also warten wir jetzt noch auf Claus.

The twin acknowledgements go to the colleagues from Potsdam. A special thanks to the Italian connection (Luca) as producer of nice EM images and supplier of delicious food. I cannot forget the BESSY twins (Stefan and Chenghao) for their never-ending help and support online and on-site. Danke auch an Kerstin, Ulrike, Nadine und die weitere Kollegen aus der Verwaltung, die unser Leben leichter machen. A special thanks to John for the corrections of the work during vacation time. Sorry for those I forget although they e.g. put my nerves on tension (do you recognize yourself Admir).

Of course I cannot forget all the co-workers of the group, from those coming for an internship, the bachelor and master students or the "old Diplomand" version, the doctoral students and the post docs, and of course the technicians; from those of the first hours sharing the difficult beginning time but also the poster prize of the HMI conference (Anna, Jens, Manu, Sanjiv) to those of the present "golden age" (Agata, Carmen, Christophe, Christopher, Jens (still), Livnat, Marc, Maria, Mathieu, Peter, Teresa, Victoria) sharing the generous support of the ERC funding in addition of the already generous support of the MPG. In the meantime André, Antje, Cécile, Gauthier, Janet, Karin, Kathleen, Kevin, Muriel, and Paul have joined the groups and joined other horizons, closed-by in the department, the institute, Potsdam or Berlin or further away in the USA and even in Peru...

This work could not have been performed without the help of numerous collaborators and support. Just to name a few I need to mention Ann Hirt as a work on magnetite need a specialist of magnetism on the side. Einen besonderen Dank an Stefan Klumpp, der die theoretische Arbeit verständlicher macht. Grazie Pierpaolo, merci aux anciens collègues parisiens qui ont continué à collaborer, Danke Hans Börner und die Kollegen von der Uni Potsdam (Peter Strauch und auch André Laschewsky), die diese Arbeit ermöglicht haben. Natürlich auch einen speziellen Dank an den Gutachtern und Mitglied der Gutachterkommission.

Finalement, je remercie ma famille. Merci à mes parents de m'avoir fourni les bases pour en arriver jusque là. N'hésitez pas à parler de BESSY à Nathalie... même si elle n'hésite pas « à mettre la main à

la pâte » pour rechercher des bactéries dans des lacs aux couleurs bizarres et dans les conditions les plus rocambolesques comme le prouve la photo ci-dessous. Merci à Pablo, Ewa et Fiona pour les jeux, les câlins et les fous-rires qui font parfois oublier que les bactéries ne poussent pas et les étudiants n'écrivent pas assez vite.





## Table of Contents

1. Scientific context and motivation.....	1
2. Biomineralization and use of magnetosomes.....	5
2.1. Ultrastructure of magnetosome.....	6
2.2. Magnetosomes biomineralization.....	11
2.2.1. Mechanism and dynamics of magnetosome formation .....	11
2.2.2. MmsF control magnetosome dimension .....	19
2.3. Magnetosome chains .....	23
2.3.1. Magnetite crystal orientation in magnetosome chains .....	23
2.3.2. Magnetic aspects of the magnetosome assembly .....	30
2.3.3. Genetic aspects of the magnetosome assembly.....	33
2.3.4. Magnetism vs. genetics: Determining the main factor in magnetosome assembly using <i>in silico</i> mutants.....	39
2.4. Magneto-aerotaxis .....	45
3. Synthetic formation and use of magnetite .....	51
3.1. Magnetite formation “in the beaker” .....	51
3.1.1. The mechanism of magnetite nucleation and growth in the absence of additives.....	51
3.1.2. MamP enables magnetite formation from ferrous iron alone.....	60
3.1.3. An alternative strategy to identify biological determinants .....	61
3.2. Magnetite assembly: actuated nanodevices.....	70
3.2.1. Microdevices based on whole magnetotactic bacteria.....	71
3.2.2. Bottom-up approaches based on the assembly of magnetic nanoparticles.....	73
4. Summary and Outlook.....	79
5. References.....	83
6. List of publications.....	95
6.1. Publications in scientific journals or magazines .....	95
6.2. Book chapters.....	104





## Abstract

Biological materials such as bone, shells and wood have been used by humans since the most ancient times. Recent scientific studies have started to shed light on the reason why: these biologically formed materials have remarkable properties. This is especially surprising since they are formed under physiological conditions i.e. at ambient temperatures and pressures, and with commonplace constituents. Nature thus not only provides us with inspiration for designing new materials but also teaches us how to use soft molecules such as proteins to tune interparticle and external forces to structure and assemble simple building blocks into functional entities. Magnetotactic bacteria and their chain of magnetosomes represent a striking example of such an accomplishment where a very simple living organism precisely controls the properties of inorganics via organics and at the nanometer-scale to form a single magnetic dipole that passively orients the cell in the Earth magnetic field lines.

The magnetosomes formed by the bacteria are of special interest since magnetic iron oxide nanoparticles have generated tremendous research interest in the last decade due to a multitude of bio- and nanotechnological applications and their role in magnetoreception. As a paradigm of nanomaterials, their magnetic properties of magnetic nanoparticles are depending on their size. In the particular case of the mineral magnetite, the magnetic properties of the nanoparticles range from superparamagnetic (from ca. 2 to ca. 25 nm), to ferrimagnetic single-domain (from ca. 25 to ca. 100 nm) and to bigger multi-domain (larger than about 100 nm) structures. The intermediate size range has long remained inaccessible *via* chemical routes but the magnetotactic bacteria commonly formed magnetite particles of that size.

In my group, we have developed a biological and a bio-inspired research based on the magnetotactic bacteria. This research combines the recent developments of nanoscale engineering in the chemical science, the latest advances in molecular biology together with modern progresses in physical analysis. My research thus focuses at the interface between chemistry, materials science, physics, and biology to understand how biological systems synthesize, organize and use minerals, and to apply the design principles to sustainably form hierarchical materials with controlled properties that can be used e.g. as magnetically directed nanodevices towards applications in sensing, actuating, and transport.

In this thesis, I thus first present how magnetotactic bacteria intracellularly form magnetosomes and assemble these particles in chains. I developed an assay, where cells can be switched back and forth from magnetic to non-magnetic states. This in particular has enabled me and my group to study the dynamics of magnetosome formation and of magnetosome chain formation. We found that the magnetosomes nucleate very rapidly

within minutes whereas they assemble to form the chain within hours. Magnetosome formation necessitates iron uptake from the environment as ferrous or ferric ions. The transport of the ions within the cell leads to the formation of a ferritin-like intermediate, which subsequently is transported and transformed within the magnetosome organelle in a ferrihydrite-like precursor. Finally, magnetite crystals eventually nucleate and growth toward their mature dimension as shown by a combination of spectroscopic and microscopic techniques.

In addition, I show that the magnetosome assembly displays hierarchically ordered nano- and microstructures over several levels, enabling the coordinated alignment and motility of entire populations of cells. The magnetosomes are indeed composed of structurally pure magnetite biomineralized within the magnetosome vesicle or organelle. The organelles are partly composed of proteins, which role is crucial for the properties of the magnetosomes. As an example, we have shown how the protein MmsF is involved in the control of magnetosome size and morphology. These magnetosomes then self-assemble into more complex structures. We have shown by 2D X-ray diffraction that the magnetosome particles are aligned along the same direction in the magnetosome chain and that this direction is species-specific. We propose that the cells do not need to control crystal orientation to impose such a patterning but that controlling the direction of elongation of the crystals leads to the same results of crystal orientation. We then show how magnetic properties of the nascent magnetosome influence the alignment of the particles, and how the proteins MamJ and MamK coordinate this assembly. We propose a theoretical approach, which suggests that biological forces are more important than physical ones for the chain formation. All these studies thus show how magnetosome formation and organization are under strict biological control, which is associated with unprecedented material properties. Finally, we show that the magnetosome chain enables the cells to find their preferred oxygen conditions if the magnetic field is present.

The synthetic part of this work show how the understanding of the design principles of magnetosome formation enabled me and my research group to performed biomimetic synthesis of magnetite particles within the highly desired size range of 25 to 100 nm. Nucleation and growth of such particles are based on aggregation of iron colloids termed primary particles as imaged by cryo-high resolution TEM. We propose a theoretical model based on the treatment of the primary particles as dilute species that explains our experimental findings and in particular the fact that no amorphous bulk phase was detected between the poorly ordered primary particles and the final crystalline magnetite. I then show how biological or biomimetic additives can influence the pathway of magnetite formation or control the properties of the formed particles. In particular, I show that MamP, a so-called magnetochrome proteins involved in the magnetosome formation *in vivo*, enables the *in vitro* formation of magnetite nanoparticles exclusively from ferrous iron and thus control the redox state of the process. Negatively charged additives, such as MamJ or

polyglutamic acid, retard magnetite nucleation *in vitro*, probably by interacting with the iron ions. Other additives such as e.g. polyarginine, a positively charged polypeptides, can be used to control the colloidal stability of stable-single domain sized nanoparticles probably by sterically screening the magnetic properties and / or by interaction with the primary particles we identified.

Finally, I show how we can “glue” magnetic nanoparticles to form propellers that can be actuated and swim with the help of external magnetic fields. We propose a simple theory to explain the observed movement. We can use the theoretical framework to design experimental conditions to sort out the propellers depending on their size and effectively confirm this prediction experimentally. Thereby, we could image propellers with size down to 290 nm in their longer dimension, much smaller than what perform so far.



# 1. Scientific context and motivation

Biomineralization is simply defined by the formation of minerals by organisms (Lowenstam, 1981). There is a large variety of such biomineralizing organisms and also of the type of minerals they can form (Baeuerlein, 2007). Organism – mineral – function relationships include e.g. calcium phosphate in bone in a multitude of organisms (Baeuerlein and Epple, 2007); calcium carbonate in crustacean shell or spine assuring protection from predator species (Seto et al., 2012); diatoms, which are eukaryotic microalgae producing structured silica cell walls (Scheffel et al., 2011); and different organisms such as salmon using magnetic iron oxide particles to orient themselves in the Earth magnetic field (Eder et al., 2012) just to name a few examples of the recent literature.

The minerals, rather than pure inorganic materials, are often organic – inorganic composites and the small fraction of organics plays a crucial role for their formation as well as properties (Dunlop and Fratzl, 2010; Weiner and Addadi, 2011). Biomineralizing organisms and their biominerals are an ideal couple to study the interface between nanomaterials and biological systems, as they offer this merging of organics and inorganics. Moreover, even simple organisms are not only able to synthesize mineral inclusions; they can also precisely tune the properties of the particles they form and arrange them in a way to achieve a given function, thereby gaining a particular advantage with respect to their non-biomineralizing counterparts (Baeuerlein, 2007). These materials are indeed also typically hierarchical structured, and this assembly is of major importance for their magnetic, optical or mechanical properties and in turn for their use by the organism (Fratzl and Weinkamer, 2007).

The formation of these biominerals is not only for biologists a fascinating example of how living organisms can translate genetic blueprint information into complex inorganic and cellular structures but is also a source of inspiration for chemists and material scientists that so far form such functional materials under conditions that are not accessible to these organisms (Baeuerlein and Behrens, 2007; Fratzl, 2007; Mann, 2001). It is indeed now widely recognized that the nanoscale phenomena and particularly the forces and interactions exerted between crystals and biological components have to be understood before this knowledge can be used for later hierarchical assembly that eventually will enable the production of hybrid materials with high functionalities. Thus, in the last years, a field of biomimetics has developed to study the interaction between organics and inorganics with model systems in a more physico-chemical and synthetic context. Biomimetics is not simply doing a direct copy of natural systems, but rather aims at applying the observed key design principles for the desired materials property.

An example of a desired materials property is found in the size- and morphology-dependent magnetic properties observed in iron oxide nanoparticles. In the context of nanosciences and nanotechnologies, magnetic nanoparticles are indeed key components to the development of novel

nano- and biotechnological applications (Lang et al., 2007; Laurent et al., 2008; Lu et al., 2007; Reddy et al., 2012). There is in fact an increasing need for such functionalized particles in medicine for advanced diagnosis and therapies such as magnetic drug targeting or molecular imaging. Besides these direct applications, magnetic nanocrystals are also the current base component of microrobots (Dreyfus et al., 2005; Martel, 2012; Peyer et al., 2013; Sitti, 2009; Zhang et al., 2011).

In the specific case of the magnetic iron oxide magnetite, the particles smaller than 25 nm are called superparamagnetic (SP) and do not possess a permanent magnetic signal (Dunlop and Özdemir, 1997). The particles between roughly 25 and 100 nm do have a permanent magnetic dipole and are called stable single domain (SSD) particles. Particles larger than this are called multidomain (MD). MD particles also exhibit a permanent magnetic signal, which however is no longer as strong as that of the SSD particles when correlated to their dimension (Dunlop and Özdemir, 1997). The applications listed above are however critically dependent on the particles size. If the dimension of magnetite nanoparticles can easily be tuned in the 5 to 20 nm range, larger particles and specifically SSD particles could not be synthetically obtained under atmospheric conditions when this work was started (Lang et al., 2007).

There is however a biomineralizing organism able to form such particles: the magnetotactic bacteria (MTB) (Blakemore, 1975; Blakemore, 1982). MTB are found in aquatic environments. They are prokaryotes exhibiting a diversity with respect to morphology, physiology and phylogeny (Bazylinski and Schübbe, 2007; Faivre and Schüler, 2008; Lefèvre and Bazylinski, 2013) with the common feature being their magnetic organelle referred to as magnetosome (Gorby et al., 1988). Magnetosomes typically are the combination of a magnetite (Frankel et al., 1979) or greigite (Mann et al., 1990) particle embedded in a membrane that are assembled in chain(s) within a bacterium. This construction passively aligns the cells along magnetic field lines. On the surface of the Earth, these magnetic field lines have a component pointing downward, which enable the cells to actively swim towards micro-oxygenated regions usually found slightly below the sediment sublayers of aquatic environments (Bazylinski and Frankel, 2004; Frankel et al., 1997; Frankel et al., 2007). The research interests in these organisms span from biotechnology with possible applications in immunoassays, cell separation, drug delivery, hyperthermia or contrast agent in MRI (Hartung et al., 2007; Lang et al., 2007; Matsunaga et al., 2007) to geology as the magnetosomes were proposed to be biomarkers for the life on Mars (Friedmann et al., 2001; Kopp and Kirschvink, 2008; Weiss et al., 2004b) and from biology as the degree of complexity found in the chain assembly where initially supposed to be eukaryotic-specific (Carballido-Lopez, 2006; Komeili, 2007a) to magnetism and chemistry (Baumgartner and Faivre, 2011; Bennet et al., 2012; Carillo et al., 2012; Körnig and Faivre, 2012).

Magnetotactic bacteria excel where the human are still stumbling: the self-assembly of nanobuilding blocks. Such a level of organization in bacteria – from the control of magnetosome crystallinity, to the growth of ferromagnetic single-domain crystal with strain-specific morphology and to the cytoskeleton extending from cell pole to cell pole and on which the magnetosomes can anchor and align (Körnig and Faivre, 2012) – was still beyond expectation just a decade ago before researchers discovered that actin-like filaments are not eukaryotic-cell-specific but can also be found in bacteria (Carballido-Lopez, 2006). It was recently shown that the genes involved in the magnetosome formation were clustered in the so-called magnetosome genomic island (Komeili, 2012; Schüler, 2008), and that about 20 genes were sufficient to form the magnetic inclusions (Lohße et al., 2011; Murat et al., 2012). However when only these 20 genes are expressed instead of the whole magnetosome island, the particles however no longer resemble that of the wild-type cells (Lohße et

al., 2011; Murat et al., 2012). The production of the bacterial magnetic assembly starts from the uptake of iron ions from the surrounding environment to trigger the nucleation and growth of magnetic nanoparticles and the fully operational chain is found when the mature magnetosomes align along the magnetosome filament (Faivre et al., 2007). These very simple microorganisms, MTB, can therefore inspire a multitude of bottom up approaches for the fabrication of structures by self-assembly (Bennet et al., 2012).

The research program presented in the following pages started in January 2005 as a Marie Curie Fellow at the Max Planck Institute of Marine Microbiology in the group of Dirk Schüler. At the time, I already planned to focus on the iron physiology as well as on the magnetosome development *in vivo*, and to study the role of overexpressed proteins *in vitro*. This research line was too ambitious for a single researcher but could find an interested ear to be continued and expanded at the Max Planck institute of Colloids and Interfaces when Peter Fratzl offered me the opportunity to start my own group in August 2007. Since then, the group has slowly but surely grown around its initial objectives:

- The study of biomineralization in magnetotactic bacteria to understand how magnetosomes are formed and arranged in chains. Specifically we aimed at defining what are the molecular players determining the size and the morphology of the magnetosomes and those which, together with physical forces control their organization.
- The application of the knowledge we can gain from the biological system to develop particles with dedicated properties that can in turn be used to build hierarchical materials in a biomimetic fashion *in vitro*, especially under sustainable conditions. We specifically focus on the formation of magnetic swimming nanocarriers.
- The development of analytical tools and methods to study the swimming and tactic characteristics of magnetotactic bacteria and to control the motion of the swimming magnetic nanodevices we prepare. Specifically, we need a multimodal optical set-up working under control magnetic environment as well as microfluidic cells to constrain the physiological environment in which the samples are observed.

The next chapters are presenting my main achievements and that of my research group in these scientific directions. I start by presenting the results we obtained on the biological aspects of magnetosome formation and assembly in chapter 2. We were the initiators of presenting the bacteria as hierarchical structures and we developed physico-chemical technics to study the organisms at all length-scales and hierarchical levels. Our results in particular indicate that the cell are able to form pure magnetite to control the ultrastructure of its magnetic inclusions; that a particular gene, *mmsF*, is of critical importance for the control of the magnetosome size; that biological forces in a collaborative effort with physical forces are guiding the magnetosome chain assembly and that the magnetosomes are all oriented the same way in the chain. We finally show in this chapter how magnetotaxis is indeed a magnetically-refined aerotaxis. Chapter 3 summarizes our effort on the biomimetic aspects. Here, we discovered how SSD magnetite particles could be crystallized under physiological conditions and studied how specific additives impact the formation of the particles. I highlight the role of MamP as iron redox controller and of polyarginine as colloidal stabilizer. I finally present how the magnetic particles we synthesized can be aggregated to form magnetic nanopropellers in a random fashion but with surprising properties. In the outlook, we discuss how these results are important for the field and why they could produce very promising applications in the near future.





## **2. Biomineralization and use of magnetosomes**

Considering the bacteria as an assembly of structures at different levels started when we described the particles and the chain as entities with different functions. Before I joined the biomaterials department in 2007, such a vision, or description of the bacteria was not used at all. In this chapter, I thus describe how the bacteria are hierarchically structured (Figure 1), how this structuring is physically and / or biologically achieved, and what are the physical effects on each level of hierarchy. This description is purely based on experimental and theoretical studies I was involved in. On some aspects, our effort coincides with the major effort in the field, as for the ultrastructural characterization, and in other, as for the molecular work on genes and proteins involved in magnetosome formation, we rather help colleagues to characterize new bacterial strains while using e.g. high resolution X-ray diffraction techniques.

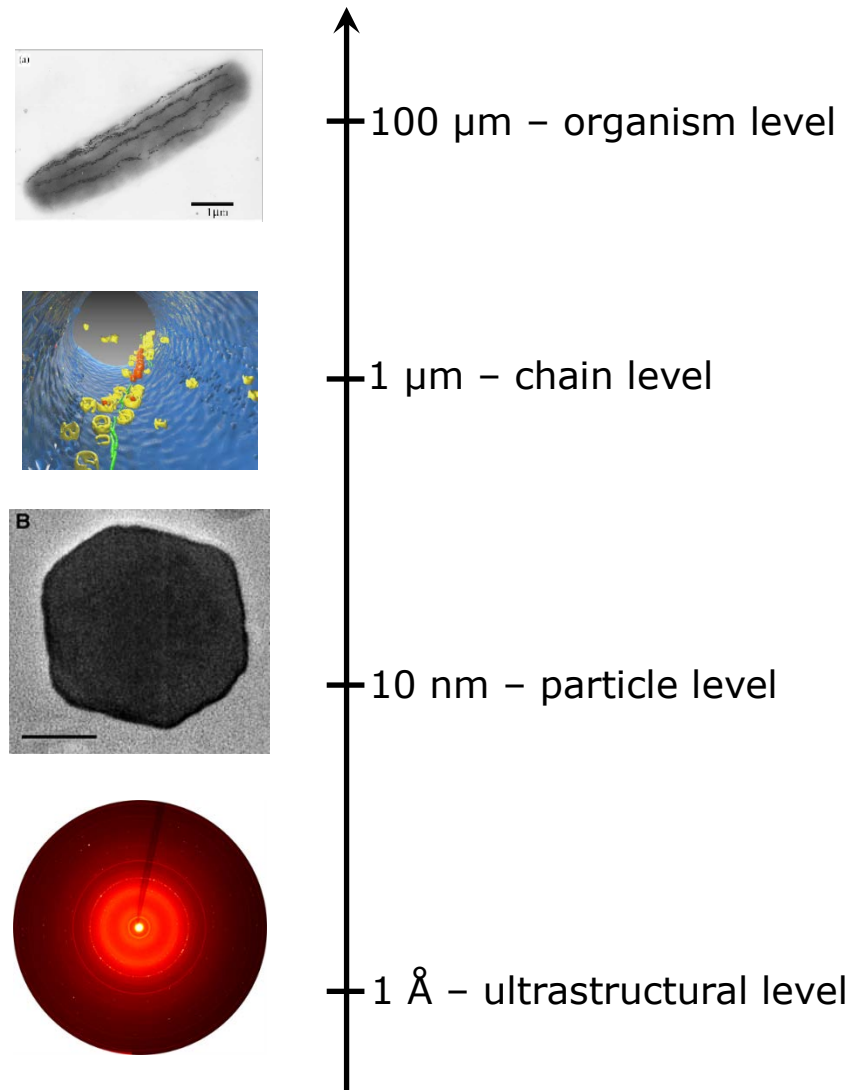


Figure 1: hierarchical structuring observed in magnetotactic bacteria and associated length scales. The different levels are presented in the text.

I begin with the astonishing ultrastructural purity of magnetosomes. Then I show how the bacteria first form and then control the size and morphology of the magnetosomes and how these impacts the magnetic properties of the cells. I subsequently describe the dynamics of magnetosome chain formation. Finally, the chains are also used as magnetic guide for the cellular movements within the Earth magnetic field lines.

## 2.1. Ultrastructure of magnetosome

The interest of biologists initially focused towards the understanding of the molecular players that control the formation of magnetosomes (Schüler, 1999). Later, interest in cell biology highlighted another hierarchical level, namely how the organelles themselves were formed and assembled (Komeili, 2007b). In parallel, a long-standing debate concerning the structural perfection of

magnetosomes at the Angstrom level and the possible presence of maghemite ( $\gamma\text{-Fe}_2\text{O}_3$ ) remained unsolved (Faivre et al., 2007; Frankel et al., 1983; Mann et al., 1984; Matsuda et al., 1983). This was at least partly due to the limited precision of electron diffraction with respect to lattice parameter determination that prevented detailed quantitative comparison between different biogenic magnetite particles and their synthetic counterparts.

With the advancement of analytical techniques and in particular the development of high power light sources at synchrotrons, even extremely small variations in lattice parameters became measurable. The group of Emil Zolotoyabko at Technion (Israel Institute of Technology) in particular paved the way and studied biominerals by high resolution X-ray diffraction (HRXRD). They showed in pioneering work in the mid-2000 that biogenic aragonite (Pokroy et al., 2004) and calcite (Pokroy et al., 2006a; Pokroy et al., 2006b) exhibited anisotropic lattice distortions when compared to analogous abiotic crystals.

Profiting from our favored access to the department Beamline ( $\mu\text{SPOT}$  Beamline at the BESSY II synchrotron of the Helmholtz Zentrum für Materialien, Berlin) dedicated towards XRD, we decided to precisely characterize the micro-structure of biogenic magnetite and used the dedicated high-resolution powder-XRD set-up to measure lattice parameters of nano-sized magnetite. This required long development in order to reach the necessary precision as presented in the diploma thesis of Manuel Schmitz (Schmitz, 2010). The process is summarized in Figure 2. Briefly, a dedicated sample holder was designed in order to have identical sample to detector distance between different samples. Then, an internal standard (quartz from the national institute of standard and technology (<http://www.nist.gov/>)) was used to calibrate the magnetite peaks.

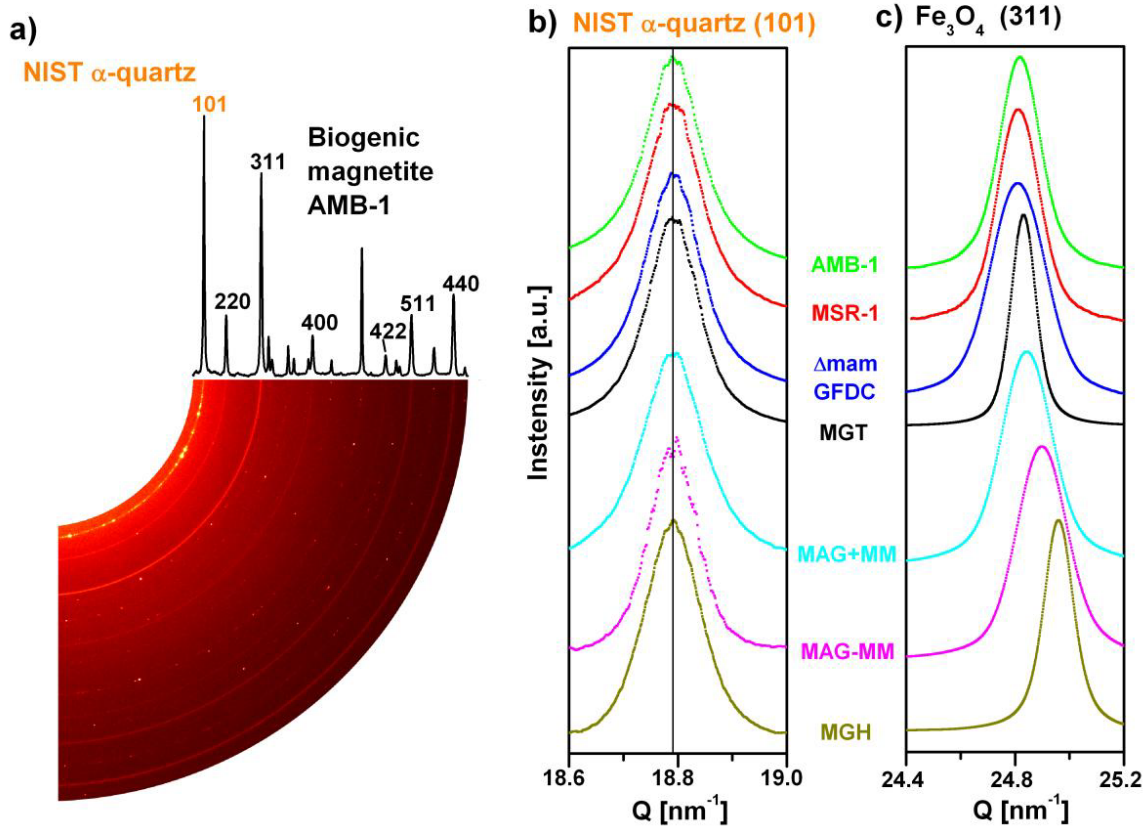


Figure 2: a) Exemplary 90° sector of the diffraction pattern of whole AMB-1 cells to visualize the azimuthal integration. Analyzed magnetite peaks and calibration peak (NIST  $\alpha$ -quartz) indexed b)  $\alpha$ -quartz (101) calibration peaks of different biogenic and abiotic magnetite/ maghemite samples. All peaks calibrated to  $Q=18.7910\text{nm}^{-1}$  c) most intensive (311) reflex of all analyzed samples. Remarkable peak shift between biogenic magnetite in cell solution samples (AMB-1, MSR-1 and  $\Delta\text{mamGFDC}$ ) compared to isolated magnetosomal magnetite (MAG+MM and MAG-MM).

Once the set-up was established, we could measure the following samples: whole cells of *Magnetospirillum gryphiswaldense* (strain MSR-1), *M. magneticum* (strain AMB-1) and  $\Delta\text{mamGFDC}$ , a deletion mutant of *M. gryphiswaldense* with altered crystallite size (Scheffel et al., 2008), detergent-treated MSR-1 magnetosomes (Lang and Schüler, 2008), and abiotic reference magnetite and maghemite, the final two samples being used for comparison. The results reported in Figure 3 were published as part of the post-doctoral work of Anna Fischer (Fischer et al., 2011). Our measurements revealed that the measured lattice parameters were similar for the bacterial samples (around  $8.396\text{ \AA}$ ) (Table 1) and comparable with the literature value of stoichiometric magnetite ( $a = 8.3969 \pm 0.0008\text{ \AA}$ ) (Fleet, 1984). In contrast, the magnetosomes isolated from the bacteria, but still protected by their magnetosome membrane, exhibited a smaller lattice parameter ( $a_{\text{a MAG+MM}} = 8.3875 \pm 0.0009\text{ \AA}$ ), which is comparable to that of our reference synthetic magnetite ( $a_{\text{a MGT}} = 8.3907 \pm 0.0009\text{ \AA}$ ). Finally, the treated magnetosomes, also lacking the magnetosome membrane, presented an even smaller lattice parameter ( $a_{\text{a MAG-MM}} = 8.3687 \pm 0.0014\text{ \AA}$ ), representing an intermediate step to maghemite ( $a_{\text{a MGH}} = 8.3470 \pm 0.0010\text{ \AA}$ ) (Table 1 and Figure 3).

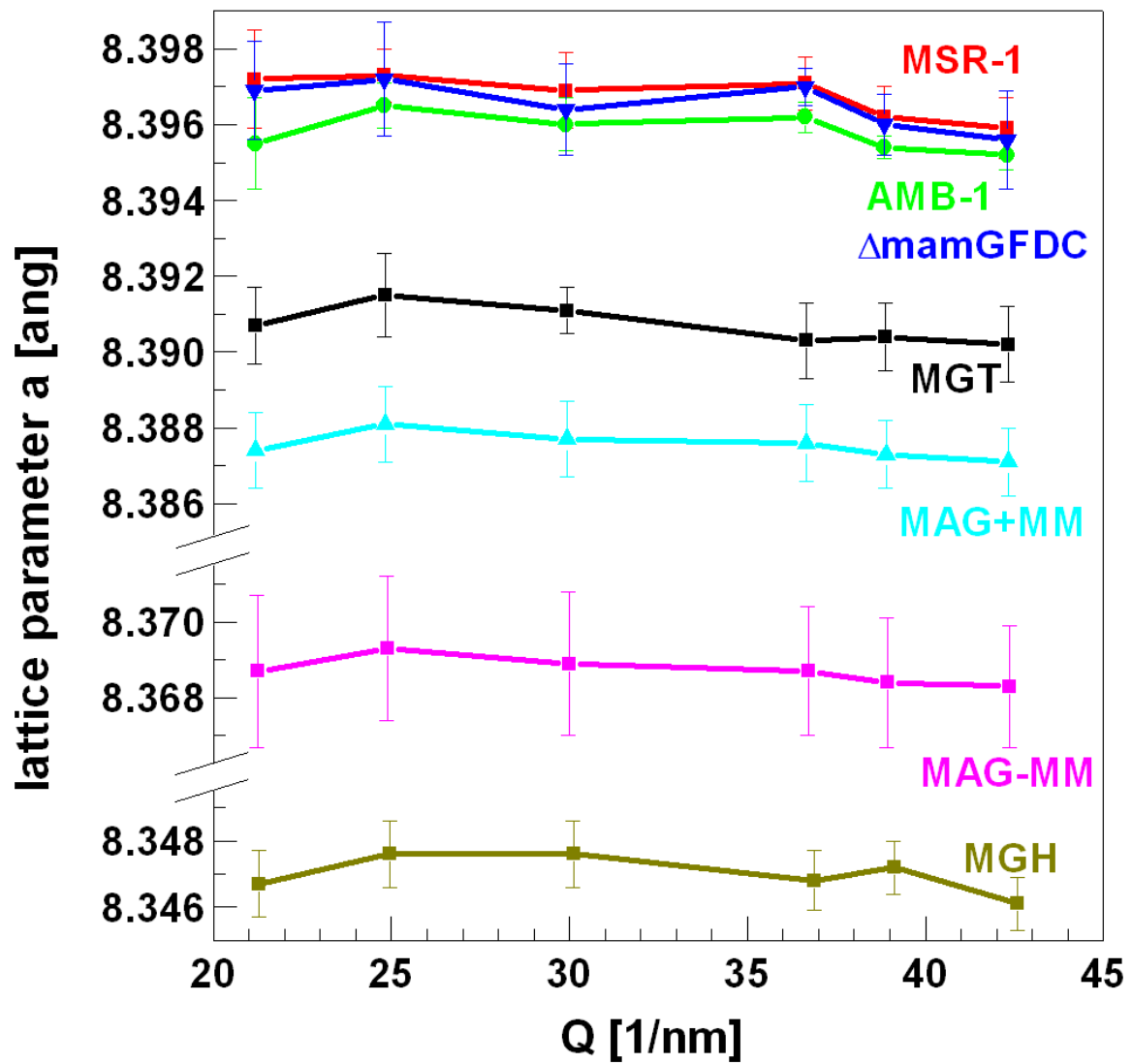


Figure 3: Translation of the observed peak positions into lattice parameter edge length  $a$  of the cubic magnetite / maghemite unit cell: Explicit higher lattice parameter for whole cell samples compared to MGT reference is observable. Isolation of magnetosomal magnetite from cells is accompanied by strong decrease of unit cell edge length (MAG+MM), even more pronounced if magnetosomal membrane is solubilized. A maghemitization of the former nearly stoichiometric biogenic magnetite seems reasonable.

**Table 1: Lattice parameter  $a$  determined for each diffraction peak, averaged lattice parameter  $a_a$ , particle size  $PS$  determined by XRD and by TEM (maximum of the distribution) for each sample. Difference in magnetosome dimensions between particles in the bacteria.**

Sample	(220)	(311)	(400)	(422)	(511)	(440)	$a_a$ [Å]	St. Dev [Å]	$PS_{XRD}$ [nm]	$PS_{TEM}$ [nm]
MSR-1	8.3983	8.3981	8.3979	8.3975	8.3971	8.3968	8.3968	0.0009	44	40
	8.3958	8.3971	8.3968	8.3975	8.3963	8.3957				
	8.3975	8.3967	8.3960	8.3962	8.3954	8.3953				
AMB	8.3969	8.3972	-	8.3966	8.3957	8.3956	8.3958	0.0007	44	45
	8.3949	8.3959	8.3956	8.3958	8.3951	8.3948				
	8.3948	8.3965	8.3965	8.3963	8.3955	8.3953				
$\Delta m_{GFD C}$	8.3960	8.3973	8.3955	8.3967	8.3954	8.3957	8.3965	0.0013	31	25
	-	8.3957	-	-	8.3965	8.3942				
	8.3979	8.3987	8.3973	8.3974	-	8.3968				
MAG+MM	8.3886	8.3892	8.3889	8.3888	8.3884	8.3881	8.3875	0.0009	33	35
	8.3868	8.3876	8.3872	8.3872	8.3868	8.3867				
	8.3868	8.3874	8.3871	8.3870	8.3867	8.3866				
MAG-MM	8.3673	8.3679	8.3676	8.3675	8.3672	8.3671	8.3687	0.0014	33	35
	8.3701	8.3706	8.3702	8.3699	8.3696	8.3694				
	-	-	-	-	-	-				
MGT	8.3916	8.3921	8.3915	8.3912	8.3911	8.3911	8.3907	0.0009	-	300-
	8.3896	8.3903	8.3904	8.3892	8.3894	8.3890				700
	8.3910	8.3921	8.3913	8.3905	8.3907	8.3904				
MGH	8.3458	8.3467	8.3466	8.3459	8.3464	8.3453	8.3470	0.0010	-	100-
	8.3467	8.3475	8.3475	8.3467	8.3472	8.3460				200
	8.3478	8.3486	8.3486	8.3478	8.3481	8.3469				

Typical explanations for such lattice parameter variations include the surface stress effect in nanoparticles (Bremholm et al., 2009), changes in composition (Readman and Oreilly, 1972) or the presence of intracrystalline proteins in ceramic crystallites (Pokroy et al., 2006a). In our case, only stoichiometric effects could explain the observed difference (Fischer et al., 2011). Oxidation of magnetite to maghemite indeed easily takes place at low temperatures by solid-state reaction *via* intermediate z-oxidation state (Dunlop and Özdemir, 1997). While the inverse spinel structure and the face-centered cubic unit cell are conserved, maghemitization results in a lattice parameter decrease. This reduction is induced by the creation of vacancies in the iron lattice and the change in Goldschmidt radius from 0.83 to 0.67 Å, as Fe(II) is oxidized to Fe(III) (Dunlop and Özdemir, 1997).

The lattice parameter of the bacterial magnetite fits perfectly with stoichiometric magnetite (Fleet, 1984), whereas that of the reference sample reveals slight oxidation (Figure 3). This result is not surprising since Fe(II) can easily be oxidized to Fe(III) under environmental atmospheric conditions.

The observed structural purity can also be expressed in term of magnetism and could thus be correlated to the functional properties of the magnetosomes in magnetotactic bacteria. Stoichiometric magnetite is indeed ferrimagnetic and it is the mineral with the highest magnetic moment (ca. 4  $\mu_B$ ) as compared to other iron oxides. Maghemitization diminishes the resulting saturation moment to a value of ca. 3  $\mu_B$  for maghemite (Dunlop and Özdemir, 1997). By fitting the experimental saturation moment  $M_s(z)$ , obtained from the literature (Dunlop and Özdemir, 1997), with a second order polynomial function (best fit), we obtained a saturation moment of 3.86  $\mu_B$  for the reference abiotic magnetite (Fischer et al., 2011). This corresponds to a loss of saturation moment of 4.1 % compared to the stoichiometric magnetite formed by the bacteria. We therefore speculated that magnetotactic bacteria might optimize their functionality at the Angstrom-level by facing the challenging task of synthesizing and maintaining the structure of stoichiometric magnetite (Fischer et al., 2011).

## 2.2. Magnetosomes biomineralization

### 2.2.1. Mechanism and dynamics of magnetosome formation

Magnetotactic bacteria were originally recognized (Blakemore, 1975) and isolated (Maratea and Blakemore, 1981; Schüler and Köhler, 1992) based on their magnetic properties and thus on the presence of magnetosomes. However, even if it was known before the beginning of this work that a non-magnetic state could exist due to the external scavenging of any iron source (Schüler and Baeuerlein, 1996) or the presence of elevated oxygen concentration in the medium (Schüler and Baeuerlein, 1998), no studies on chain or magnetosome formation based on a non-magnetic state that were also able to differentiate mineralizing from physiological iron were to be found in the literature.

I thus first had to develop a cell-suspension assay, where the bacteria are able to mineralize the magnetosome but no longer divide (Faivre et al., 2007; Faivre et al., 2008). Once this set up was established, we could look at the physico-chemical (Baumgartner et al., 2013c; Faivre et al., 2007; Faivre et al., 2008) as well as other aspects of magnetosome and chain formation as developed in the

following chapters. In particular, we studied the individual steps of the mechanism and dynamics of magnetosome and of magnetosome chain development, with a special focus on the early steps of magnetite formation. This work was commenced during my post-doctoral research stay in Bremen and continued in Potsdam.

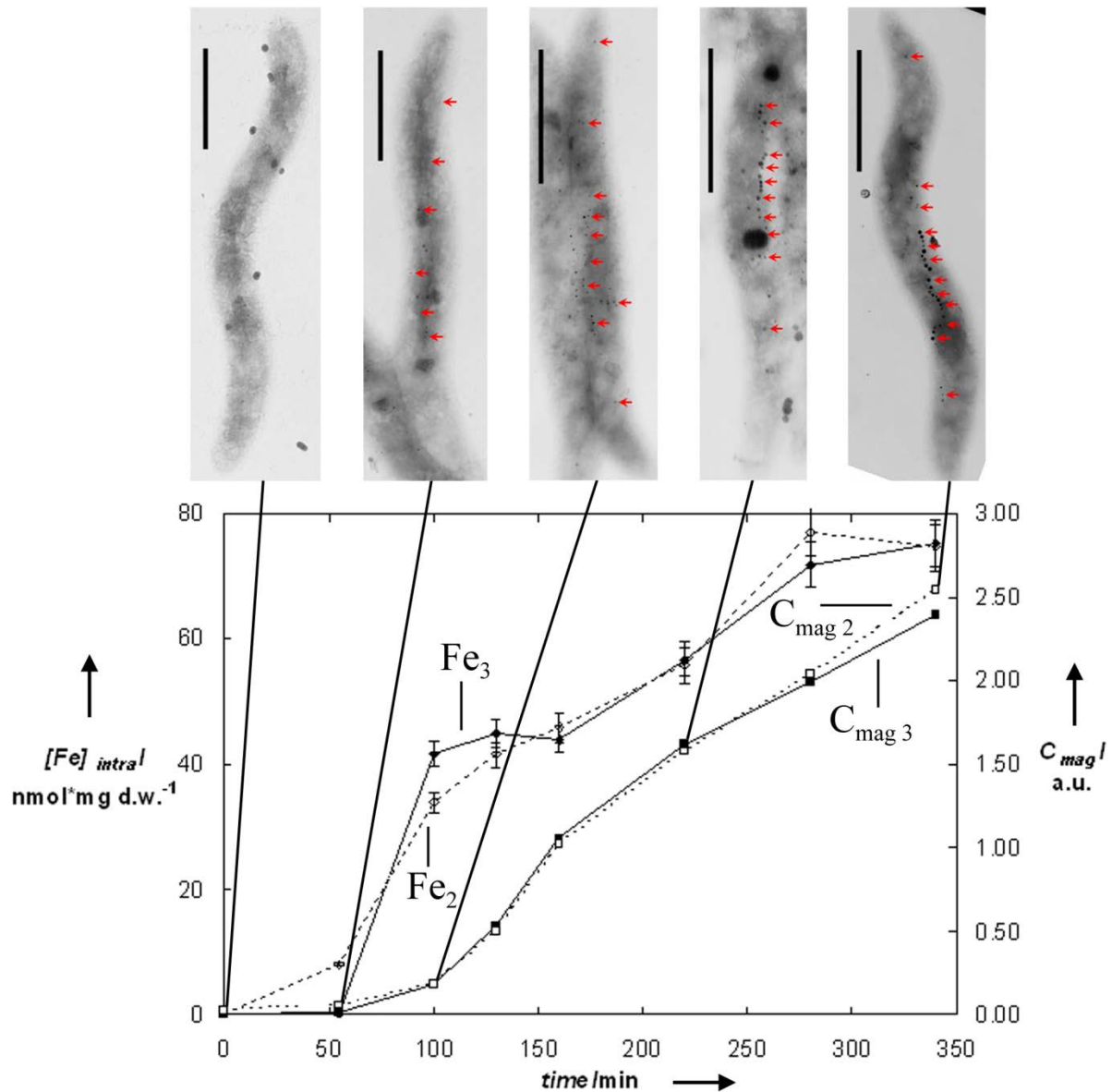


Figure 4: Time-resolved magnetosome formation after induction: Magnetite formation was induced in resting iron-deprived cells by addition of either Fe(II) or Fe(III) into the medium (black symbols and continuous line for Fe(III), open symbols and dashed line for Fe(II)) and was followed by intracellular iron accumulation ( $[Fe]_{intra}$  (d.w.: dry weight), diamonds), magnetic response ( $C_{mag}$ , squares), and TEM. The micrographs show the increase in particle number and dimensions (arrow pointed at every third magnetosome) in representative cells at different times after induction (scale bar: 1  $\mu$ m). Formation of chains is complete after 340 minutes. Figure modified with permission from (Faivre et al., 2007).

Briefly, magnetite formation could be induced in iron-starved non-magnetic wild-type MSR-1 cells by the addition of either ferric citrate or ferrous ascorbate (Figure 4), indicating that the bacteria are capable of intracellular reduction or oxidation of extracellular iron to form the mixed-valence



magnetite crystals. Crystallites were not detected by TEM until 55 min after iron addition, coincident with the appearance of magnetically oriented cells as detected by  $C_{mag}$  measurements (Figure 4). Over time, the average particle dimensions increased from less than 20 to more than 30 nm, and the number of crystals per cell from about 15 to ca. 30 (Table 2). After 6 h, formation of chains was complete.

**Table 2: Time-resolved properties of the developing magnetosomes and a comparison with the reference in continuously growing and Fe-supplemented cells (N.A. not applicable, N.D. not determined).**

Sample name	Crystallite	Immature	Intermediate	Mature	Reference
Time after induction (min)	55	110	220	340	N.A.
Average size (nm)	N.D.	19.4	26.3	31.5	32.5
Average number of magnetosomes per cell	N.D.	17.8	20.3	29.5	32.1
General morphology	Lack a well-defined morphology	N.D.	N.D.	Dominated by {1 0 0} faces	Cubooctahedral

Based on the results obtained by Mössbauer spectroscopy, we proposed a mechanism for magnetite formation, by which iron required for magnetite biomineralization is processed throughout cell membranes directly to the magnetosome membrane without iron transport through the cytoplasm, suggesting that pathways for magnetite formation and biochemical iron uptake are distinct. Magnetite formation occurs via membrane-associated crystallites, whereas the final step of magnetite crystal growth possibly is spatially separated from the CM (Figure 5) (Faivre et al., 2007). In addition, the establishment of this set-up was key for the development of further studies of magnetosome and chain formation. In fact, all research results presented hereafter in this chapter are based on this assay.

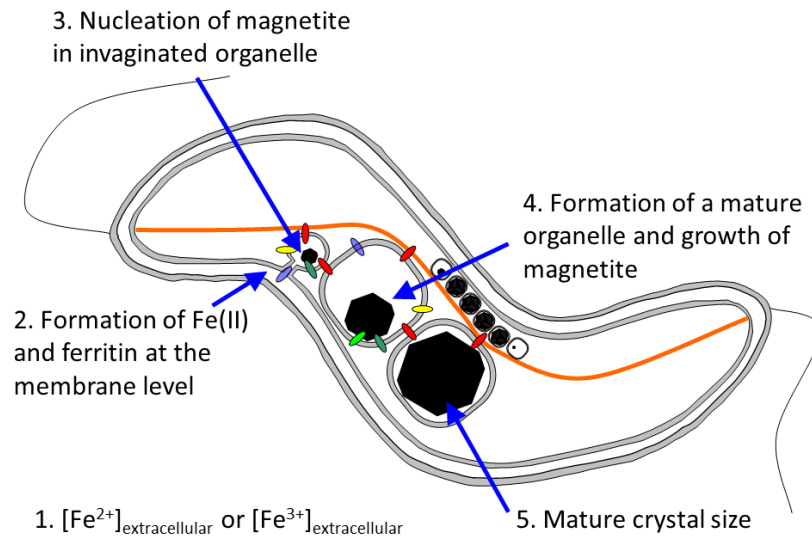


**Figure 5: Model of iron uptake and magnetite formation mechanism. The chain formation is concomitant to the magnetosome development.**

After I worked on this mechanism of magnetite formation in the cell, hematite was proposed to also be involved in the process (Staniland et al., 2007). However, in this case, it was not described what would be the different steps leading to magnetite from this intermediate. In addition, none of the published experiments could spatially resolve the position of the intermediates within the bacteria. We thus decided to have another look at the process by combining a high spectral technique under native condition (cryo X-ray absorption spectroscopy) with high resolution electron microscopy (Baumgartner et al., 2013c). This study was performed as part of the post-doctoral work of Jens Baumgartner.

The AMB-1 wild-type magnetotactic bacteria were initially grown to reach a non-magnetic state as presented before. Upon cell transfer into Fe-containing medium, TEM images show after 10 min the first dark-contrasted spots of a few nanometers size in the cells, which form over time discretely and widely distributed on a nearly linear axis along the inner curvature of the spirillum helix. This is consistent with the known localization of the magnetosomes in AMB-1 and in agreement with similar observations on *M. gryphiswaldense* MSR-1 (Faivre et al., 2007)(Figure 4).

We used the X-ray absorption near edge structure (XANES) at the Fe K-edge to follow the iron speciation (Figure 6). The characteristic spectral features of magnetite become increasingly dominant over time (Figure 6A, black arrows). From the first to the last member in the time series we observe a shift of the Fe edge toward lower energy values consistent with the increase of Fe<sup>II</sup> in the magnetite structure (Fe<sup>III</sup><sub>2</sub>Fe<sup>II</sup>O<sub>4</sub>). This shift indicates an overall reductive phase formation process *in vivo*. At the early stages, we observe a shoulder feature at 7139 eV (Figure 6A, red arrow), which disappears concomitantly with the crystallization of magnetite. This shoulder is observed in the XANES spectrum of a regular Fe<sup>III</sup> octahedron such as the Fe<sup>III</sup> hexaaquo complex and in strengite (FePO<sub>4</sub>·2H<sub>2</sub>O) (Voegelin et al., 2010). It is also observed in hydrated amorphous ferric sulfate (Wilke et al., 2001) as well as in poorly ordered ferric phosphates (Voegelin et al., 2010). It is known that prokaryotes can store iron in the form of (bacterio)ferritin, proteins that can contain large amounts of phosphate

along with iron, which disturbs the mineral structure (Rohrer et al., 1990; Rose et al., 1996; Waldo et al., 1995). Thus, we hypothesized about a phosphate contribution to the bacterial iron species studied here, which is supported by the similarity between the spectrum of the early bacterial mineral and that of the poorly ordered ferric phosphate hydroxides we synthesized as model compounds. Accordingly, the shoulder is clearly observed in the XANES spectra of our poorly ordered ferric phosphate hydroxides and its intensity increases with increasing P/Fe ratio (P/Fe=0.4, 0.8, 1.1) (Figure 6A). In contrast, the shoulder at 7139 eV is not observed in ferrihydrite (Fh), the mineral usually associated with ferritin. In addition, the shoulder at 7149 eV characteristic for ferrihydrite (blue arrow) almost completely disappears in our model phosphate compounds and the early stage cells. Linear combination fitting of the time-resolved induction series with the obtained standard spectra reveal that the bacteria - based on XANES - contain only two major different pools of iron, which change their spectral contributions over the time-course of biomineralization (Figure 6B, C): a disordered ferric phosphate-like phase, similar to the P/Fe=1.1 model compound, and the growing magnetite phase. While the Fe K-edge jump intensity (which is proportional to the iron concentration) increased by 3 - 4 fold over the investigated time span, the phase content of phosphate-rich ferric hydroxide calculated from the same technique dropped from around 90 % to 0 % (Figure 6C). Thus, the concentration of the phosphate compound fell below its initial value, indicating that the material is consumed in the mineralization of magnetite.

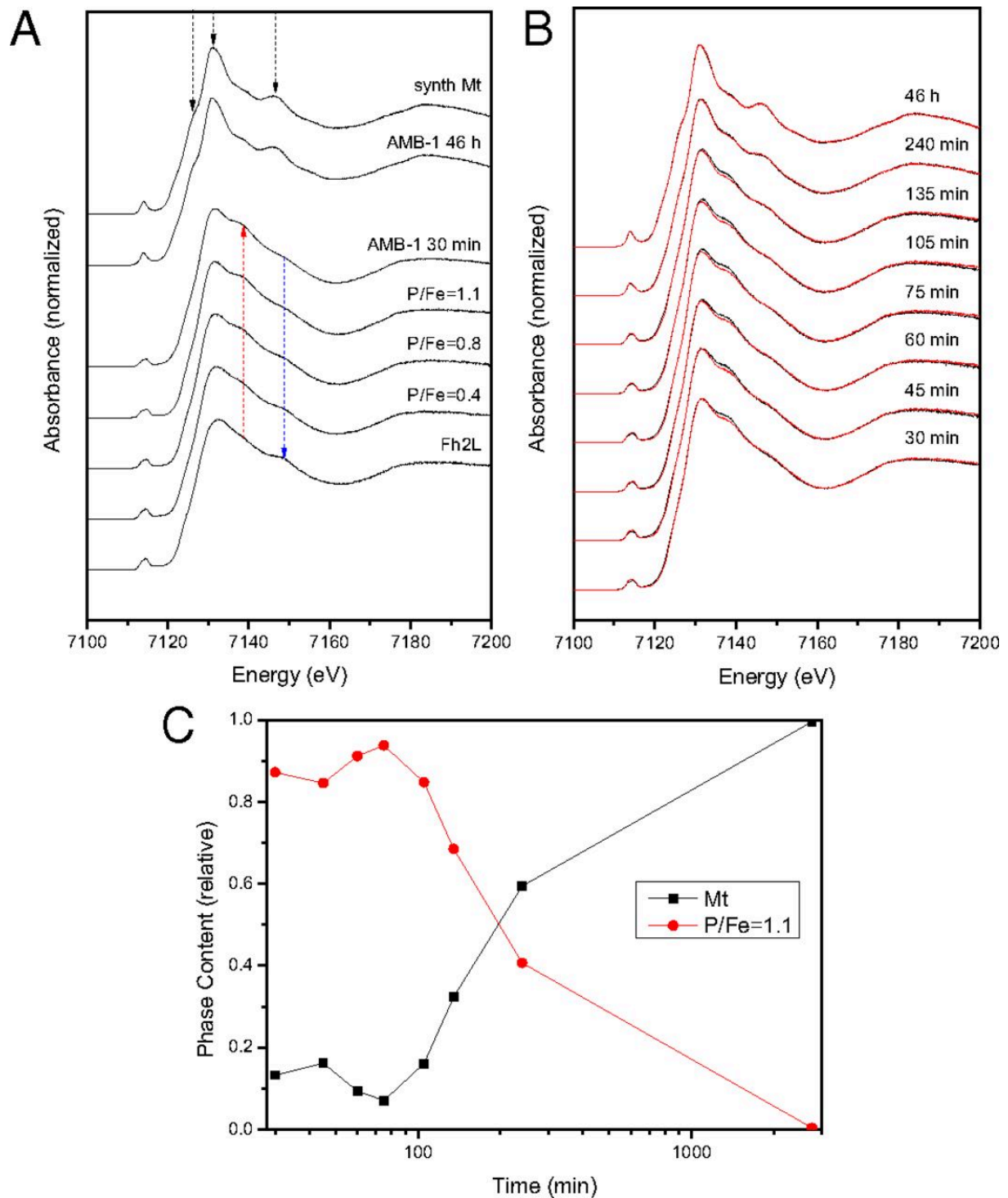


**Figure 6:** Time-resolved mineralization of magnetite from a phosphate-rich ferric hydroxide compound (bacterioferritin) in *M. magneticum* AMB-1. (A) Comparison of bacterial and reference spectra. (B) High-resolution XANES of Fe-induction time-series: experimental data are plotted in black, and linear combination data are in red. (C) Relative iron phase content, as determined by linear combination fitting. P/Fe, phosphate-to-iron ratio; Synth Mt, synthetic magnetite; Fh2L, 2-line Fh (figure from (Baumgartner et al., 2013c)).

We then studied the earliest mineralization stages using STEM-HAADF and XEDS elemental mapping to locate the phosphate-rich ferric hydroxide phase within the cells, and to correlate these results with that of the spectroscopic technique. For AMB-1 after 10 min induction, it appears that iron and phosphorus are spatially correlated in diffuse intracellular patches in line with the observation of the

disordered phosphate-rich ferric hydroxide phase by XANES and EXAFS (Figure 7B, C). Both methods reveal that iron, but not phosphorus, is also localized along the inner curvature of the helical cells in the form of defined nanometric particles or small aggregates. These particles and aggregates are distributed linearly along the long axis of the cell helix at discrete spacings of  $76 \pm 31$  nm in agreement with the known location and size of the magnetosome compartments in AMB-1 (Komeili et al., 2006). HRTEM and FFT analyses shows that the earliest observed crystalline particles 10 min after induction are magnetite ( $\sim 50\%$ ) or nanometric ferric (hydr)oxide aggregates ( $\sim 50\%$ ) such as ferrihydrite, poorly crystalline iron oxyhydroxides and hematite (Figure 7D-F). Particles of all phases at this stage fall within the same size range of around  $8 \pm 4$  nm. 30 min after induction only magnetite particles were observed.

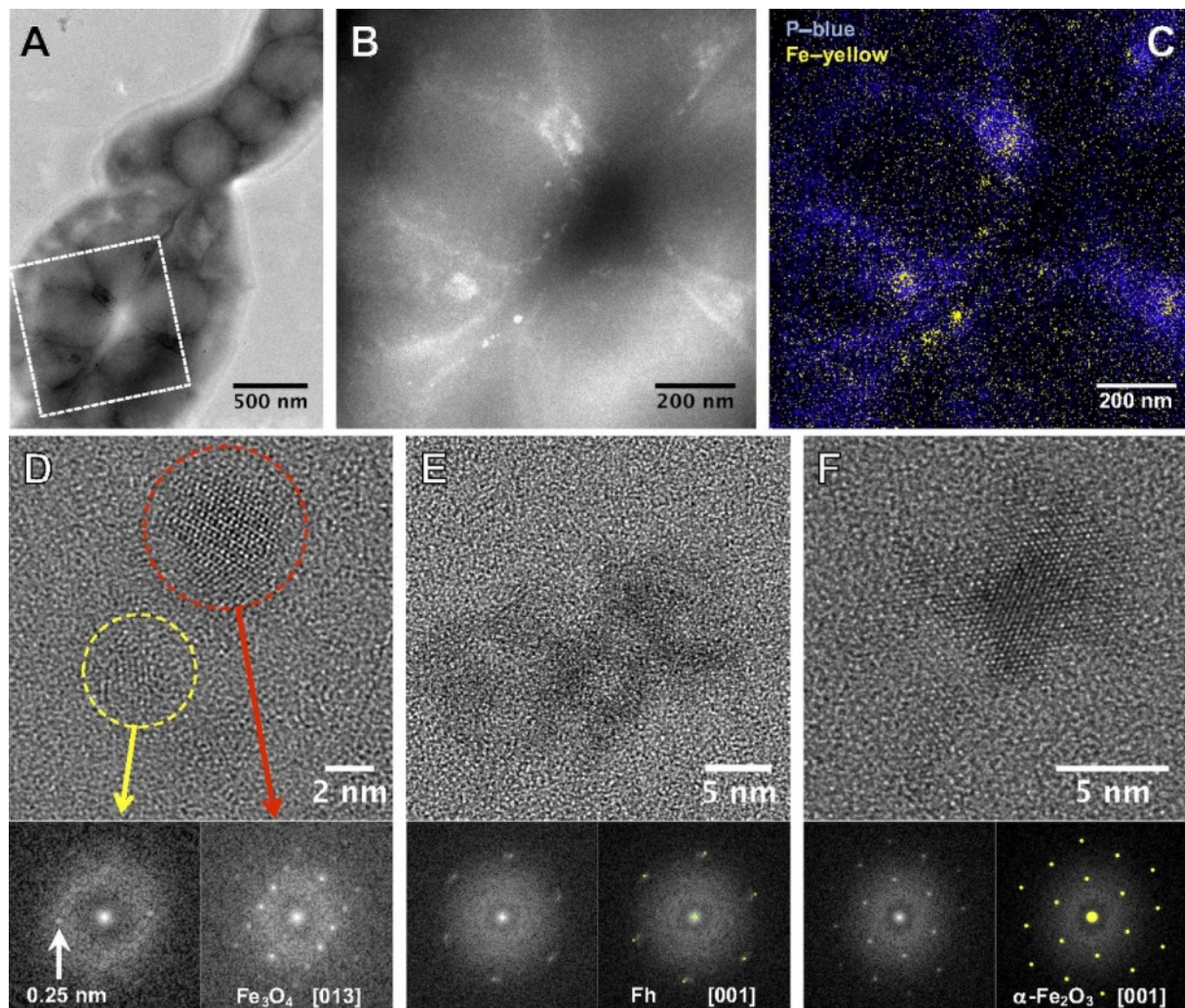


**Figure 7:** TEM observations of AMB-1 at  $t = 10$  min after induction. (A) Bright-field TEM image of a bacteria assembly. (B) HAADF-STEM image of the selected area in A revealing the presence of aggregates in the cell. (C) XEDS elemental mapping showing the colocalization of iron and phosphorus. (D–F) HREM observations of intracellular nanoparticles and their corresponding FFT analyses. (D) A magnetite nanocrystal is observed close to a poorly crystallized particle for which the interplanar distance of 0.25 nm is compatible with the Fh phase. (E) Poorly crystallized particle for which the diffraction is related to Fh. (F) Hematite nanoparticle (figure from (Baumgartner et al., 2013c)).

While ferrihydrite is known as a metastable precursor of magnetite in the presence of ferrous iron, hematite is not since it is typically considered as being thermodynamically too stable (Cornell and Schwertmann, 2003b). However, the high surface energy of  $0.75 \pm 0.16 \text{ J m}^{-2}$  renders the small and irregularly shaped nano-hematite in the size range observed here with surface areas  $\geq \sim 26000 \text{ m}^2 \text{ mol}^{-1}$  (equivalent to a minimal surface  $\sim 7 \text{ nm}$  sphere) potentially as metastable as the ferrihydrite phase (Navrotsky et al., 2008). Phosphate inhibits the formation of iron oxides including magnetite (Borch et al., 2007); thus, a biochemical mechanism must exist in the bacteria, which is able to separate phosphate from the environment of the nascent magnetite phase in the magnetosome vesicles likely concomitant with transmembrane transport. In addition, the observed reduction of ferric to ferrous iron is consistent with typical biological redox potentials (Kemp et al., 2008) although the specific physicochemical parameters within these vesicles are unknown. To our knowledge bacterioferritin has not yet been studied in detail by high resolution imaging techniques likely due to its amorphous character. Eukaryotic ferritins on the other hand are well-studied proteins and show structural features consistent with  $\sim 5 \text{ nm}$  large iron-containing particles with  $\sim 2 \text{ nm}$ -sized domains of ferrihydrite and sometimes hematite very similar to our observations in the bacteria (Pan et al., 2009; Quintana et al., 2004). Prokaryotic ferritin primarily differs from its eukaryotic homologues in the high phosphate content which can reach P/Fe ratios of 1.7 (for comparison: horse spleen ferritin has a ratio of P/Fe = 0.125) (Rohrer et al., 1990). Therefore, we expect that separation of phosphate from bacterioferritin will lead to crystallization of ferrihydrite as observed here within the magnetosomes (for the updated model of magnetite biomineralization, see Figure 8). Upon partial reduction of  $\text{Fe}^{\text{III}}$  to  $\text{Fe}^{\text{II}}$ , this nanometric phase can transform to magnetite. As we did not observe ferrihydrite by X-ray absorption spectroscopy, this phase is likely only present as minor and short-lived intermediate in this process. The irregular morphology of the first magnetite particles supports the notion of a solid phase transformation from the precursor. In fact, only very recently we have been able to demonstrate that in solution synthetic magnetite nucleates and grows from nanometric ferrihydrite-like aggregates bearing close resemblance to the precursor material here both in size and morphology (see later and in (Baumgartner et al., 2013b)).

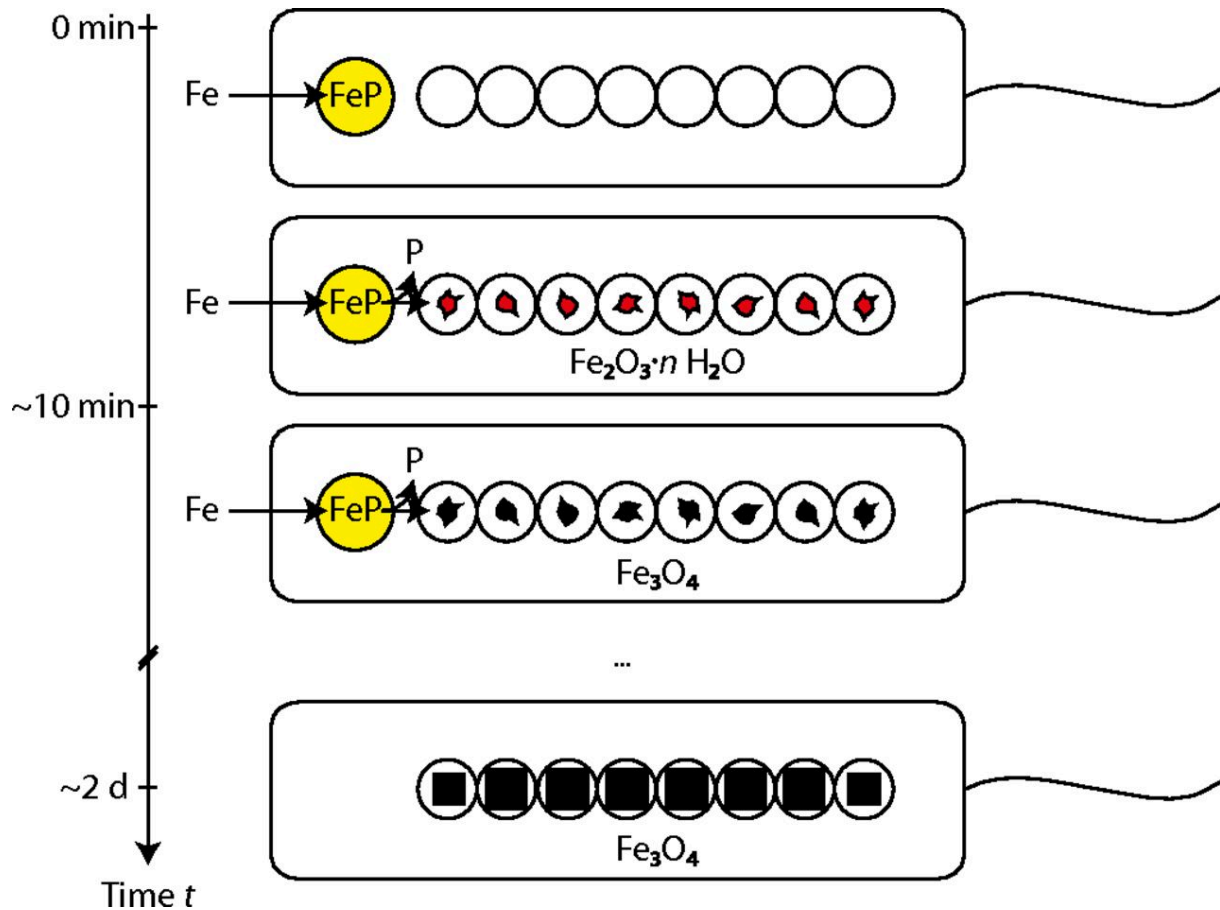


Figure 8: Schematic illustration of the suggested magnetite biomineralization mechanism in magnetotactic bacteria. On uptake, iron (Fe) is stored in a phosphate-rich ferric hydroxide phase (FeP). Fe and P are separated in the transfer process into the magnetosome compartments, leading to the formation of Fh ( $Fe_2O_3 \cdot n H_2O$ ). Reduction of this phase yields magnetite, which grows out to mature crystals (figure from (Baumgartner et al., 2013c)).

The spectroscopic results were concomitantly confirmed by an independent work – without spatial information however - that also showed by magnetic measurements that the iron in the ferritin was indeed transforming with time into magnetite (Fdez-Gubieda et al., 2013b). The findings described here also bear significance beyond magnetite mineralization in magnetotactic bacteria alone as some higher organisms such as the homing pigeon are also capable of its formation. Interestingly, in these birds, magnetite appears to be co-localized with ferric phosphate suggesting potential similarities in the formation mechanisms in pro- and eukaryotes (Fleissner et al., 2003). In addition, the technique employed here has a great potential to also unravel the biomineralizing process in other organisms or that of greigite in other magnetotactic bacteria.

### 2.2.2. MmsF control magnetosome dimension

Initial studies on *Magnetospirillum gryphiswaldense* MSR-1 (Grünberg et al., 2001), a bacterial strain isolated by D. Schüler in the 90s (Schleifer et al., 1991a) and for which the first genetic system was established (Schultheiss and Schüler, 2003), led to the first indication that magnetosome genes were not randomly scattered throughout the genome of the organism but rather confined to a single

genomic region later called the magnetosome island (MAI) (Ullrich et al., 2005), in analogy to other genomic islands described previously (Jogler and Schüler, 2009). The major regions involved in the biomineralization were analyzed step by step by several groups in parallel on different strains and were published in two major studies showing that genes in the *mamAB* clusters were the most important for magnetite formation (Lohße et al., 2011; Murat et al., 2010b).

In addition to the understanding of how a large set of genes can influence magnetosome biomineralization and even the formation of the organelle itself, studies were performed to determine the role of dedicated genes and proteins on the control of the mineral particle size and morphology. In this case, one of the decision criterion for the choice of the molecular player was the physical association of proteins with the mineral part of the magnetosome or at least the presence of trans-membrane domain(s) in its predicted structure. For example, the role of *mamA* and *mamGFDC* were studied and their role were respectively associated with activation of nucleation and size and morphology control (Komeili et al., 2004; Scheffel et al., 2008). Getting magnetosomes with the “right” size is of primary importance for the cells as it is the only manner to ensure that they will properly be able to passively align with the Earth magnetic field lines. Indeed, magnetosomes in the SP size range may not be able to fully achieve this function (Faivre and Schüler, 2008). Further studies focused on the role of iron transporters, as MTB accumulate up to 4 % iron in dry weight, where common bacteria do not exceed 0.1 % (Uebe et al., 2011b; Uebe et al., 2010; Yijun et al., 2007).

We decided to study the role of the *mms6* gene cluster and of its individual genes (Murat et al., 2012). This work was done in collaboration with the group of Arash Komeili (University of California, Berkeley). My group took over the mineralogical and crystallographical description of the generated strains as part of the doctoral work of André Körnig. Besides the above mentioned *mamAB* region, an 8-gene region termed R3, encompassing the *mamFDC* and *mms6* gene clusters, also played an important role in magnetite biomineralization, as its deletion leads to the production of small and misshapen crystals (Murat et al., 2010b). Intriguingly, the biomineralization phenotype of the  $\Delta R3$  mutant in *Magnetospirillum magneticum* AMB-1 (and that of the deletion of the equivalent region in MSR-1) is more severe than that of *mms6* in AMB-1 or a *mamGFDC* deletion mutant in the closely related bacterium MSR-1 (Lohße et al., 2011; Murat et al., 2010b; Scheffel et al., 2008). Given the clear role of Mms6 in magnetite biomineralization *in vivo* (Tanaka et al., 2011) and *in vitro* (Arakaki et al., 2003; Prozorov et al., 2007), we hypothesized that the more severe phenotype of the  $\Delta R3$  mutant may be due to a combined loss of *mms6* and *mamFDC*. An additional possibility was that the other genes of R3, not previously characterized genetically, could play a dominant role in magnetite biomineralization.

By generating independent non-polar deletions of these genes, we showed that the single deletion of the previously uncharacterized gene *mmsF*, but not that of *mms6* or of the combined *mamFDC*, is primarily responsible for the severe phenotype of the  $\Delta R3$  mutant (Figure 9) (Murat et al., 2012).



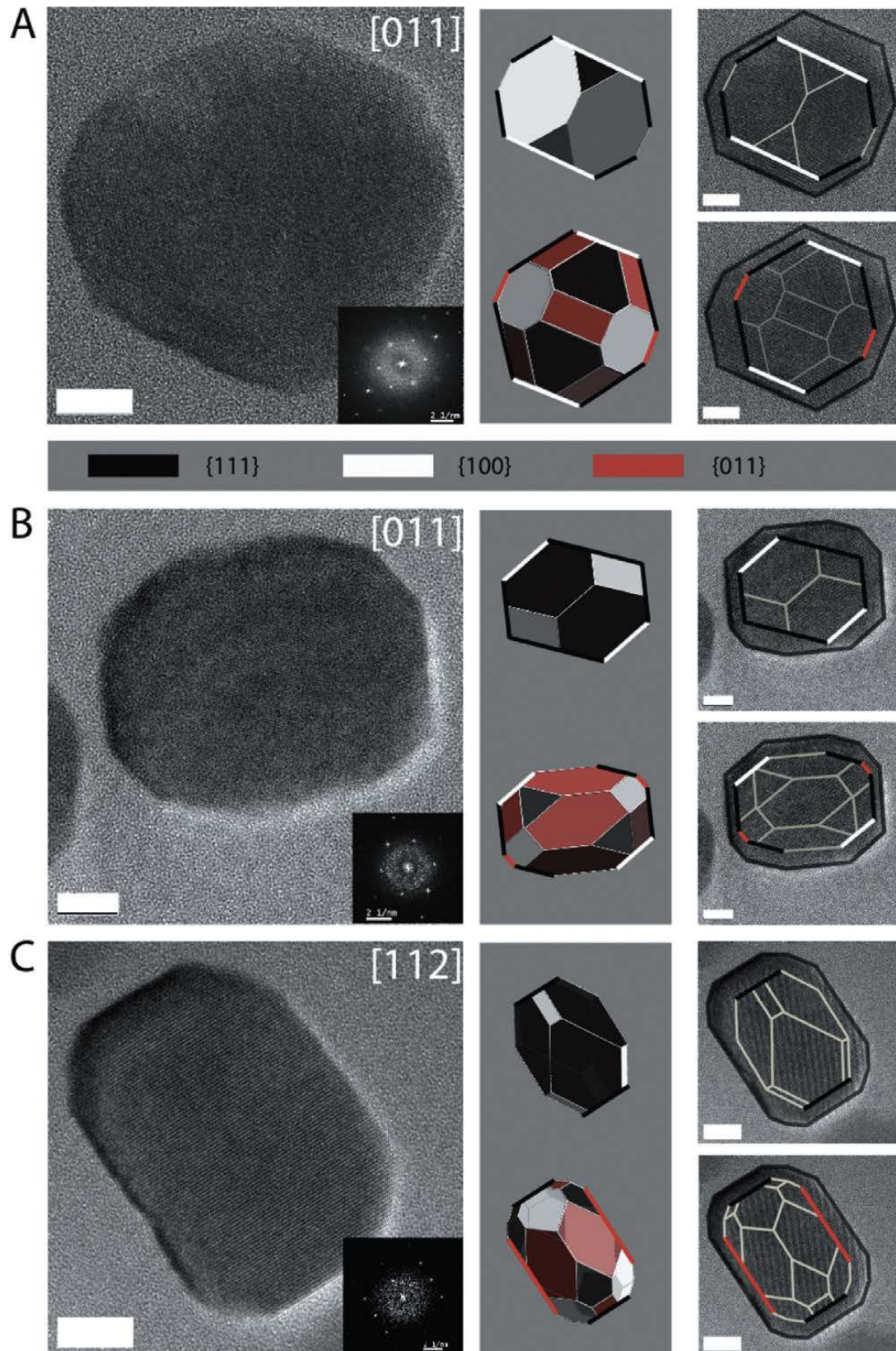


Figure 9: Magnetite nanocrystals with altered geometric properties are produced in the absence of *mmsF*. Left, HRTEM images of representative magnetite crystals and corresponding Fast Fourier Transforms (FFT) (inset) in (A) wild-type AMB-1, (B and C)  $\Delta mmsF$  mutants. Right: Crystal models (grey background) and projected frame models (superimposed with the original HRTEM images) oriented as in the HRTEM image. Face forms {100}, {110} and {111} are colored according to the scheme indicated in the grey band between (A) and (B). Faces parallel to lattice planes belonging to the zone axis of each micrograph are outlined with the corresponding color. Scale bar: 10 nm. Figure reproduced with permission from (Murat et al., 2012).

In addition, we showed that initiation of magnetite synthesis did not seem to be delayed in absence of *mmsF*. Instead, crystal growth followed a pattern reminiscent of wild-type AMB-1 until the crystals reach about 25 nm in length at which point crystal growth stalled in the  $\Delta mmsF$  mutant while it proceeded in wild-type cells. The key role of this protein in biomineralization was further highlighted in our surprising finding since in the 8-gene deletion mutant  $\Delta R3$ , the expression of MmsF was sufficient to restore the synthesis of mature-sized magnetite crystals (Murat et al., 2012).

To investigate the capabilities of MmsF more broadly, we constructed a strain in which the entire MAI, save for the *mamAB* gene cluster, was deleted. Surprisingly, these 18 genes were sufficient for the early steps of magnetosome formation in AMB-1 but only led to the biomineralization of small (SP) magnetite (Figure 10, EM performed by L. Bertinetti) that did not facilitate the orientation of cells in a magnetic field. However, the expression of *mmsF* in this 'minimal-island' strain resulted in a significant improvement of magnetite synthesis that allowed the cell pellets to be attracted by a magnet (Murat et al., 2012).

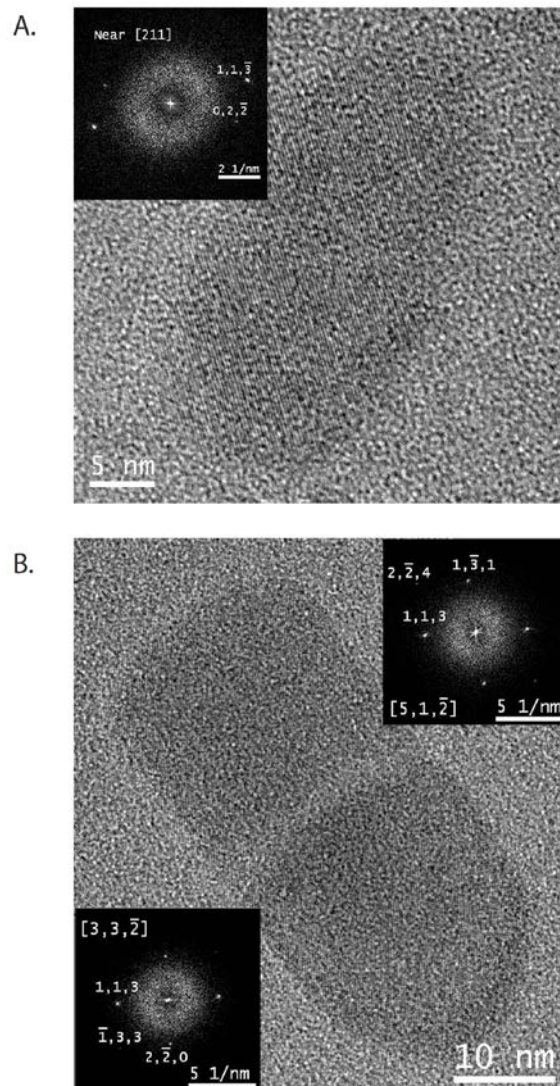


Figure 10: the miniMAI strain produces magnetite crystals. HRTEM images of two particles from the miniMAI strain shows that they are clearly crystalline with spacing that is consistent with magnetite. Figure reproduced with permission from (Murat et al., 2012).

Taken together, these results demonstrate that *MmsF*, and to a lesser degree *Mms6*, are major players in the control of magnetite biomineralization in AMB-1. Future engineering of the levels of expression of the *mamAB* and the *mmsF* genes in the minimal strain, as well as a more expanded search for biomineralization factors may lead to higher levels of magnetite production and therefore optimize the overall magnetic capabilities of such a mobile cassette. This work thus lays out a potential blueprint for the development of an autonomous genetic unit for the biological production of magnetic minerals with controlled size.

## 2.3. Magnetosome chains

The next level of hierarchy that I present here is the magnetosome chain. Formation of a single magnetic dipole based on single-domain sized magnetosomes, the latter being themselves made of highly stoichiometric magnetite. Single, non-assembled magnetosomes would not be sufficient to passively align the bacteria. Thus, the dedicated organization in chain is necessary for magnetotaxis. Hereafter, I describe experimental works showing the orientation of crystals within a magnetosome chain. I subsequently show what are the magnetic aspects of the chain formation process and how given molecular players are involved. Finally, I present a theoretical work studying the interplay of the physical and biological forces in the course of chain maturation.

### 2.3.1. Magnetite crystal orientation in magnetosome chains

The magnetosome chains represent a paradigm of a functional biological 1D nanostructure. It is typically assumed that a dedicated trait of magnetotactic bacteria is the strict biological control on the aspect ratio and orientation of the magnetosome crystals such that the axis of elongation is aligned with the chain axis, and further, that they both correspond to a magnetic easy axis of magnetization ( $\langle 111 \rangle$  in magnetite). A few TEM (Alphandéry et al., 2009; Li et al., 2013; Meldrum et al., 1993) or electron holographic studies (Buseck et al., 2001; Dunin-Borkowski et al., 1998; Lins et al., 2005) have confirmed combined this  $\langle 111 \rangle$  elongation and chain orientation in the types of organisms that produce magnetite magnetosomes of symmetric morphology, such as MC-1, MV-1, and the magnetospirilla strains MS-1, AMB-1. The  $\langle 111 \rangle$  trait as inferred from single-cell observations has been statistically confirmed by means of ferromagnetic resonance (FMR) measurements on bulk samples of MSR-1 and MV-1, where FMR spectra simulated for  $\langle 111 \rangle$  oriented chains were in good, though not perfect agreement with the experimental spectra (Charilaou et al., 2011a; Charilaou et al., 2011b). This suggests some degree of disorder and inhomogeneity. More surprisingly, however, elongations along various other crystallographic axes have been observed in cells with magnetosomes of irregular morphology (Hanzlik et al., 2002; Li et al., 2010; Lins et al., 2007; Pósfai et al., 2006; Taylor et al., 2001). In these cases, the chain architecture often is less regular, which makes it difficult, if not impossible to determine on the single cell level the typical relationship between crystal axes and chain structure.

André Körnig, as one of the main part of his doctoral work, performed X-ray diffraction on pre-aligned magnetotactic bacteria from different strains that are established models for magnetite biomineralization and for which the crystallographic orientation of the chain axis might differ (Körnig et al., 2013). TEM images show that the cell bodies are oriented such that their magnetosome chains are aligned with the externally applied magnetic field, resulting in samples in which all magnetosome chains were close to parallel to each other.

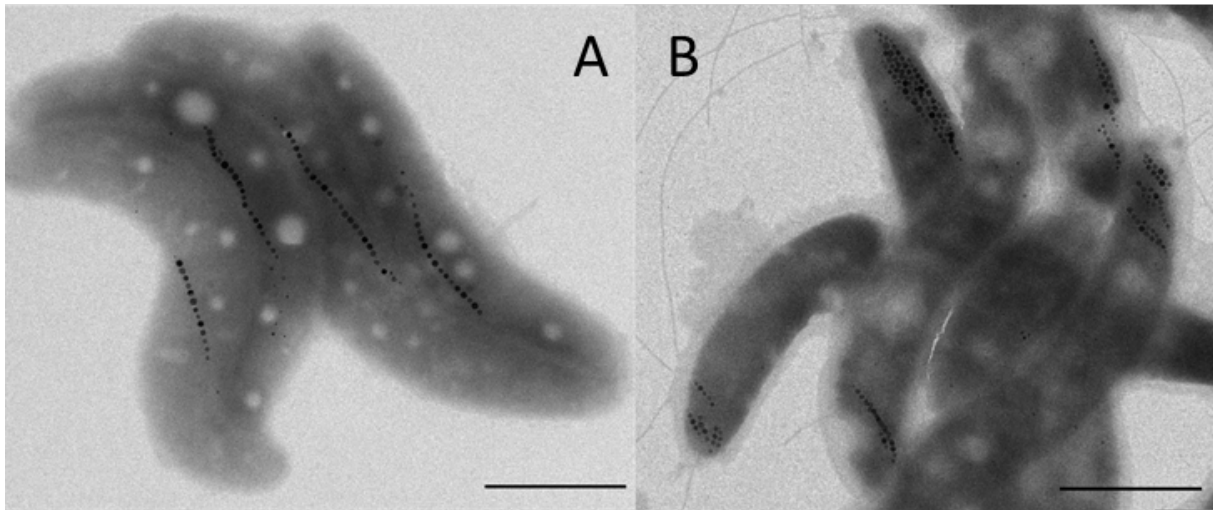
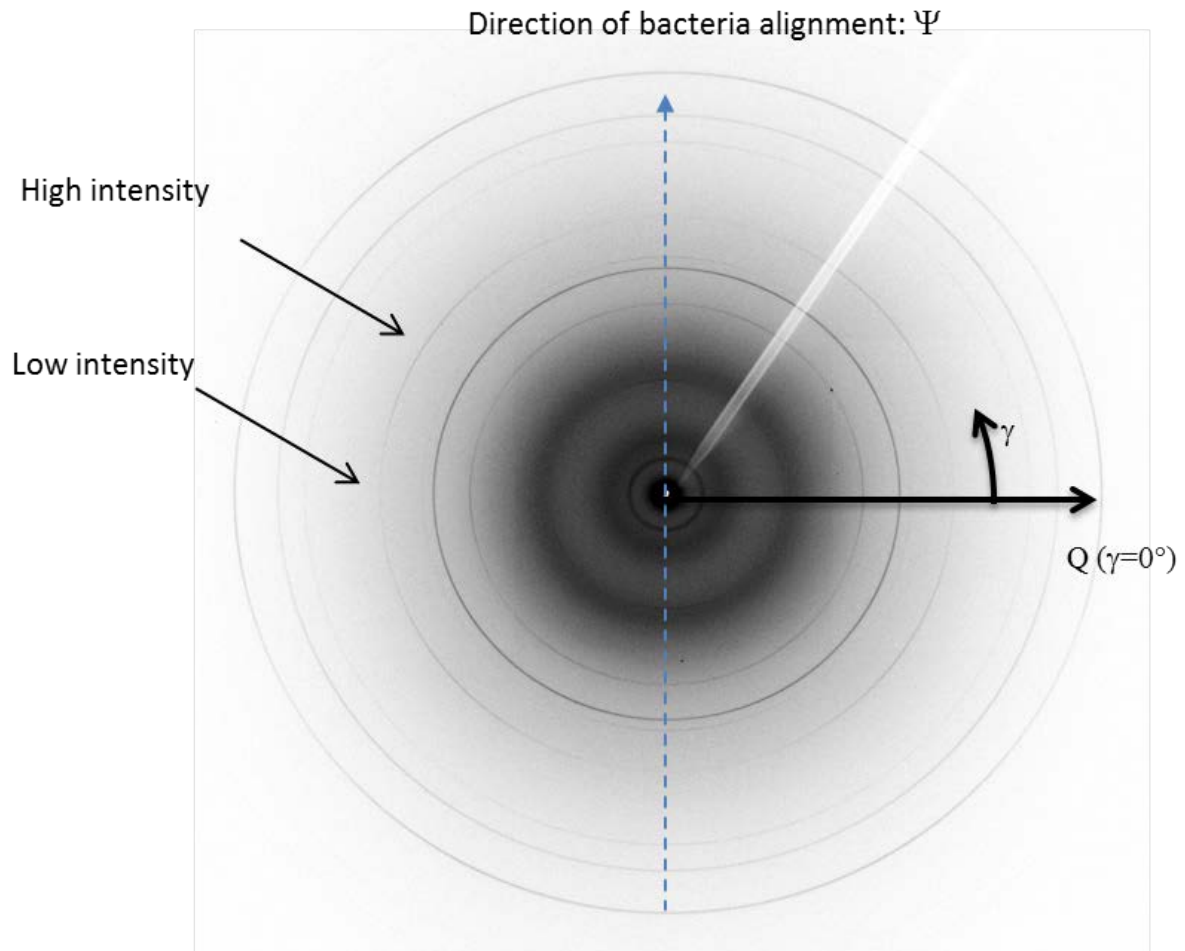


Figure 11: TEM images of wildtype (A) and  $\Delta mamJ$  mutant (B) cells of MSR-1 dried in the presence of a magnetic field, scale bars represent  $1\mu\text{m}$ .

Aligned bacteria of different strains (the wildtype and a  $\Delta mamJ$  mutant of *Magnetospirillum gryphiswaldense* MSR-1, *Magnetospirillum magneticum* AMB-1, and *Desulfovibrio magneticus* RS-1) and isolated magnetosomes of the MSR-1 strain were investigated with high-resolution XRD. The diffraction pattern of MSR-1 is shown in Figure 12. As expected, the positions of the diffraction rings, displayed as peaks in the diffractogram (azimuthally integrated  $I(Q)$ ,  $Q = 4\pi \sin(\theta) / \lambda$ , where  $2\theta$  corresponds to the scattering angle and  $\lambda$  is the wavelength of the beam), can be indexed to magnetite. Importantly, the Debye rings show systematic variations in their azimuthal intensity distribution (AID), indicating a non-random orientation of the crystals.



**Figure 12:** Two dimensional diffraction pattern, darker pixel display higher diffracted intensity. The dashed line indicates the direction of the bacterial alignment along the external magnetic field. The solid lines indicate the direction of integration of the XRD pattern.

Upon projection of the 2D XRD pattern onto a Cartesian grid (azimuthal angle  $\gamma$  vs  $Q$ ), the diffraction rings become straight lines and the AID along the rings can be recognized more easily (Figure 13). The AID  $I_{hkl}(\gamma)$  of the diffraction ring for a certain set of planes  $\{hkl\}$  were obtained by radial integration of the 2D-pattern and a localized background subtraction. The AID  $I_{hkl}(\gamma)$  of four Debye rings are shown in Figure 13B.  $I_{hkl}(\gamma)$  represents the normalized directional distributions of the  $hkl$  lattice in the sample. The symmetry of the pattern can be observed in the intensity distribution of the different planes. All the AID display line (mirror) symmetries at the angles indicated by the dashed lines at  $\gamma = 2^\circ, 92^\circ, 182^\circ$  and  $272^\circ$ . In the 2D-XRD pattern, these angles correspond to the plane parallel to the direction of bacterial alignment ( $92^\circ$  and  $272^\circ$ , blue line in Figure 13) and to the plane perpendicular to it ( $2^\circ$  to  $182^\circ$ ). A further analysis of the AID reveals the type of fiber texture: The crystallographic direction parallel to the fiber axis can be determined from the  $I_{hkl}(\gamma)$  plots. The fact that the intensity maxima in the  $I_{222}(\gamma)$  are parallel to the fiber axis indicates that the texture is a  $[111]$  fiber texture.

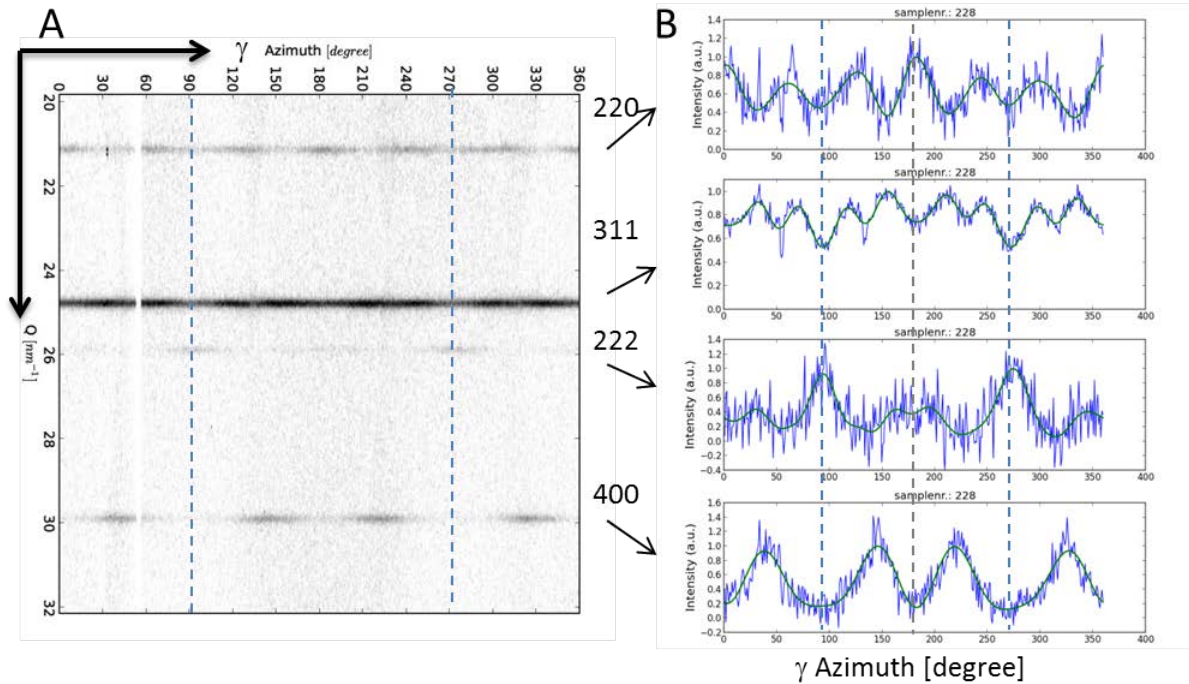


**Figure 13: (A) background subtracted Cartesian plot of  $Q$  vs  $\gamma$  of the inner rings of the XRD pattern; (B) normalized azimuthal intensity variations  $I_{hkl}(\gamma)$  for different rings, dashed lines indicate symmetry angles, blue dashed lines are along the direction of the bacteria alignment and therefore the fiber axis.**

We determined the half width at half maximum (HWHM) of the peaks in the AID as a measure for the dispersion in the fiber texture. The HWHM is in the range of  $15^\circ$ , compared to a full width of  $0.15^\circ$  in the radial direction, the latter reflecting instrumental broadening (resulting from beam divergence and detector point spread) and grain-size related broadening (in nanoparticles, crystallite size correlates inversely with peak width). Since the effects of instrumental and grain size related broadening are equal in azimuthal and radial direction, the observed HWHM in azimuthal direction of about  $15^\circ$  reflects deviations from perfect crystal alignment. This deviation has two contributions, one from intra-chain scatter of [111] orientations, the other from cell-to-cell variations in the axial orientation of the magnetosome chains, as can be observed in the TEM image (Figure 11).

Not surprisingly, a [111] fiber texture with similar HWHM was observed for AMB-1 cells (Figure 14). This strain also forms cubooctahedral magnetosome crystals, albeit with slightly larger elongation than MSR-1 does, and assembles the magnetosome in a similar, although more fragmented chain arrangement. The magnetosome crystals of this strain also assembled with their [111] direction along the chain axis and thus along the bacterial pole to pole direction.

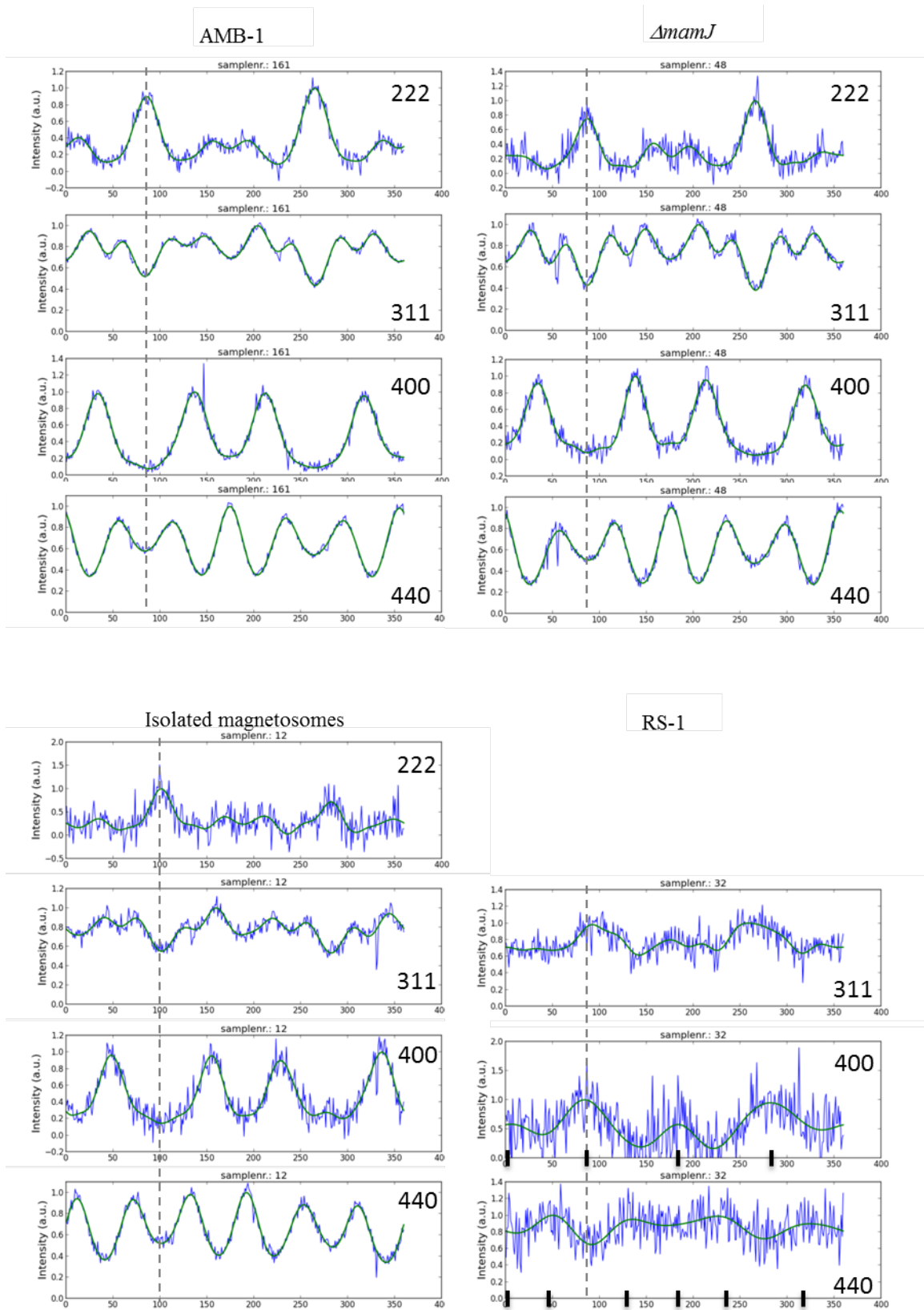


Figure 14: AID of different Debye rings of cells of AMB-1, a  $\Delta mamJ$  mutant of MSR-1, RS-1 cells and isolated magnetosomes from MSR-1. The direction of the magnetic field applied during the drying process is indicated by dashed lines. In the RS-1 graphs, the black lines indicate expected intensity maxima for a [100] fiber texture.

A [111] fiber texture has also been observed for a mutant of the MSR-1 strain, which lacks the anchor protein MamJ (Figure 14) and displays therefore no linear chain structures but clustered magnetosome arrangements. In a magnetic field, the cell bodies of  $\Delta mamJ$  mutants are practically not aligned. A closer look at the TEM image reveals the effect of the magnetic field on the  $\Delta mamJ$  mutant: Magnetosome clusters become elongated in the field direction, which supports the concept that magnetosomes within these cells can move freely: the unbound magnetosomes can rearrange into an energetically more favorable disposition that is elongated along the field (Figure 11B). Isolated magnetosomes from the MSR-1 strain resulted in the same [111] fiber texture. Clearly, in this case again, the magnetosomes are free to move and to rearrange. In this case, the interaction with the external magnetic field forces them to orient along their [111] easy axis, which results in the observed fiber texture.

The cells of the RS-1 strain, which produce magnetosomes of irregular shape, showed a completely different behavior. RS-1 cells produce less magnetosomes so that the magnetic dipole moment per cell is too small for efficient alignment of the cells. The reduced number of magnetosomes also resulted in a diminished XRD signal intensity of the magnetite. Only three diffraction rings displayed variations in the AID (Figure 14). These AID differ strongly from those observed for the other samples. The higher intensities in the AID of the {400} planes along the direction of the magnetic field and perpendicular to it, as well as the higher intensities in the AID of the {440} planes at angular differences of  $45^\circ$  with respect to the direction of the magnetic field, suggests a [100] orientation of the magnetosomes in RS-1 cells. Pole-figure simulations, with an assumed HWHM of  $25^\circ$  around the [100] fiber axis resulted in a satisfying fit of all the experimentally observed AIDs for [311], [400], and [440].

The RS-1 strain with its [100] fibre texture appears to violate the hierarchical optimization principle, because the  $\langle 100 \rangle$  axis are magnetic hard axes in magnetite and therefore energetically unfavorable. Yet, in contrast to *Magnetospirillum* strains, RS-1 produces magnetosomes that in the mature stage are clearly nonequidimensional (Byrne et al., 2010) with an elongation most probably along a  $\langle 100 \rangle$  axis (Pósfai et al., 2006). The shape anisotropy for an aspect ratio of 1.25 or greater is sufficient to turn the  $\langle 100 \rangle$  axis of elongation into an effective easy axis and therefore overrides the intrinsic  $\langle 111 \rangle$  easy axis. Hence an energetically stable chain configuration can be achieved by aligning RS-1 magnetosomes with their  $\langle 100 \rangle$  elongation axes along the chain axis, as seen in the texture analysis. However, only roughly a third of the analyzed magnetosomes of RS-1 (Pósfai et al., 2006) have an aspect ratio that exceeds the critical value of 1.25, whereas most magnetosomes have aspect ratios between 1 and 1.25, which implies a continuum of effective easy axis orientations between [111] to [001]. Indeed, the [100] texture orientation in RS-1 is not so well developed compared to the [111] texture in the magnetospirilla strains (Figure 14). The smaller degree of texture in RS-1 may reflect diminished alignment with the external field, but also an overlay of different crystal orientations due to magnetosomes in different stages of maturity, from isometric  $\langle 111 \rangle$  oriented crystals in the early stage to mature crystals highly elongated along  $\langle 100 \rangle$ , with a continuum of hybrid states in between. This is supported by the TEM work of Li et. al. (Li et al., 2010), who described both equidimensional crystals (up to 30 nm edge length) and  $\langle 100 \rangle$  elongated crystals (up to 160 nm length but only 40 nm in width) in cells of uncultivated strain Myr-1, and divided the crystal formation process in two stages: isotropic growth of the particle, followed by anisotropic growth along the 100 direction (Li et al., 2010). The lower degree of texture observed for RS-1 could therefore be a result of isometric, transitional, and mature crystal morphologies.



It is not known, however, if the fiber texture, whether directed along  $\langle 111 \rangle$  as in magnetospirilla or  $\langle 100 \rangle$  as in RS-1, is strictly controlled by a biomineralization template (as it was suggested for an uncultured coccoid MTB (Abracado et al., 2010), or rather a result of magnetically enforced mechanical rotation of the easy axis into alignment with the chain axis caused by magnetostatic interactions among the crystals in the chain. This is because a magnetosome that is not oriented with its (effective) easy axis along the chain would represent no stable minimum and therefore would be subject to a torque. Physically enforced easy-axis alignment in the wildtype is consistent with our observation that FWHM values are similar for wild type MSR-1, its  $\Delta mamJ$  mutant, and even isolated magnetosomes of MSR-1. This agreement in FWHM indicates that the deviation from a perfect crystal alignment with the field does not depend on the spatial configuration of the magnetosomes (chains versus clusters). The fact that non-chain bound magnetosomes aligns with their easy axes along an external magnetic field, as seen in the  $\langle 111 \rangle$  fiber texture, demonstrates the great potential of physical alignment forces. From an experimental point of view, it may not be simple to distinguish between  $\langle 111 \rangle$  template-controlled and physically-induced alignment, except perhaps at early growth stages, when magnetosome crystals are too small to strongly interact magnetically with each other. Once the first crystal is mature, however, a newly nucleating magnetosome particle next to it will be subject to magnetic orientation forces, that *in silico* were shown to promote consistent crystallographic orientation (Kirschvink, 1992). Thus, RS-1 with its switch from isometric to anisotropic crystal growth appears to be a better candidate to test the physical alignment hypothesis. In a fresh cell culture of RS-1, a good proportion of crystals would be isometric and should then be aligned with one of their  $[111]$  axes, and thereby reduce the strength of the  $[100]$  fiber texture due to  $[100]$  elongated crystals that are already present. Over time, anisotropic growth along one of the  $\langle 100 \rangle$  axes would rotate the  $[100]$  axis of elongation into alignment with the chain axis  $[100]$ , so that the  $[100]$  fiber orientation should become more pronounced with time.

With this study, we have thus shown that synchrotron 2-dimensional X-ray diffraction is a powerful tool to study the crystallographic orientation of magnetosomes and the texture of magnetosome chains in magnetotactic bacteria. From our analysis, we can draw two main conclusions on the biological organization of magnetic nanoparticles in 1D. First, when building a nanostructured 1D magnet from a magnetically soft material like magnetite (low magnetocrystalline anisotropy compared to stray field energy), it is not obligatory to align the crystals with their intrinsic easy axis of magnetization ( $\langle 111 \rangle$  in magnetite) along the chain axis, even though it would represent the optimum for a given particle geometry. A stable 1-D magnet can be obtained as well on the basis of elongated crystals (aspect ratio  $> 1.25$ ) aligned with their elongation axis along the chain axis. This can be seen in RS-1 and other strains that produce magnetosomes with elongations along axes other than  $\langle 111 \rangle$ , thereby imparting a new effective easy axis on the crystals. In these cases, the crystallographic axis of elongation is species specific, which implies a high level of genetic control on the biomineralization mechanism. This contrasts with the straightforward design principle found in magnetospirilla, in particular with strain MSR-1, where the crystals are nearly isometric, and aligned with one of their *intrinsic* easy  $\langle 111 \rangle$  axes. Our results on isolated magnetosomes show that the  $\langle 111 \rangle$  orientation is the default case for isometric crystals and we conclude that the  $\langle 111 \rangle$  texture in wildtype cells of MSR-1 may be the result of physical effects (e.g., torques), not of an underlying genetic blueprint.

We suggest that magnetic forces/torques generally have an important role on the chain texture and remove the need for bacteria to actively control the texture. Just by controlling the direction of

elongation, they can affect the crystallographic orientation of the magnetosomes with respect to the chain direction. Of course, as opposed to the crystallographic texture of the chain, the very assembly of it requires biological control, as shown by the fact that linear chains are no longer observed in  $\Delta mamJ$  mutant (Scheffel et al., 2006b) and by theoretical approaches showing biological determinants at least helped stabilizing the chain (Klumpp and Faivre, 2012).

### 2.3.2. Magnetic aspects of the magnetosome assembly

The studies of the dynamics of magnetosome and magnetosome chain formations showed that the dimension of the crystals varied. In addition, we observed that the magnetosomes displayed a dynamic localization in the MSR-1 cells. Thus, and since those crystals are made of magnetite, the observed size variations also implied that the magnetic properties of the particles varied from SP to SSD and therefore, it was questionable if the magnetic interactions were involved in the process of chain formation.

I thus used the assay I recently had developed where magnetosome chain formation was induced from iron-starved non-magnetic MSR-1 cells in a time-resolved manner to answer this question too. Probes sampled at different time were magnetically characterized by an integrated approach involving first-order reversal curve (FORC) diagrams (Carvallo et al., 2009) and ferromagnetic resonance (FMR) spectroscopy (Charilaou et al., 2011a; Faivre et al., 2010) as part of my post-doctoral work and later as that of Anna Fischer in my group. FORC diagrams were performed by Claire Carvallo at the Institute of Mineralogy (University of Paris). In these, SP and SSD particles can be interpreted as a combination of coercivity distributions (and therefore grain size distributions in the case of a single magnetic mineral) and interaction field distributions. Therefore, they are the ideal tool for this studying the evolution of magnetite crystals through time, as well as the chain formation.

In addition, recent FMR studies also provided compelling evidence that this method possibly detects anisotropy of aligned mature magnetosomes in MTB as well as the coupling fields within the chains (Fischer et al., 2008; Kopp et al., 2006a; Kopp et al., 2006b; Weiss et al., 2004a). We were approached by a group from the ETH Zurich to analyze our cells by such method and thus could complement and compare the two magnetic techniques.

The FORC diagrams show the magnetic state of the magnetosomes and their interacting magnetic forces (Figure 15). After 90 min., the crystals are superparamagnetic with apparition of a tail of single domain after 180 min. The high coercivity pattern is the dominant one in the final sample. The full-width at half-maximum also increases, indicating higher magnetic interactions (Carvallo et al., 2009).

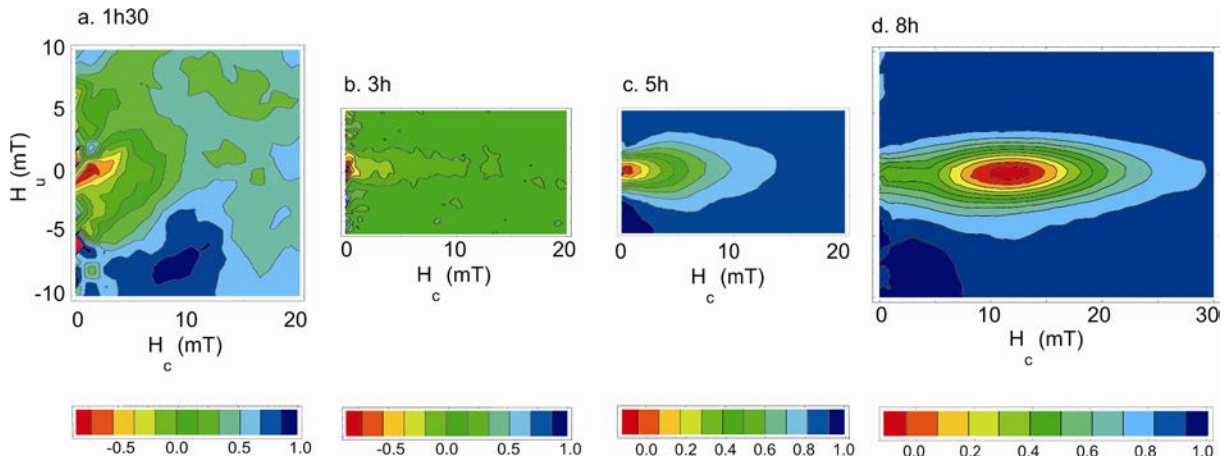


Figure 15: evolution of the FORC diagrams as a function of time after induction with an iron ferric source.

Figure 16 shows experimental and simulated FMR spectra of an induction starting from non-magnetic cells up to 7 hours. At the first recordable growth-stage, a weak paramagnetic signal was recorded, which could be attributed to Fe(III) in an octahedral configuration. At the next stage (T3, 110 min), the shape anisotropy of the isotropic particles was negligible and no cellular magnetic anisotropy due to particle interaction was present because the particles were too far away from each other. At T6 (280 min), where the particles have an average diameter of 23 nm, the first signs of dipole uniaxiality can be seen in the spectrum: the low-field tail corresponds to uniaxial anisotropy contributions, which require lower resonance fields along the easy axis. Finally, the development of a shoulder from T6, more pronounced from T8 up to T12 reflected the growth of aligned magnetosomes from few blocks to larger chain.

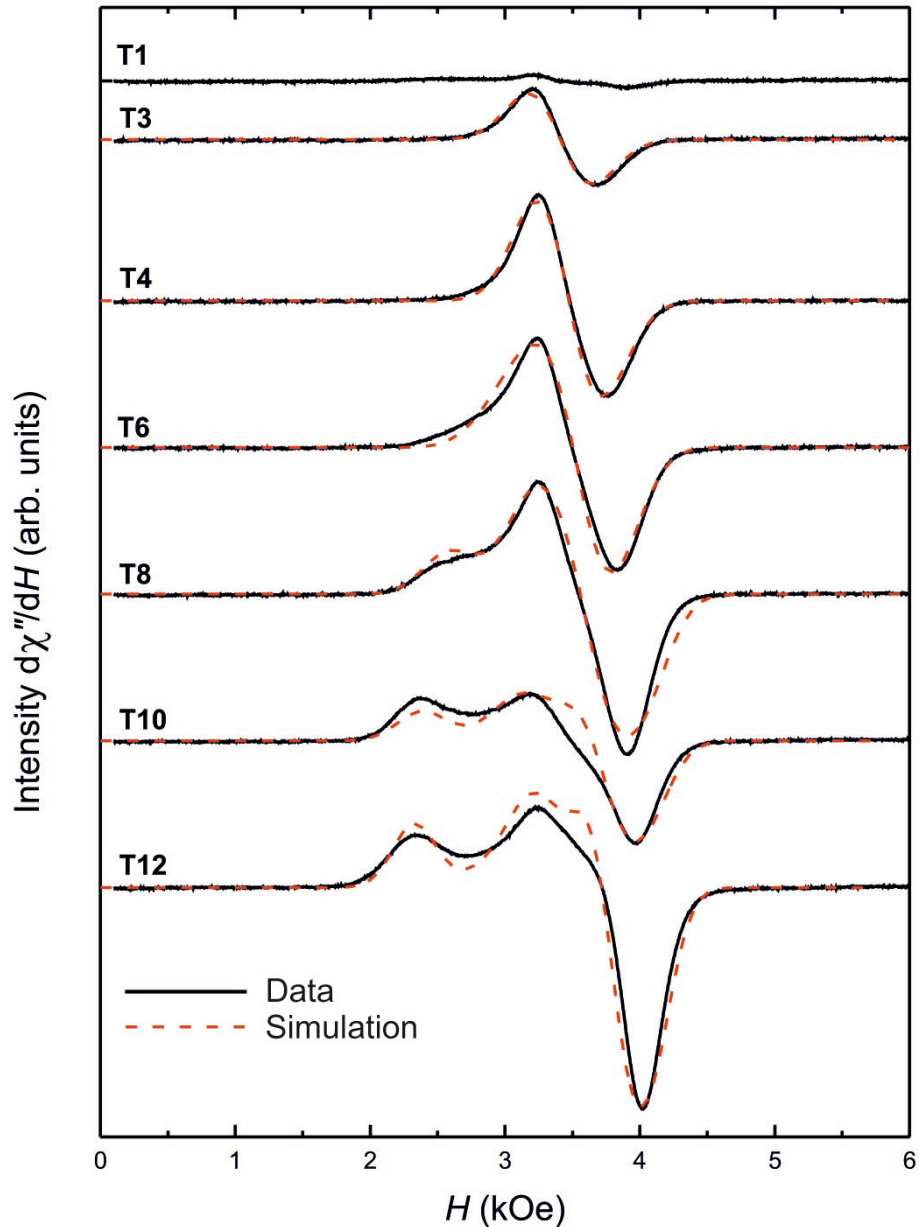
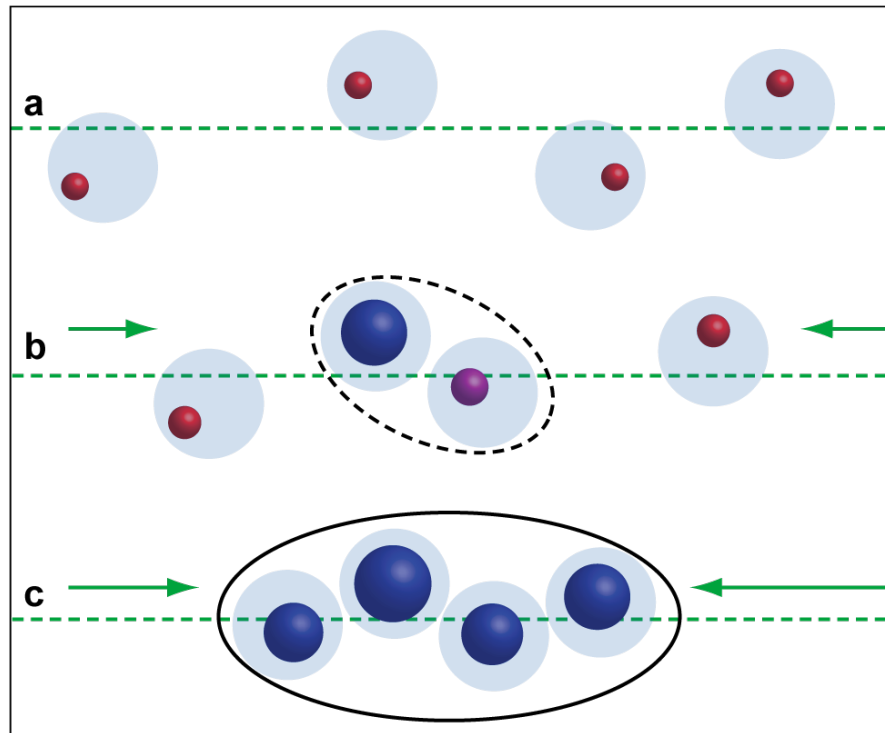


Figure 16: Measured (solid lines) and simulated (dashed lines) FMR spectra of MTB during particle and chain formation. For comparison, T3 is about 2h after induction, T6 5 h and T10 7 h. Figure reproduced with permission from (Charilaou et al., 2011a).

Altogether, our magnetic results were summarized in the following model (Figure 17): the first grains of magnetite formed were very small (in the SP range) and far away from each other (Figure 17a). As time passes by and more iron was taken up by the cells, the magnetic grain size increased and more and more grains became SD, and started forming chains. The stray field of these particles stabilizes the magnetic dipoles of the remaining and newly formed SP particles in the immediate neighbourhood (Figure 17b). When most grains were large enough to be SD, and arranged in chains, there still remained some SP grains. According to the TEM images, some of them are at the extremities of the chains, but the SP contribution on the FORC diagrams indicated that there should also remained some SP grains far enough from the chains so that they behave independently from

the SD chains. Most of the particles however are in the SSD domain and arranged in chain at the center of the cell (Figure 17c).



**Figure 17: Schematic sequence of cellular magnetic dipole formation.** SP magnetite particles (red) are nucleated in widely spaced organelles (light blue). (a) The green arrows indicate the movements of the magnetosomes along the cytoskeletal filament (dashed line). (b) The SSD magnetite (blue dot) and its magnetic interaction (dashed-lined ellipse) act as a magnetic dock to stabilize SP particles (purple dot). (c) The spacing and size of the magnetite are adjusted, and the closely spaced magnetite particles separated only by the magnetosome membrane generate a robust cellular magnetic dipole (solid-lined ellipse). Figure reproduced with permission from (Faivre et al., 2010).

### 2.3.3. Genetic aspects of the magnetosome assembly

If it is now clear that at least the genes *mamJ* and *mamK* are involved in the chain formation and stabilization in *Magnetospirillum* strains, as shown by a long list of publications on the subject (Draper et al., 2011; Katzmann et al., 2010; Komeili et al., 2006; Philippe and Wu, 2010; Pradel et al., 2006a; Rioux et al., 2010; Scheffel et al., 2006b; Scheffel and Schüler, 2007; Taoka et al., 2007), this was far from being the case when this work started. It is certainly the field, which has advanced the most during the last years. What was known at the time was that a magnetic chain would have the tendency to collapse in a ring if not stabilized (Philippe and Maas, 2002). Thus, such a stabilizing structure was thought to exist although such compartmentalization was unknown in prokaryotes at the time.

Among the genes present in the MAI of MSR-1, we decided to target *mamJ*, because the MamJ protein was characterized by a high content of acidic amino acids and a repetitive domain structure, features that have frequently been found in other proteins associated with biomineralization

processes (Evans, 2003). A MamJ-deficient mutant strain ( $\Delta mamJ$ ) was thus generated in order to verify the assumed essential role of MamJ in the formation of functional magnetosomes (Scheffel et al., 2006b). Contrary to our expectations, the mutant was not affected in biomineralization (presence of magnetosome, dimension of crystals, and number of magnetic particles). However, the mutant cells showed substantially reduced magnetic orientation in the  $C_{mag}$  assay (light scattering assay based on the ratio of maximum and minimum scattering intensities;  $C_{mag}$  wild type, 1.7;  $\Delta mamJ$ , 0.5) (Schüler et al., 1995) and TEM images revealed that the mutant no longer produced straight magnetosome chains, but that magnetite crystals were instead arranged in compact clusters (Figure 18).

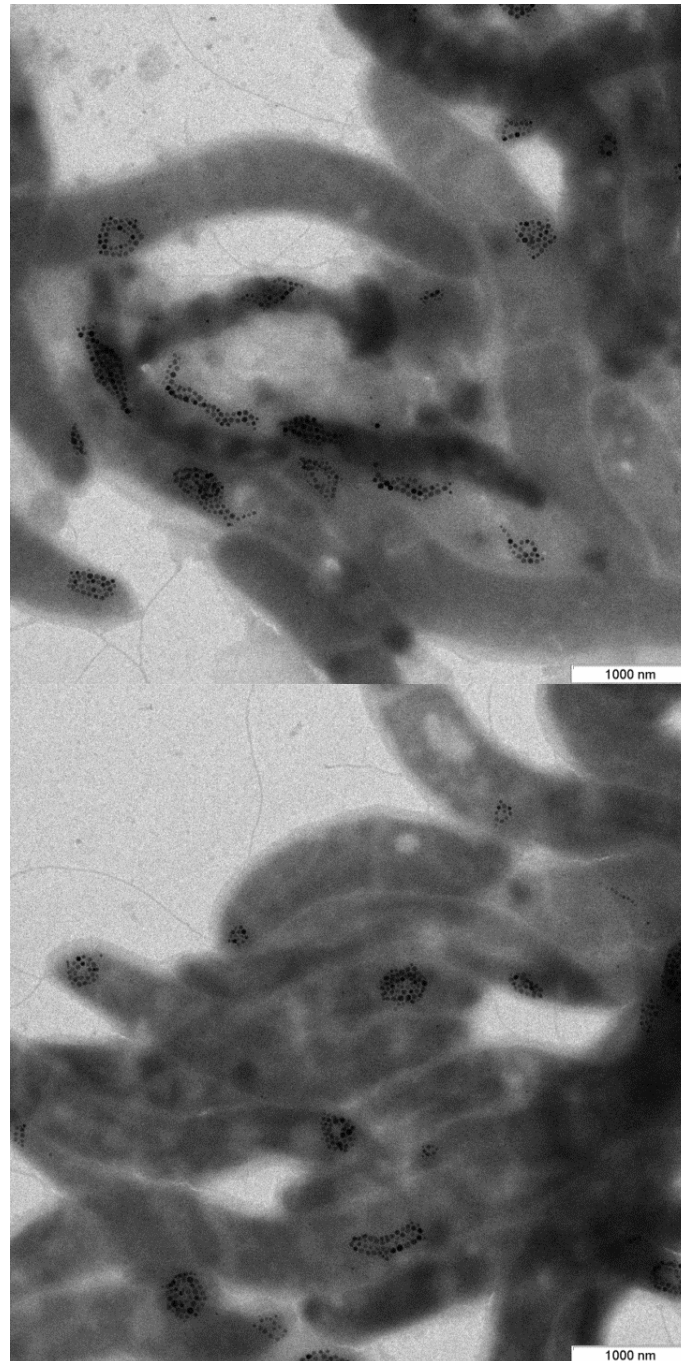


**Figure 18: TEM images of MSR-1  $\Delta mamJ$  mutant cells. Several organization can be recognized, varying from e.g. donut, cluster, or double-chain.**

We studied the dynamics of this cluster formation in order to possibly understand their mechanism of formation (Scheffel et al., 2006b). In contrast to what is observed in wild -type cells, the localization of immature crystals did not change significantly for more than 2 hours in  $\Delta mamJ$  mutant cells. The clustering of magnetosomes started only at about 3 hours, corresponding to the time where numerous larger particles were present. This indicated that the agglomeration of particles occurs at a later stage of crystal growth, and we proposed that it was probably caused by increasing magnetic attraction between SSD crystals arrived in close proximity to each other as observed in wild-type cells in our magnetic studies of chain formation (chapter 2.3.2).

Given the essential role observed for MamJ in the organization of magnetosome in linear assemblies or chains, we postulated at the time a mechanism that involved magnetic interactions within the chain, physical contact between adjacent particles, and the interaction of MamJ with a cytoskeleton-like structure that was observed by cryo-TEM (Scheffel et al., 2006b) and that could direct the assembly and localization of the prokaryotic organelles (Figure 19). Such a mechanism was nearly simultaneously proposed by a group of colleagues from California, where they also showed that the filamentous structure could be made of MamK (Komeili et al., 2006).

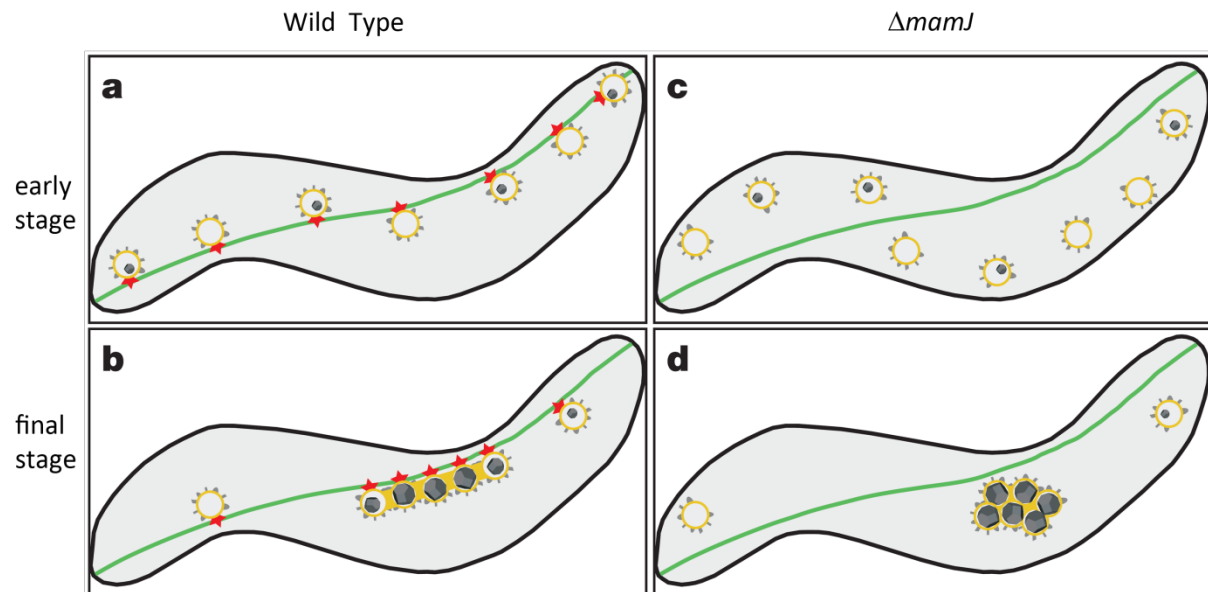


**Figure 19: Model for the magnetosome chain assembly.** MamJ (red) attaches the empty magnetosome vesicles (yellow) to the cytoskeletal filaments (green), resulting in a loosely spaced ‘beads-on-a-string’-like alignment. a, Magnetite biomineralization is initiated at multiple discrete sites distributed over the length of the cell. As magnetite crystals (black) continue to grow, their magnetic moments increasingly force the particles to interact. b, Positioning of mature magnetosomes at midcell is then directed along filaments. Once particles are in close contact, growing chains are further stabilized by interaction through the magnetosome membrane. c, In contrast, vesicles in the  $\Delta mamJ$  mutant are detached from the filaments. d, Vesicles are free to diffuse within the cells, resulting in agglomeration of particles upon close contact as magnetic interactions between growing magnetite crystals increase. Figure reproduced with permission from (Scheffel et al., 2006b).

The interaction between MamJ and MamK was thus postulated but was hardly demonstrated *in vivo*. Indeed, although experimental indications suggest the direct interaction between MamJ and MamK in MSR-1, this has not been undoubtedly demonstrated to date, since the interactions studied using the yeast 2-hybrid (Y2H) method are not fully demonstrative of a real interaction (Scheffel and Schueler, 2007). We thus decided in the course of the doctoral work of Maria Carillo and the post-doctoral work of Mathieu Bennet to reassess this postulated interaction *in vivo*. Fusion of MamK with mCherry together with MamJ with eGFP were thus imaged using fluorescence confocal microscopy and FLIM images were generated in order to calculate the FRET characteristics between mCherry and eGFP, hence to evaluate the interaction between MamK and MamJ (Carillo et al., 2013).

Images of *E. coli* expressing eGFP\_MamJ (Figure 20, (a),(b),(c)), MamK\_mCherry (Figure 20, (d), (e), (f)) and both eGFP\_MamJ and MamK\_mCherry (Figure 20, (g), (h), (i)) are shown in Figure 20. Each expression is presented on a separate row. The columns correspond to the different imaging



parameters. The first column (green channel) shows the images recorded with excitation at 488 nm and emission between 500 nm and 550 nm corresponding to the fluorescence emission of the eGFP protein, the second column (red channel) shows the images recorded with excitation at 561 nm and emission between 570 nm and 640 nm corresponding to the fluorescence emission of the mCherry protein. The third column is a transmission image of the sample.

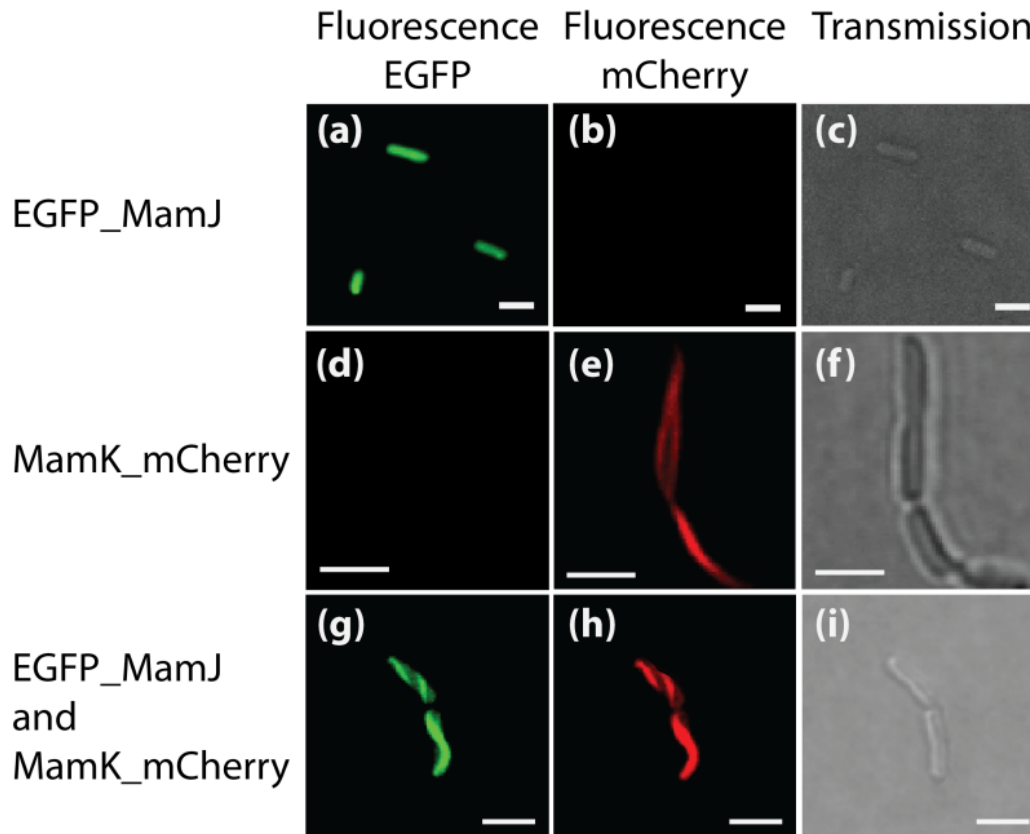


Figure 20: Fluorescence images ((a) and (b)) and transmission image (c) of *E. coli* expressing eGFP\_MamJ; fluorescence images ((d) and (e)) and transmission image (f) of *E. coli* expressing MamK\_mCherry; and fluorescence images ((g) and (h)) and transmission image (i) of *E. coli* expressing eGFP\_MamJ and MamK\_mCherry. The excitation and emission wavelengths were 488 nm and 500-550 nm ((a); (d); (g)); and 561 nm and 570 – 620 nm ((b); (e); (h)). Scale bar 2  $\mu$ m (figure from (Carillo et al., 2013)).

The fluorescence of eGFP\_MamJ protein is as expected in the green region of the spectrum (Figure 20(a)) and is homogeneously distributed in the entire cells (Figure 20 (c)) whereas the fluorescence of MamK\_mCherry is also as expected in the red region of the spectrum and its elongated spatial distribution is typical of that of a filament (Figure 20 (e)) extending across cells (Figure 20 (f)) as similar to the pattern observed by Pradel (Pradel et al., 2006b) and Komeili (Komeili et al., 2006). Figure 20 (g-i) show bacteria where MamK\_mCherry and eGFP\_MamJ were co-expressed. These are the bacteria that can be seen in the green and red channels Figure 20 (g) and (h). The first evidence for interaction between MamK\_mCherry and eGFP\_MamJ is found when comparing the localization of the fluorescence signal of the green and red channels. These show that the fluorescence of eGFP\_MamJ is no longer homogeneously distributed across the cell as in Figure 20a but rather emits from the same region as where the MamK\_mCherry filaments are found, effectively demonstrating

the reconstruction in *E. coli* of part of the protein assembly found in MSR-1. We expected to observe some free unbound eGFP\_MamJ in cells where MamK was expressed. This was however not the case and may result from a relative higher expression of MamK with respect to MamJ.

This observation is also evident in Figure 21 that shows the localization of eGFP\_MamJ (Figure 21a-c), eGFP with respect to MamK\_mCherry in the absence (Figure 21 d-f) and in the presence (Figure 21 g-i) of MamJ. In the absence of MamJ and/or MamK (Figure 21 a-f), the fluorescence from eGFP emanates from the entire cell whereas in the mutual presence of MamJ and MamK, this comes exclusively from the MamK filament.

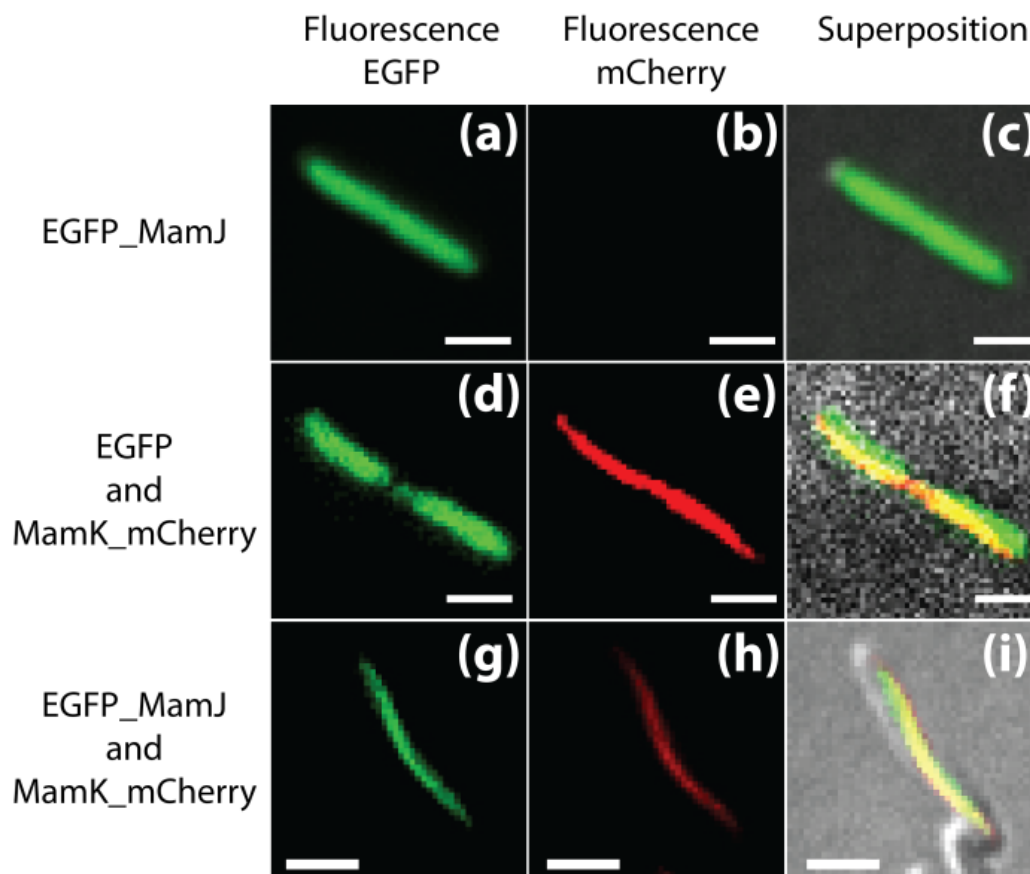


Figure 21: Fluorescence images of *E. coli* expressing: eGFP\_MamJ (a), (b) and (c) MamK\_mCherry and eGFP (d), (e) and (f) and MamK\_mCherry and eGFP\_MamJ (g), (h) and (i). Excitation and emission wavelength of eGFP, i.e. 488 nm and 500 to 550 nm (a), (d), and (g); excitation and emission wavelength of mCherry, i.e. 561 nm and 570 to 640 nm (b), (e) and (h). Superposition of image (a) and (b) on a transmission image (c); (d) and (e) on a transmission image (f); and (g) and (h) on a transmission image (i). Scale bar 2  $\mu\text{m}$  (figure from (Carillo et al., 2013)).

The control intensity imaging experiments we performed were all negative and the co-localization of eGFP and mCherry occurs only when both MamK and MamJ are co-expressed. Most importantly, the co-expression of eGFP and MamK\_mCherry does not lead to the arrangement of eGFP along the MamK filament (Figure 20 and Figure 21), a prerequisite to the validation of the FRET experiments. Figure 22 shows examples of the fluorescence lifetime images of *E. coli* expressing eGFP (b), MamJ\_eGFP (d), MamK\_mCherry and eGFP (f), and MamK\_mCherry and eGFP\_MamJ (h). The

decrease of eGFP fluorescence lifetime in the presence of MamK\_mCherry and eGFP\_MamJ indicates the occurrence of FRET between mCherry and eGFP, hence the interaction of MamJ and MamK.

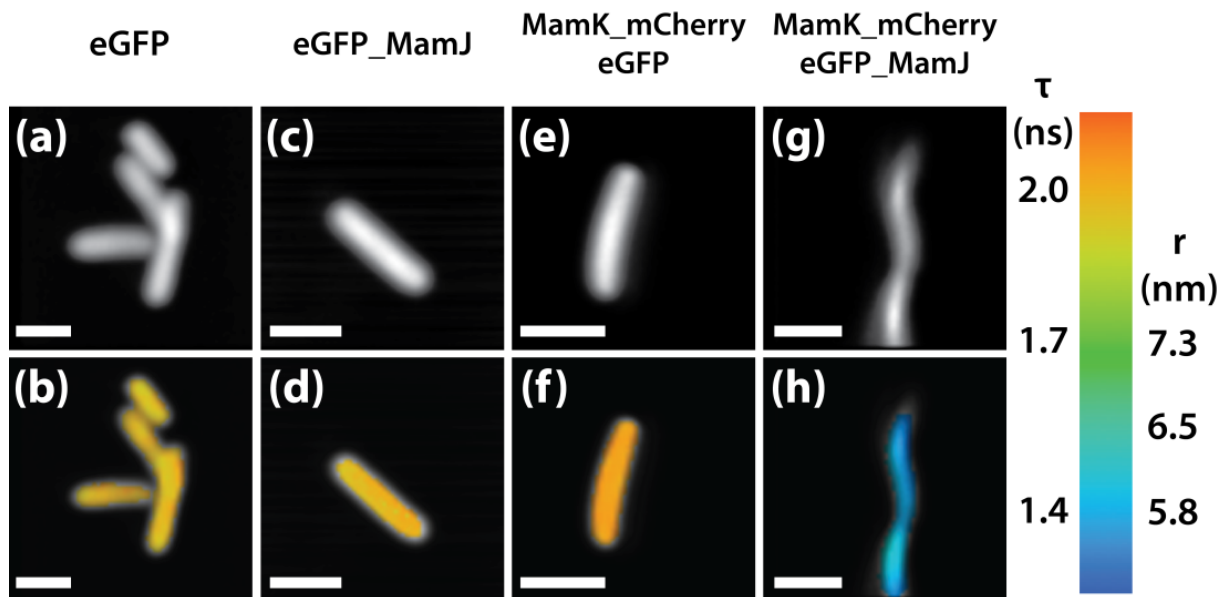


Figure 22: Fluorescence intensity and fluorescence lifetime images of *E. coli* expressing; eGFP (a) and (b); eGFP\_MamJ (c) and (d); MamK\_mCherry and eGFP (e) and (f); and MamK\_mCherry and eGFP\_MamJ (g) and (h). The color-coded scale bar is used to map the fluorescence lifetime of eGFP and the calculated separation distance between eGFP and mCherry. The fluorescence lifetimes range from 1.3 ns (blue) to 2.1 ns (red) and the separation from 5.5 nm (blue) to 7.3 nm (green). Scale bar 2  $\mu\text{m}$  (figure from (Carillo et al., 2013)).

As shown in previous experiments, MamK overexpressed in *E. coli* readily forms filaments (Komeili et al., 2006; Pradel et al., 2006b). Here, we have shown that the co-expression of MamJ and MamK leads to the co-localization of the two proteins along MamK filaments *in vivo*, effectively demonstrating the reconstruction of part of the protein assembly found in MSR-1 in a host organism. In addition, the presence of both proteins is essential to the formation of the magnetosome chain (Scheffel et al., 2006a) in *Magnetospirilla*. Using FLIM-FRET and the co-expression of MamK\_mCherry and eGFP\_MamJ in *E. coli*, we have demonstrated the molecular interaction between MamJ and MamK and show the large possibilities offered by this technique to study protein-protein interaction.

#### 2.3.4. Magnetism vs. genetics: Determining the main factor in magnetosome assembly using *in silico* mutants

From the previous chapters, it became evident that the formation of magnetosomes was indeed a complex process that consisted in the controlled biomineralization of magnetite in pre-existing vesicles and the synergic assembly of magnetosomes into chains. The detailed mechanism of this process was shown to involve both: specific biological control mechanisms (chapter 2.3.3) as well as generic physical processes and interactions such as the diffusion of magnetosomes in the cell and the

magnetic interactions between the nanocrystals (chapter 2.3.2). Several molecular players involved in the formation and assembly of magnetosomes have indeed already been identified. These included the cytoskeletal proteins MamK and MamJ that played a role in the assembly of magnetosome chains (Draper et al., 2011; Katzmann et al., 2010; Komeili et al., 2006; Scheffel et al., 2006b). Studies of the dynamics of magnetosomes formation and assembly in iron-starved cells, mostly of *Magnetospirilla* strains, also provided some constraints on the dynamics of the processes. It was for example shown that about 6 hours were necessary for the magnetosomes to grow and reach a mature size, and to assemble into the typical chain arrangement with narrowly spaced neighbor-crystallites (Carvallo et al., 2009; Faivre et al., 2007; Faivre et al., 2008). Moreover, it was hypothesized, based on FMR spectroscopy, that the crystals first growing over the critical superparamagnetic to stable single domain size threshold (~25 nm), act as 'magnetosome docks' and play a decisive role for the stabilization of the magnetic dipole and thus for chain formation (Faivre et al., 2010).

However, the numerous studies listed above could not determine how the physical interactions were coordinated with specific biological (transport) mechanisms. More specifically, questions remained on the role of magnetic interactions in the formation of the magnetosome chain. Are they, together with diffusive movements of the magnetosomes, sufficient for the formation of a chain? Likewise, what were the roles of specific, genetically encoded, factors? A minimal model for the role of the cytoskeleton in this context was therefore that the magnetosome filament provided a structural scaffold for the formation of a linear assembly of magnetosomes (Figure 19). However, the magnetosome filament and its structural component could also have a more dynamic function and be involved in directed transport, delivering magnetosomes to the site of the formation of a magnetosome chain. The minimal model of a purely structural role of the magnetosome filament was indeed challenged by recent observations that the MSR-1 *mamK* deletion mutant still formed magnetosome chains, although shorter than those of the wild-type strain, but was defective in assembling a single chain as well as in the midcell localization of magnetosomes (Katzmann et al., 2010). A more dynamic role of the magnetosome filament was also consistent with observations that MamK filaments are dynamic and depolymerize in an active, ATP-dependent fashion (Pradel et al., 2006a; Rioux et al., 2010; Sonkaria et al., 2012; Taoka et al., 2007).

Together with a colleague from the theory department of the MPIKG, we thus developed and used computer simulations of the formation of magnetosomes to address these questions (Klumpp and Faivre, 2012). The model integrated generic physical processes with specific biological functions. Specifically, it described the nucleation and growth of magnetite crystals, the diffusive and active transport of magnetosomes, and their magnetic interactions. The full theoretical description can be found elsewhere (Klumpp and Faivre, 2012). We used this model to simulate several scenarios of the dynamics of magnetosome formation and assembly (Figure 23). Simulating these scenarios allowed us to study '*in-silico* mutants' that had various physical processes and / or interactions turned on or off, in order to elucidate the roles of the different dynamic processes. In some cases, it may be possible to obtain corresponding experimental mutants by genetic modification, although it is currently not known which genes encoded proteins with the predicted functions. In other cases such as those with magnetic interactions turned off, it is very unlikely that such mutants can ever be generated experimentally at all. The simulations therefore allowed us to elucidate the roles of different molecular players, dynamical processes and physical interactions in a complementary manner to current experimental studies of magnetosome formation and assembly.

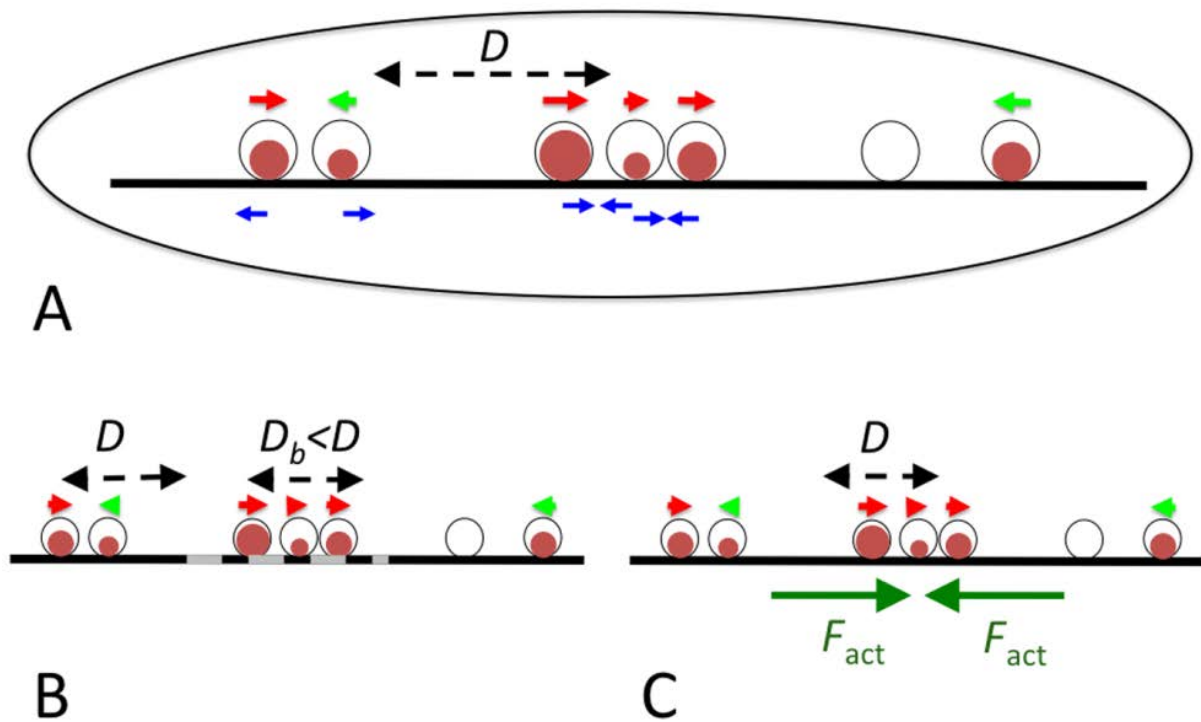


Figure 23: Model for magnetosome dynamics and scenarios of chain formation.

(A) The basic scenario: Magnetosomes are described by their position, the volume of the magnetite crystal they contain (brown circles) and the direction of their magnetic momentum (indicated by small red and green arrows). They move diffusively in one dimension, constrained by the cytoskeletal magnetosome filament along the cell axis, and interact through magnetic dipole-dipole interactions (A), which may either be attractive or repulsive (blue arrows). In other scenarios we simulate, the dynamics is modified by introducing a binding zone (dashed grey), in which diffusion is reduced by binding to the cytoskeleton (B), or active movement towards the center of the cell (C). Figure reproduced with permission from (Klump and Faivre, 2012).

We first studied whether magnetic interactions alone were sufficient to drive the assembly of magnetosome chains and therefore simulated the dynamics of magnetosomes in the absence of active movements. This case may correspond to the situation in a *mamK* deletion mutant. An inspection of the time traces of magnetosomes in a cell indicates that a large fraction of cells formed several shorter chains rather than a single long one (Figure 24A). We thus determined the average number of chains per cell (Figure 25A) and the fraction of cells that have formed a single chain (Figure 25B) after 10 hours to quantify this observation. Figure 25A showed that the average number of chains per cell decreased with increasing magnetosome mobility, but that it remained considerably larger than 1 for all values of the diffusion coefficient we simulated (black circles). In addition, our simulations indicated that cells forming more than 1 chain typically have chains with oppositely oriented magnetic moments (Figure 25C). Finally, we have determined the average distance of the center of mass of the magnetosomes from the center of the cell (Figure 25D) and found that magnetosomes were not well-centered in these simulations.

These observations showed that diffusive movements of magnetosomes in the force field generated by their magnetic interactions may lead to the formation of a single magnetosome chain, provided that magnetosomes were sufficiently mobile. However, without additional directional clues, the

chain will not be positioned properly in the center of the cell. We therefore concluded that diffusive magnetosome movements and magnetic interactions alone were not sufficient for the robust formation of a magnetosome chain.

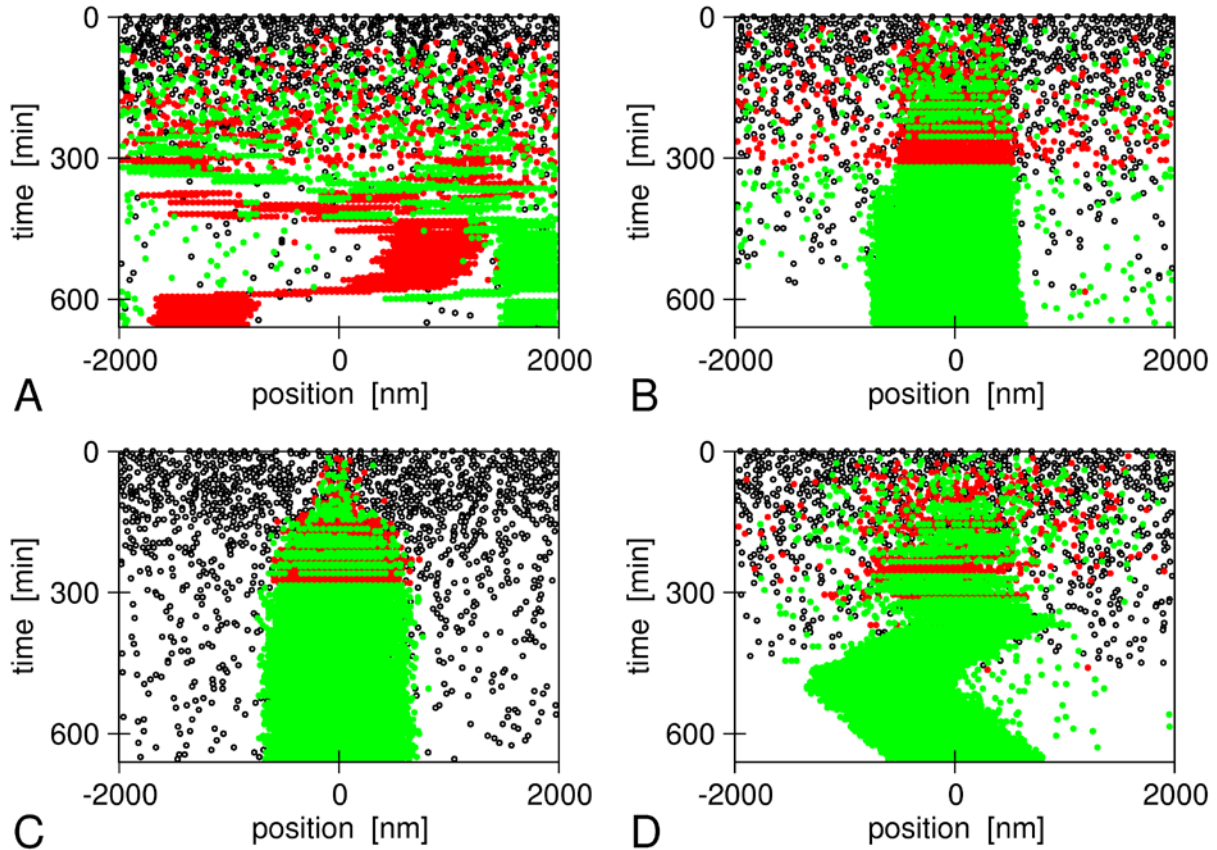


Figure 24: Example time traces of magnetosome formation in our simulations.

(A) Magnetic interactions and diffusion only, (B) binding zone in the cell center ( $L_b = 1000$  nm), (C) and (D) active transport to the cell center with an active force  $F_{\text{act}} = 1$  pN (C) and  $0.01$  pN (D). In all panels, black dots indicate empty magnetosome vesicles, green and red points indicate magnetosomes containing a crystal with plus or minus orientation of its magnetic moment. In all panels, the magnetosome mobility is given by  $D = 10^5$  nm<sup>2</sup>/s. Figure reproduced with permission from (Klumpp and Faivre, 2012).

We next asked how the diffusive dynamics of magnetosomes had to be amended to ensure the formation of a single chain in the center of the cell. We have first tested the possibility that binding sites for magnetosomes in the cell center serve as a nucleus for the formation of a single chain. The quantitative analysis of the structures formed after 10 hours showed that the results were almost the same as in the absence of such binding sites. With increasing magnetosome mobility however, we saw a faster decrease of the number of chains per cell in the presence of binding sites than in their absence (Figure 25A, dashed green and solid black lines, respectively), a stronger increase in the fraction of cells that have a single chain (Figure 25B), and a stronger decrease in the fraction of cells with chains of opposite polarity (Figure 25C). These observations depended on the length of the binding zone. When the lengths of the binding zone was reduced to  $L_b = 500$  nm, corresponding to binding sites for 10 closely packed magnetosomes, the presence or absence of these binding sites

made no difference for the formation of a single chain (compare the solid green line with the black lines in Figure 25A-C), indicating a rather strict requirements for the robust functioning of such mechanism. However, both the short and long binding zones concentrated the magnetosomes towards the center of the cell, as indicated by the position of their center of mass (Figure 25D).

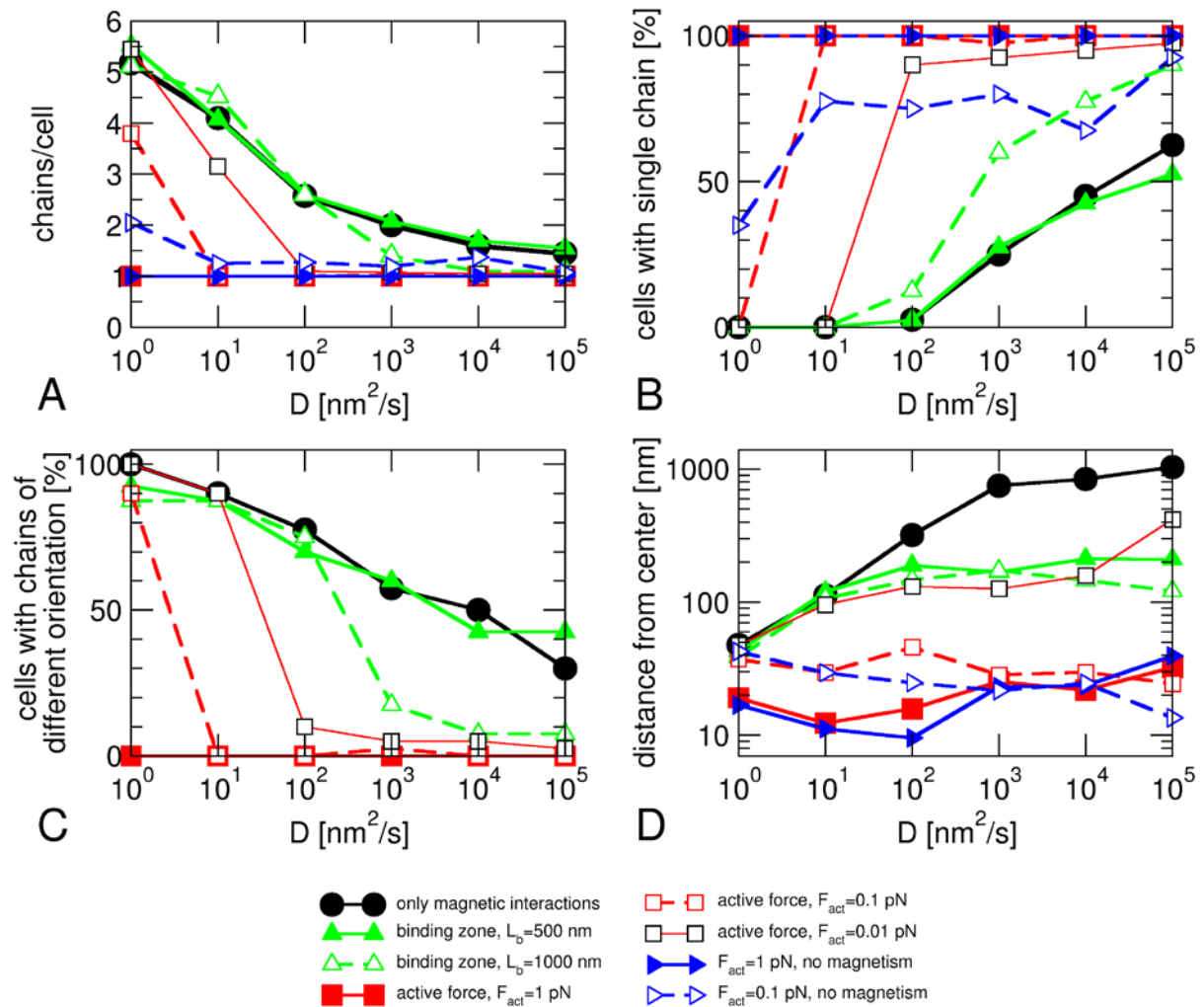


Figure 25: Analysis of the structures formed after 10 hours for different scenarios of magnetosome formation.

(A) average number of chains per cell, (B) fraction of cell with a single chain, (C) fraction of cells with chains that have opposite orientations of their magnetic moment, (D) average distance of the center of mass of the magnetosomes from the cell center, plotted as functions of the magnetosome mobility, which is characterized by the diffusion coefficient  $D$ . For each scenario and each value of  $D$ , 40 cells were simulated and analyzed. Figure reproduced with permission from (Klump and Faivre, 2012).

Another possibility was that active transport towards the center of the cell was responsible for chain assembly as well as for the positioning of the chain. Such a mechanism might for example be driven by the polymerization or depolymerization of cytoskeletal filaments such as MamK. This case corresponded to the situation in wildtype cells. As in the case of defined binding sites for chain nucleation, such a mechanism required that the cell could determine its center. Figure 24C showed an example of a simulation with an active force of 1 pN. Essentially all magnetosomes that had

nucleated a crystal were found in the center of the cell, in contrast to the case with a binding zone shown in Figure 24B. Initially both magnetic orientations coexisted, but as the crystals kept growing, the magnetic interactions became stronger and forced the magnetosomes to align in one chain. The chain as a whole was rather immobile in the center of the cell, but individual magnetosomes from both ends of the chain could be seen to make diffusive excursions away from the chain. For a lower active force, these diffusive excursions were bigger, and we also observed diffusive movements of the whole chain (Figure 24D). The presence of an active force decreased the average number of chains per cell (Figure 25A) and increased the probability that a cell formed a single chain (Figure 25B) compared to both the case with only magnetic forces and the case of a binding zone for chain nucleation. It also resulted in better-centered chains than both other models (Figure 25D). We therefore concluded that active transport can account for both the formation of a single magnetosome chain and its central positioning.

Finally, we simulated crystals without a magnetic moment, but subject to active transport to test what role the magnetic interactions had in the process. This type of ‘mutation’ is extremely unlikely to be realized experimentally as a mutant forming non-magnetic mineral would have to be generated. The results for the number of chains per cell (Figure 25A) and the centering of the magnetosome chain (Figure 25D) were very similar as in the presence of magnetic interactions, but for small active forces, the number of chains per cell was slightly increased in the absence of magnetic interactions and the probability of finding only one chain was reduced by approximately 25% (dashed red and blue lines in Figure 25A and B). We interpreted these observations as reflecting the lower cohesiveness of chains, as the magnetosomes became more mobile and can more easily make diffusive excursions away from the chain. This result was in agreement with observations from FMR spectroscopy that also suggested a role for magnetic interactions between magnetosomes for the stabilization of the chain (Faivre et al., 2010). Our simulation results thus suggested that attractive magnetic interactions were not the main driving force for the formation of the magnetosome chain, but rather played a role in stabilizing the chain, after active transport had brought magnetosomes in close proximity.

Besides all the case studies presented above, the simulations allowed us to make two complementary suggestions. First, the structures we found in our simulations of magnetosome dynamics without active movements strongly resembled recent observations of a *mamK* deletion mutant in *M. gryphiswaldense* (Katzmann et al., 2010) and in *M. magneticum* (Komeili et al., 2006). Cells of these strains did not form MamK filaments, and had a smaller numbers of magnetosomes. Most interestingly, however, formation of magnetosome chains was observed despite the absence of MamK, but about half of the cells contained 2 – 4 short chains rather than one long chain (Figure 26), and chains are displaced from midcell (Katzmann et al., 2010). Our model thus suggested an interpretation of the *mamK* phenotype as the loss of or a defect in the active transport of magnetosomes towards the cell center. In that case, short chains may form in multiple locations in the cell. These short chains moved too slowly to merge into a single chain by diffusion and build up independent magnetic moments, which may provide additional barriers for the concatenation of two chains if they had opposite orientation. We noted that, while these observations pointed to a crucial role of MamK for the active movements of magnetosomes, the mechanistic role of MamK remained an open question. MamK was indeed a candidate for the motor protein that generated force and drove active magnetosome movements, but it may also have some other function that was required for these movements.



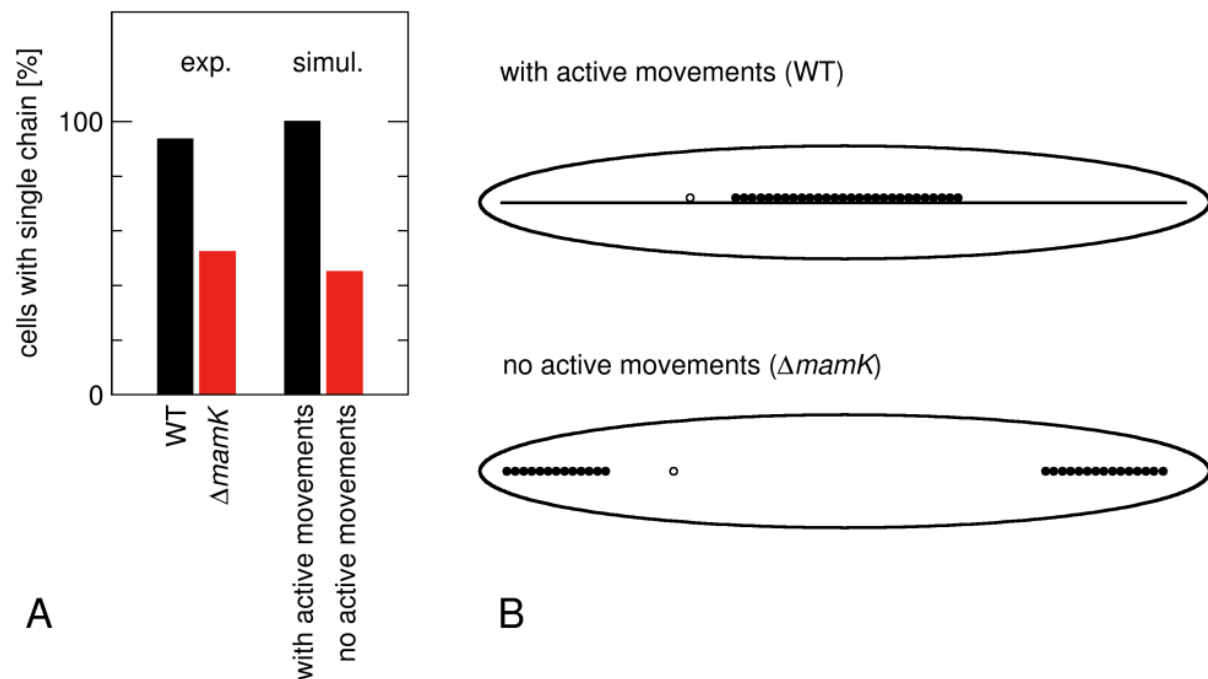


Figure 26: Comparison of chain formation in simulations and experiments.

(A) Fractions of cells with a single chain as observed from electron microscopy images of *M. gryphiswaldense* wild type and  $\Delta mamK$  cells (Katzmann et al., 2010) and from our simulations with and without active movements of magnetosomes (data from Figure 25B, with  $D = 10^4 \text{ nm}^2/\text{s}$  and  $F_{\text{act}} = 0.1 \text{ pN}$ ). (B) Examples of magnetosome structures formed in these simulations. These structures are very similar to those seen in electron microscopy images of (Katzmann et al., 2010). Figure reproduced with permission from (Klumpp and Faivre, 2012).

Secondly, our simulations indicated that a coupling between the activation of biomineralization in a vesicle and the activation of its active transport was required in order to reproduce the dynamics of chain formation that is observed experimentally in *M. gryphiswaldense*, where crystals were nucleated in magnetosome vesicles throughout the cell before a chain of magnetosomes was formed (Faivre et al., 2007; Faivre et al., 2010; Faivre et al., 2008). Without such coupling, our simulations rapidly formed chains of empty magnetosome vesicles as observed in *M. magneticum* (Komeili et al., 2004), but not *M. gryphiswaldense*. The simulations therefore suggested that an important mechanistic difference between these related species may be based on the presence or absence of such coupling of the activation of magnetosome mobility and the activation of biomineralization.

## 2.4. Magneto-aerotaxis

The presence of the magnetosome chain is supposed to act as compass needle on the cell body. Thereby, the magnetotactic bacteria passively align with the Earth magnetic field lines thanks to their intracellular magnetic dipole. The biological advantage provided by the magnetic assembly onto magnetotactic bacteria as opposed to non-magnetic bacteria is the simplification of their taxis for an appropriate environment from three-dimensions to quasi-one-dimension.

However, if magnetotaxis and aerotaxis were linked earlier (Frankel et al., 1997; Frankel et al., 2007; Smith et al., 2006b), a clear description of the behavior together with a quantification of the physiological aerotactic need of the cells were not performed. The correlative study of the tactic response of microorganisms in controlled physiological environments indeed requires the non-invasive sensing of the chemical micro-environment and the observation of the micro-organisms' response at both single cell and cell population levels, requirements that have yet to be satisfied.

In the framework of the post-doctoral work of Mathieu Bennet, we have devised a platform dedicated to the study of micro-organisms response to micro-environmental changes to remedy the shortcomings of the current techniques (Bennet et al., submitted). The platform is constructed entirely from non-magnetic materials and hosts triaxial Helmholtz coils that generate magnetic fields with a precision of  $\pm 5\%$  of the Earth's magnetic field. Our method allows the simultaneous correlative mapping of the micro-environmental properties and recording of the characteristic response of the bacteria at the cell and population level. Physiological characteristics and magneto-aerotactic behaviour of the bacteria are calculated using a modified diffusion model and a revised model for magneto-aerotaxis, respectively. As a case study, we have worked on the magneto-aerotaxis of *Magnetospirillum gryphiswaldense* MSR-1 (Schleifer et al., 1991b).

MSR-1 bacteria were grown, selected for their motility and transferred to a fluorescent medium. They were then loaded into a microcapillary (Figure 27a) that is open at one end (left hand side), through which air diffuses in, and sealed at the other end with petroleum jelly. This resulted in the formation of an oxygen gradient, and with time an aerotactic band that formed a few millimetres away from the air interface. The capillary was placed on the microscope stage under a controlled magnetic field. The oxygen concentration was mapped using wavelength-ratiometry fluorescence imaging. The aerotactic band position, the distribution of bacteria and the oxygen concentration along the capillary were measured in time steps of 30 minutes for two hours. A total of five magnetic field conditions were applied:

1. the Earth's magnetic field is cancelled. This condition is equivalent to bacteria finding their preferred environment by aerotaxis alone;
2. the magnetic field is set to 50  $\mu\text{T}$ , parallel to the oxygen gradient and pointing to the sealed end of the capillary. This condition is equivalent to bacteria placed at the Earth's magnetic pole;
3. the magnetic field is set to 500  $\mu\text{T}$ , parallel to the oxygen gradient and pointing to the sealed end of the capillary. This condition is geographically similar to 2 with a 10-fold increase of the field strength;
4. the magnetic field is set to 50  $\mu\text{T}$ , at  $45^\circ$  to the oxygen gradient and pointing to the sealed end of the capillary. This condition is similar to bacteria placed, for instance, in North Africa, or in Mexico;
5. the magnetic field is set to 50  $\mu\text{T}$ , perpendicular to the oxygen gradient. This condition is similar to bacteria placed at the equator.

As an example, Figure 27b shows the typical concentration profile of oxygen ( $\text{O}_2$ ) in the capillary at 30, 60, 90 and 120 minutes after sample preparation performed for condition 2 (See also Fig.S6 for other conditions). The position of the band over time is indicated by a bar, whose colour matches that of the oxygen measurement. The oxygen concentration at the air / medium interface is 216  $\mu\text{M}$ , then decreases as the position of the aerotactic band is approached and remains relatively constant after the band.

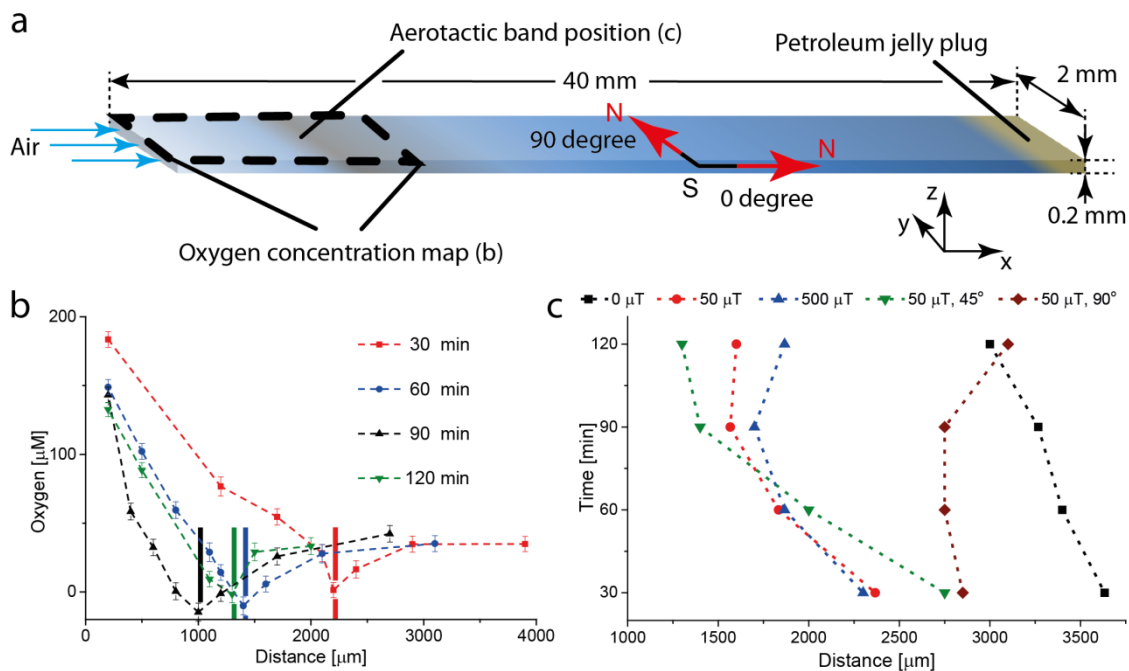


**Figure 27:** a: Schematic of the capillary showing the generation of an oxygen gradient due to air diffusion at one end of the capillary, the consumption by the bacteria at the aerotactic band position shown in c, and the jelly plug at the other end of the capillary; the area corresponding to the oxygen gradient measured and shown in b; a schematic of the magnetic field conditions corresponding to 50  $\mu\text{T}$ , at 0° and 90° to the length of the capillary; and the orientation of the x, y- and z-axis according to how they are referred to in the text. b: Graph showing the evolution of the oxygen gradient generated and the position of the bacteria in the capillary following the sample preparation. The measurements are performed after 30 min (red square); 60 min (blue circles); 90 min (black triangles); and 120 min (inverted green triangle). The aerotactic band position is marked by a bar the colour of which corresponds to the colours used to plot the gradients. c: Position of the aerotactic band when the Earth's magnetic field is cancelled (black squares), a magnetic field of 50  $\mu\text{T}$  is applied and the North pole points towards the anaerobic region (red circles), a magnetic field of 500  $\mu\text{T}$  is applied and the North pole points towards the anaerobic region (blue triangles), a magnetic field of 50  $\mu\text{T}$  is applied and the North pole points at 45° to the capillary long axis towards the anaerobic region (green reverse triangles), a magnetic field of 50  $\mu\text{T}$  is applied and the North pole points at 90° to the capillary long axis (brown squares). Each point represents the position of the aerotactic band at a given time after the beginning of an experiment averaged over three distinct experiments.

The position of the aerotactic band over the time course of the experiment is averaged for three sets of data and shown in Figure 27c. Three main trends are observed. If the magnetic field is applied pointing towards the anaerobic region (Figure 27c, 50  $\mu\text{T}$  and 500  $\mu\text{T}$ ) or at 45° to the long axis of the capillary (Figure 27c, 50  $\mu\text{T}$ , 45°), the bacteria converge towards a distance of ca. 1.6 mm from the air / solution interface. A convergence also occurs when the magnetic field is cancelled. However this happens much more slowly than in the former cases and after 120 minutes the band is further away from the open-end of the capillary, at 3 mm from the air interface. Finally, we did not observe reproducible aerotactic behaviour when the magnetic field is applied at 90° to gradient. In this condition, several bands are eventually observed, some moving towards and some away from the oxygen diffusion front, sometimes bands merge. For this condition, Figure 27c shows the position of the band observed closest to the open-end of the capillary.

We can readily conclude that the spatial organisation of magnetotactic bacteria colonies in a gradient environment is influenced by the presence and the direction of a magnetic field. Whereas the

colonies reach an equilibrium position after 90 minutes when the field has a component along the gradient, it takes longer for the bacteria to reach such a position when they are left only with the aerotaxis to guide their quest, experimentally showing the advantage of the combined magneto-aerotaxis in these conditions. Finally, when the magnetic field is perpendicular to the chemical gradient, multiple bands are observed and the system does not converge to an equilibrium position.

The mean oxygen concentration at which the bacteria form a band was extracted from the model we built by overlap between the bacterial spatial distribution and the oxygen profile (Bennet et al., submitted). The full theoretical description can be found elsewhere (Bennet et al., submitted). We only present here how this model was applied for a better understanding of magneto-aerotaxis. The mean oxygen concentration is  $1.5 \pm 0.1 \mu\text{M}$  when there is no magnetic field (condition 1),  $2.7 \pm 0.1 \mu\text{M}$  and  $3.6 \pm 0.2 \mu\text{M}$  for the bacteria subjected to a magnetic field of  $50 \mu\text{T}$  (condition 2) and  $500 \mu\text{T}$  (condition 3) respectively. These values are in good agreement with previously published preferred oxygen concentrations for microaerophilic bacteria (between 1 and  $10 \mu\text{M}$ ) (Thar and Fenchel, 2005). The oxygen consumption rate, which was the fitted parameter of our model, is ca.  $0.1 \text{ fmol} \times \text{min}^{-1}$  per MSR-1 cell and this is comparable to that measured in bulk for *Azospirillum lipoferum* ( $0.2 \text{ fmol} \times \text{min}^{-1} \times \text{cell}^{-1}$ ) (Alexandre et al., 1999). The final width of the aerotactic band is also dependent on the magnetic field strength. This is  $9.1 \pm 0.5 \mu\text{m}$  at  $500 \mu\text{T}$ ,  $11 \pm 1.6 \mu\text{m}$  at  $50 \mu\text{T}$  and  $17 \pm 2 \mu\text{m}$  at  $0 \mu\text{T}$ .

A simple interpretation of our experimental results is that a magnetic field with a significant component along the direction of the oxygen gradient simplifies and speeds up the formation of an aerotactic band by defining a single axis along which the bacteria search for the preferred oxygen concentration. To test this idea more quantitatively, we developed a model for the dynamics of the distribution of bacteria and the oxygen concentration. The model, which is based on earlier models for aerotaxis and magneto-aerotaxis (Mazzag et al., 2003; Smith et al., 2006a), describes movement of the bacteria in one dimension, distinguishing leftward moving and rightward moving, which swim up or down the oxygen gradient, respectively.

The model shows a sharp band of bacteria that forms within 5 min and then moves towards the open end of the capillary within 60 to 80 min (Figure 28A and B). We varied the swimming velocity  $v$  to mimic the effect of a magnetic field under an angle with the gradient (Figure 28B). Reducing the velocity, the shift of the band to its stationary position is slowed, but eventually the stationary position is established. For velocities down to  $10 \mu\text{m/s}$ , the stationary position is reached within the experimentally observed time scale, but not for  $5 \mu\text{m/s}$ . Under the strongly simplifying assumption that all bacteria move exactly along the direction given by the magnetic field, the velocity can be related to the angle  $\phi$  between field direction and gradient direction as  $v = v_{max} \cos\phi$ . With this assumption, these velocities correspond to angles of  $60^\circ$  and  $75^\circ$ , respectively, thus the behaviour seen in the model is consistent with the experiments where little difference was seen for angles of  $0^\circ$  and  $45^\circ$ . No band will form for an angle of  $90^\circ$ , while the absence of a magnetic field should lead to a mixture of all angles, and thus a slower formation of the band.

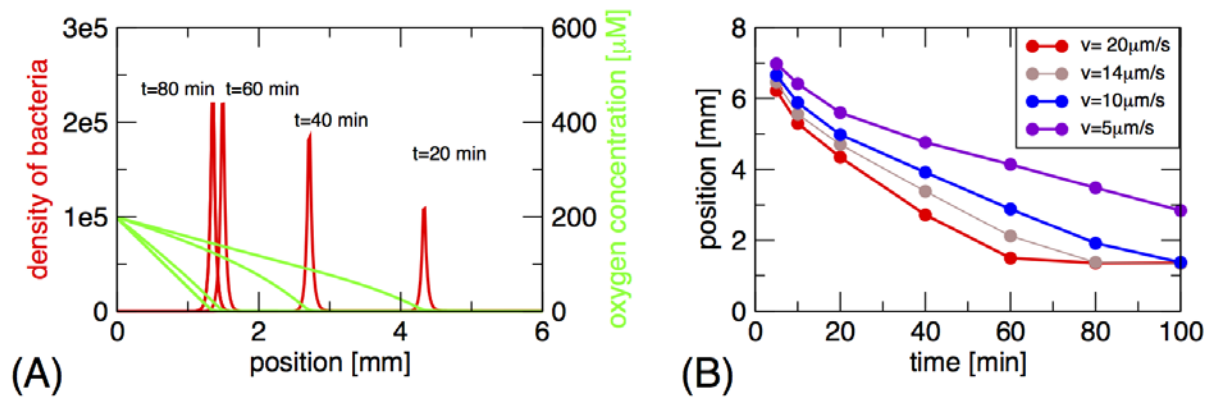


Figure 28: Formation of the aerotactic band in a model for magneto-aerotaxis: (A) Density profile of the bacteria (sharp band, shown in red) and of the oxygen concentration (green) at different time points. The parameter values for the simulations are as given in Table S1, corresponding to a magnetic field parallel to the oxygen gradient. (B) Position of the aerotactic band as a function of time for different bacterial swimming speeds. A magnetic field at an angle to the oxygen gradient can be interpreted as effectively reducing the swimming speed in the direction of the gradient (the projected swimming speed). Under this simplifying assumption the four speed values correspond to angles of  $0^\circ$ ,  $45^\circ$ ,  $60^\circ$ , and  $75^\circ$ .

Using a custom-made microscope platform, we have studied the behaviour of magneto-aerotactic bacteria in a monitored oxygen landscape under physiological magnetic fields. We found that not surprisingly, the presence of a magnetic field influences the characteristics of the aerotactic band but also more surprisingly its position in an oxygen gradient. In the absence of a magnetic field, the bacteria are only relying on their aerotaxis to find an optimal environment. The population migration is much slower than when the aerotaxis is assisted by a magnetic field. A one-dimensional model of aerotaxis is sufficient to semi-quantitatively describe the behaviour of magnetotactic bacteria colonies in an oxygen gradient; i.e., to show that an increasing average bacteria orientation angle with respect to the oxygen gradient leads to a reduced effective aerotactic speed, hence a slower colony organisation.



## 3. Synthetic formation and use of magnetite

The chemistry of the magnetite formation process and particularly under biomimetic (physiological conditions such as room temperature and atmospheric pressure) was only vaguely studied when this work started. Both ferrous and ferric iron oxides are considered insoluble in water around neutral pH. Soluble iron concentrations without complexing agents indeed lie below the micromolar range in the physiologically relevant pH range of 4 – 10 (Cornell and Schwertmann, 2003a). The magnetite phase forms under mildly reducing conditions ( $E_h \sim -0.2$  to  $-0.4$  V) and under alkaline pH > 8 (Faivre and Schüler, 2008; Winklhofer and Petersen, 2007). Most likely, magnetotactic bacteria form the intracellular compartments for the synthesis of magnetite in order to provide the necessary conditions. However, the precise chemical parameters under which the mineralization occurs *in vivo* are unknown. Various magnetite mineral precipitation mechanisms have been proposed. Initial assumptions after the discovery of magnetite biomineralization involved an amorphous or low crystallinity mineral precursor such as an amorphous ferrous oxyhydroxide or ferrihydrite, which is subsequently transformed into magnetite by oxidation or reduction, respectively (Frankel et al., 1983). As it was shown that magnetotactic bacteria are able to take up iron in both its divalent and trivalent form, the formation *via* co-precipitation of ferrous and ferric iron has also been proposed (Faivre et al., 2007; Schüler and Baeuerlein, 1996). But at room temperature and atmospheric pressure, the synthetic pathway typically used by chemists, the coprecipitation method (Massart, 1981), uses pH typically larger than 9 (Vayssières et al., 1998), at the limit of the physiological range and only producing particle smaller than 20 nm, far from the 30 nm size range necessary to obtain SSD properties. A controlled crystallization setup was thus developed in order to study how magnetotactic bacteria can control the size of the magnetosome and to test the effect of proteins of magnetotactic bacteria on magnetite formation *in vitro*.

### 3.1. Magnetite formation “in the beaker”

#### 3.1.1. The mechanism of magnetite nucleation and growth in the absence of additives

Understanding crystal formation is of fundamental interest and essential for a broad area of scientific disciplines as it might help for example chemists to understand how small building blocks preferentially assemble, materials scientists to develop morphological and shape control of synthetic

materials, geo-scientists to better apprehend the origin and formation of minerals, and biologists to understand how biomineralizing systems function. With the recent advancement of nanoscience, it was recognized that crystallization most probably not only simply occurs *via* the attachment of single atoms, ions or molecules but can also proceed through the aggregation, attachment and assembly of small, mostly poorly-structured clusters or crystalline nanoparticles. Mechanisms that involve such precursors have been termed „non-classical”, as they – so far – could not be explained within the framework of the classical nucleation and growth theory (Cölfen and Antonietti, 2005).

We developed an experimental setup for the precipitation of magnetite under controlled physicochemical conditions to monitor its rapid nucleation and growth (Figure 29). The setup was established based on earlier mineral formation studies (Faivre et al., 2005; Gebauer et al., 2008; Vayssières et al., 1998). Briefly, it allowed the controlled dispensing speed of an iron precursor solution into alkaline media at controlled and constant pH. The pH was kept constant by addition of sodium hydroxide under the control of a pH electrode. The temperature was controlled by the use of a water bath and the whole system operated under atmospheric pressure but under argon or nitrogen flow. The growth behavior under different pH conditions was initially investigated to determine conditions, which best mimicked biogenic particle formation. Particle growth of the nucleated crystalline phase was tracked by synchrotron-based X-ray diffraction and electron microscopy. After recognizing the non-classical properties of our process during the doctoral work of Jens Baumgartner, we in addition investigated the early stages of the mineralization by high resolution cryogenic transmission electron microscopy in collaboration with the group of N. Sommerdijk (TU Eindhoven) (HR cryo-TEM). This technique allows the imaging of the involved species in their quasi-native hydrated state as present in solution (Dey et al., 2010; Pouget et al., 2009; Yuwono et al., 2010). This allowed us to propose a model based on classical nucleation theory that might explain the characteristics features we observed and more generally that of any non-classical growth process.



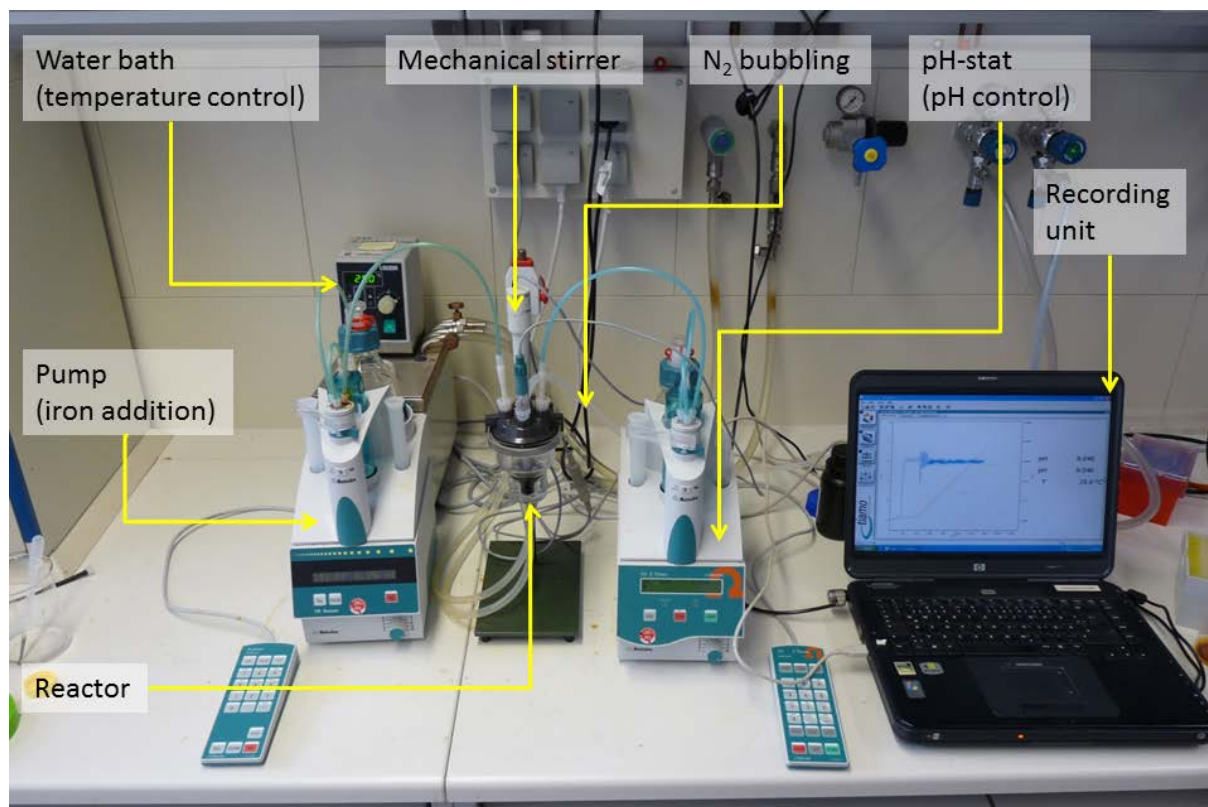


Figure 29: set-up used for the biomimetic syntheses.

Magnetite was crystallized using the above described set-up at pH = 8, 9, 10 and 11 by addition of a 1 M Fe solution at a rate of  $1 \mu\text{l min}^{-1}$  (Baumgartner et al., 2013a; Baumgartner et al., 2013b). Samples were taken in hourly intervals and analyzed by synchrotron powder X-ray diffraction for crystallinity and particle size by calculations using the Scherrer equation. Experiments were run in triplicate to analyze the internal variability. The diffractograms showed broader peaks for magnetite particles precipitated at higher pH values (Figure 30A and B). Furthermore, the diffractograms showed continuous peak narrowing with time indicating growth of the crystalline domains (Figure 30C and D) (Baumgartner et al., 2013a).

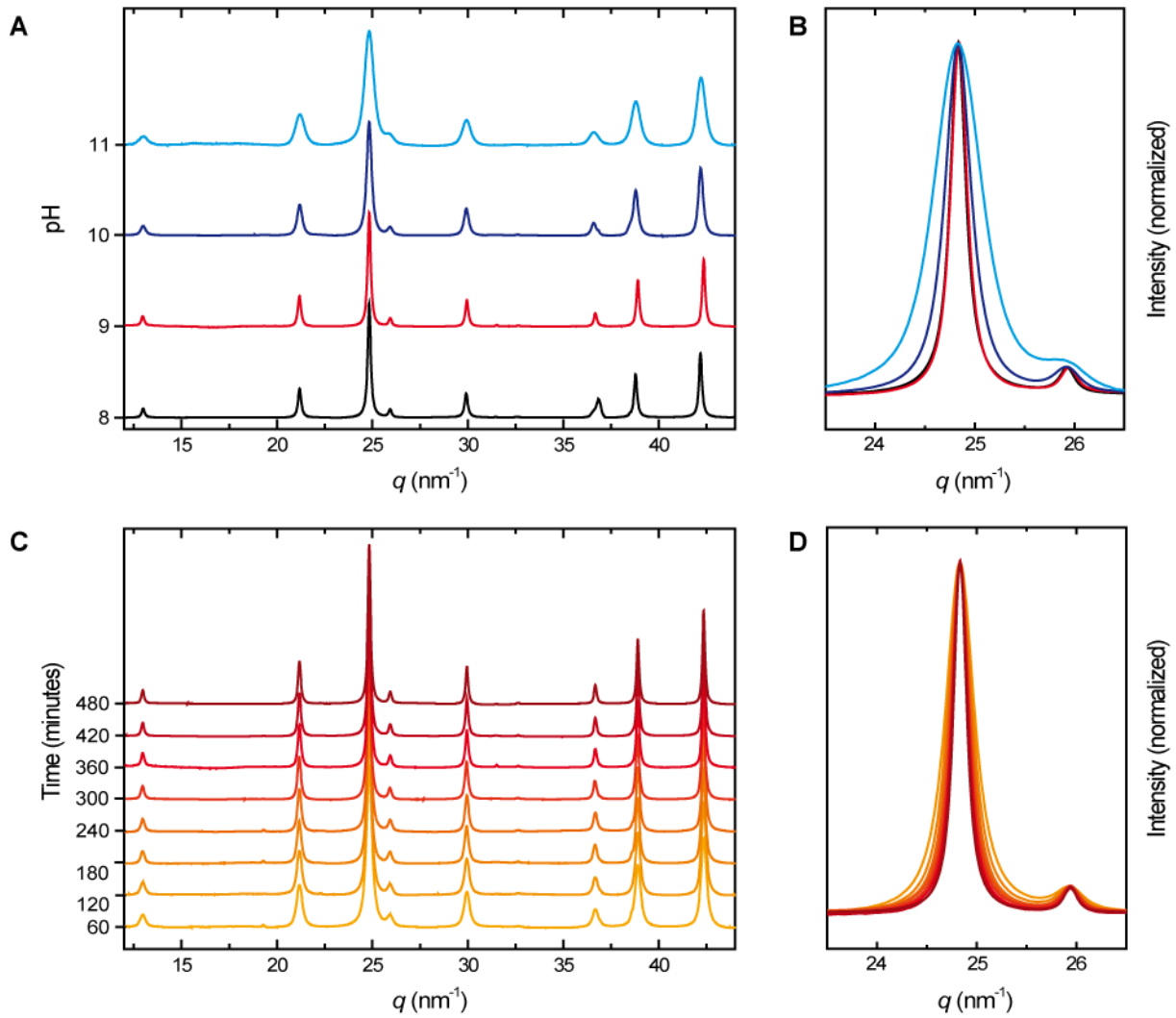


Figure 30: X-ray diffractograms of magnetite nanoparticles formed at different pH and time points. (A, B) diffraction patterns of particles grown for 360 min show increasing peak broadening with rising pH. (C, D) peak narrowing over time for particles grown at pH = 9.

The crystallite mean domain sizes were determined from peak broadening of the magnetite (311) reflection (Figure 30). The results for different pH values are plotted in Figure 31 as a function of time.

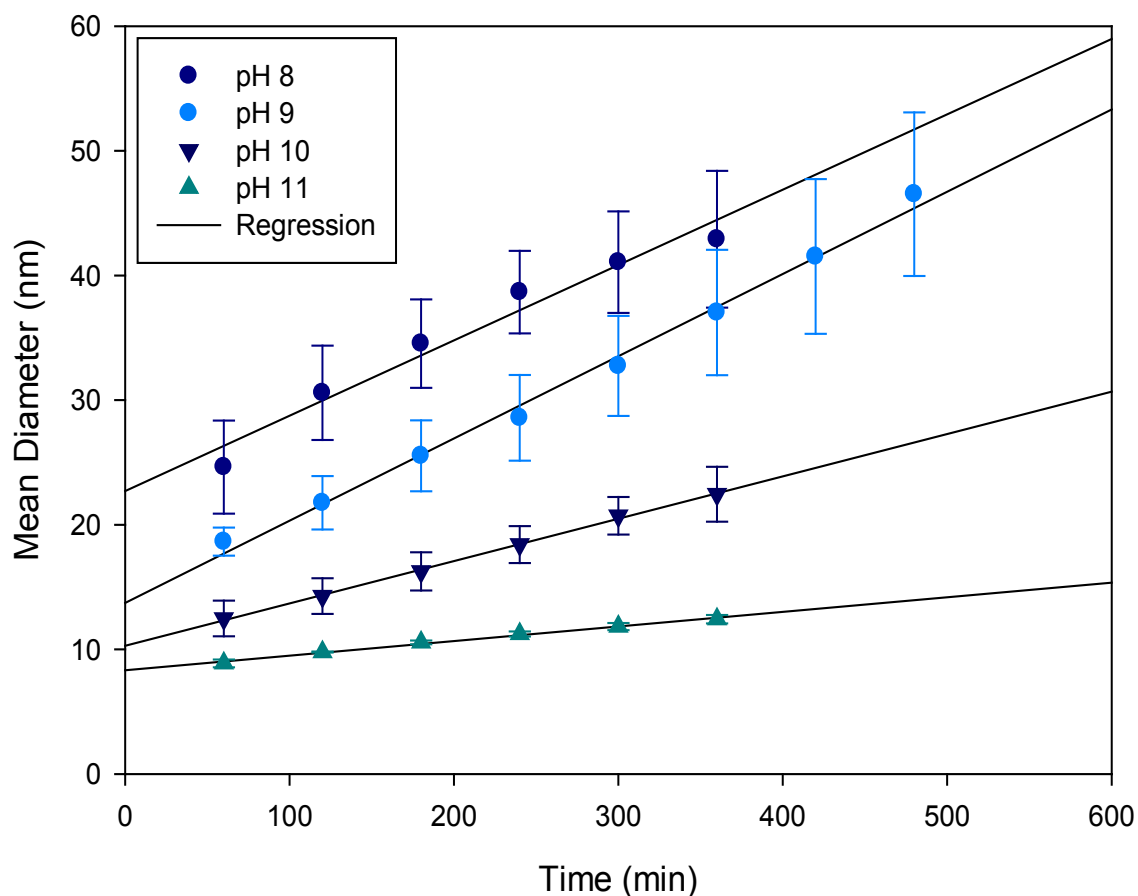
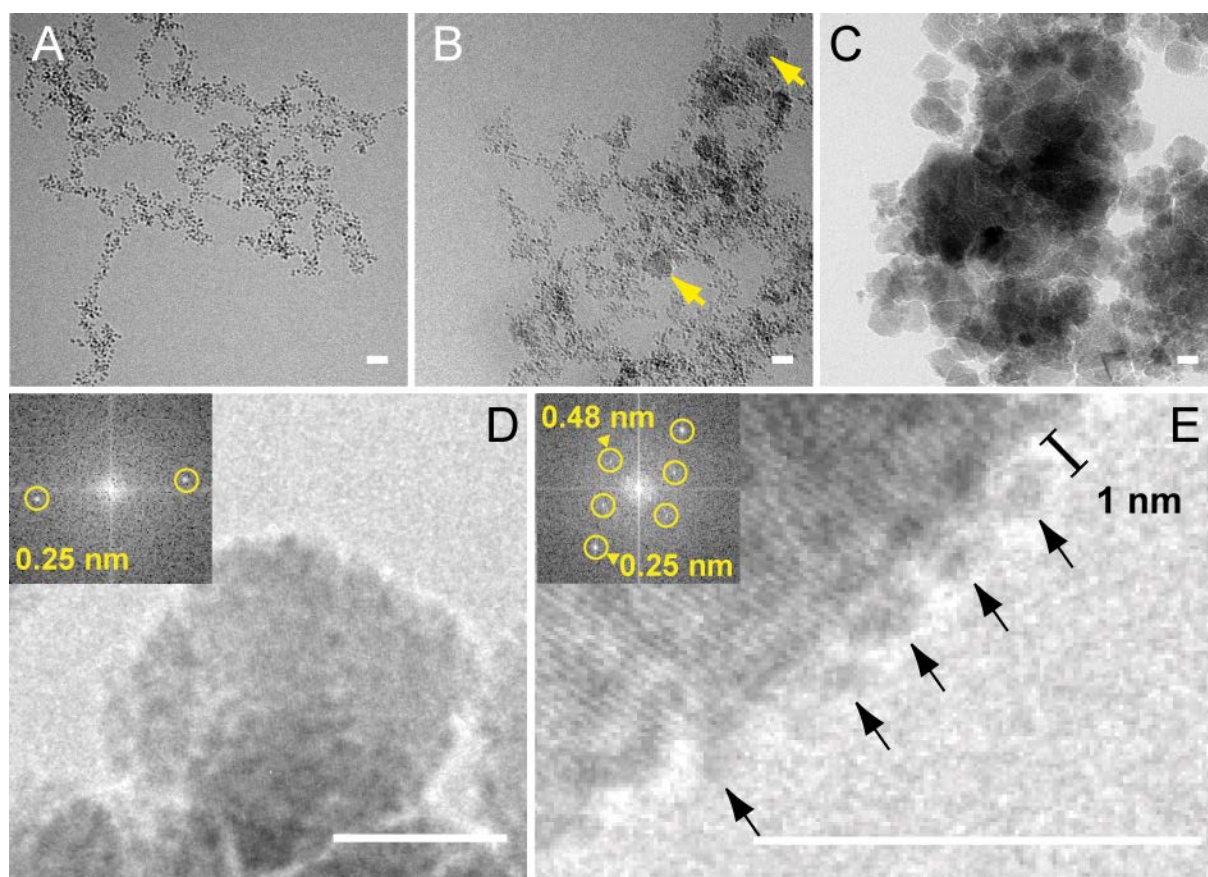


Figure 31: Magnetite nanoparticle growth at different pH. Mean values from three independent reactions. Error bars represent standard deviation.

It can clearly be seen that the growth kinetics of magnetite is influenced by the pH. The initially observed size is pH-dependent with smaller particles at increasing alkalinity. Furthermore, faster continuous growth occurs at lower pH with pH = 8 and pH = 9 showing similar behavior. The particularly interesting size range from 20 nm upwards is reached within one hour by particles grown at pH = 8, after two to three hours at pH = 9 and after six hours at pH = 10. Magnetite precipitated at pH = 11 did not reach the ferrimagnetic size threshold within the investigated time.

Figure 32 shows a typical time series of the nucleation and growth process at pH 9 as imaged by cryo-TEM, where magnetite formation followed a crystallization pathway involving the intermediate formation of nanometre-sized primary particles that fused to form the crystalline iron oxide phase.



**Figure 32: Cryo-TEM images of the nucleation and growth process of co-precipitated magnetite. Time series of the evolving primary particle and magnetite nanoparticle aggregates as imaged after (A) 2 minutes, (B) 6 minutes and (C) 82 minutes. Yellow arrows in B indicate early formed crystalline magnetite nanoparticles. (D) Image of a magnetite nanoparticle as in (B), inset: FFT indicating the crystallinity of the particle. (E) Image of primary particles (arrows) attaching to the surface of a magnetite nanoparticle. Scale bars, 10 nm. Figure from (Baumgartner et al., 2013b).**

The formation of these primary particles occurred from an unstable initial precursor phase within 2 minutes after the initial addition of iron chloride to the dilute sodium hydroxide solution (Figure 32A). These primary particles showed a surprisingly monodisperse size distribution around 2 nm and aggregated in branched networks. Within 6 minutes, the aggregates locally became denser and spheroidal nanoparticles of 5 – 15 nm formed from them (Figure 32B, arrows). With further reaction time the nanoparticles grew in number and size at the expense of the primary particles (Figure 32C). Lattice fringes and respective FFT reflections with  $d$ -spacings attributable to magnetite were observed superimposed on them (Figure 32D-E). These crystalline nanoparticles possessed a surface roughness pattern indicating that they form through primary particle aggregation rather than atomic accretion (Figure 32D-E). We frequently observed primary particle attachment to the crystals suggesting a secondary nucleation growth mechanism through coalescence (Figure 32E, arrows). The size of attached primary particles and respective surface roughness features on the crystals were reduced to around 1.1 nm (Figure 32E), which indicated their volume decreased in the course of accretion. The primary particles exhibited no crystal lattice fringes before attachment to a crystal surface suggesting that they did not possess translational symmetry before this stage.

These results were to be compared with crystallization studies on calcium carbonate and calcium phosphate (Dey et al., 2011; Pouget et al., 2009), in which the formation of an amorphous bulk phase

was observed through the accretion of nanometre-sized precursors, prior to the appearance of the final crystalline phase. These species were regarded as pre-nucleation clusters whose properties and involvement in nucleation processes are currently under intense debate (Hu et al., 2012). In the case of magnetite, we observed the fusion of nanometre-sized precursors parallel with the formation of crystallinity without intermediate formation of an amorphous bulk phase (Figure 32).

This finding led us to theoretically investigate the general parameters under which such different crystallization pathways were expected to occur. Figure 33A schematically depicts different possible pathways from atoms/molecules to the final crystalline phase: (I) in a classical step rule scenario, atoms/molecules accrete to an amorphous bulk phase. The crystalline phase then appears after the amorphous phase either through a later nucleation event in the solution, upon which time the less stable amorphous phase would dissolve and re-precipitate onto the crystalline nucleus, or through solid state transformation of the amorphous phase. (II) Alternatively, the assembly of the crystalline phase occurs directly from atoms/molecules in solution without an intermediate amorphous phase. Analogously, the accretion of nanometric primary particles or clusters can lead to the formation of (III) the amorphous bulk phase with possible later crystallization or (IV) the crystalline bulk phase. The full theoretical description can be found elsewhere (Baumgartner et al., 2013b). We only present here the general framework and how this model can be applied to better understand magnetite formation.

Figure 33 C depicts an example for a case in which the stability of the primary particles leads to the reversal of the energy barriers of an amorphous (A) and a crystalline (C) nucleus. We started from a scenario in which the thermodynamic barrier for the formation of the amorphous phase was typically lower than that of the crystalline phase ( $\Delta G_A < \Delta G_C$ ), i.e. a step rule scenario (Figure 33A, scenario I) for nucleation from atomic / molecular species. When introducing the observed primary particles we noted that the energy curve of a single primary particle (P) had a well-defined minimum  $\Delta G_P$  corresponding to the observed monodisperse size of this species (to be seen in Figure 33C). The energy content of the primary particle aggregate consumed in the nucleation scaled with its volume (green dashed line in Figure 33C). Figure 33 D shows how the primary particle consumption contributes to the total nucleation work so that the nucleation from primary particles favours a direct crystallization rather than an amorphous phase (free energy for mechanism including primary particles / clusters  $\Delta \tilde{G}_A > \Delta \tilde{G}_C$ , Figure 33A, scenario IV). Metastable primary particles induce the opposite effect, which can lead to a preferential nucleation of the amorphous phase ( $\Delta \tilde{G}_A < \Delta \tilde{G}_C$ ) under conditions that would normally (classical nucleation theory without primary particles / clusters) only allow formation of the crystalline phase ( $\Delta G_A > \Delta G_C$ ).

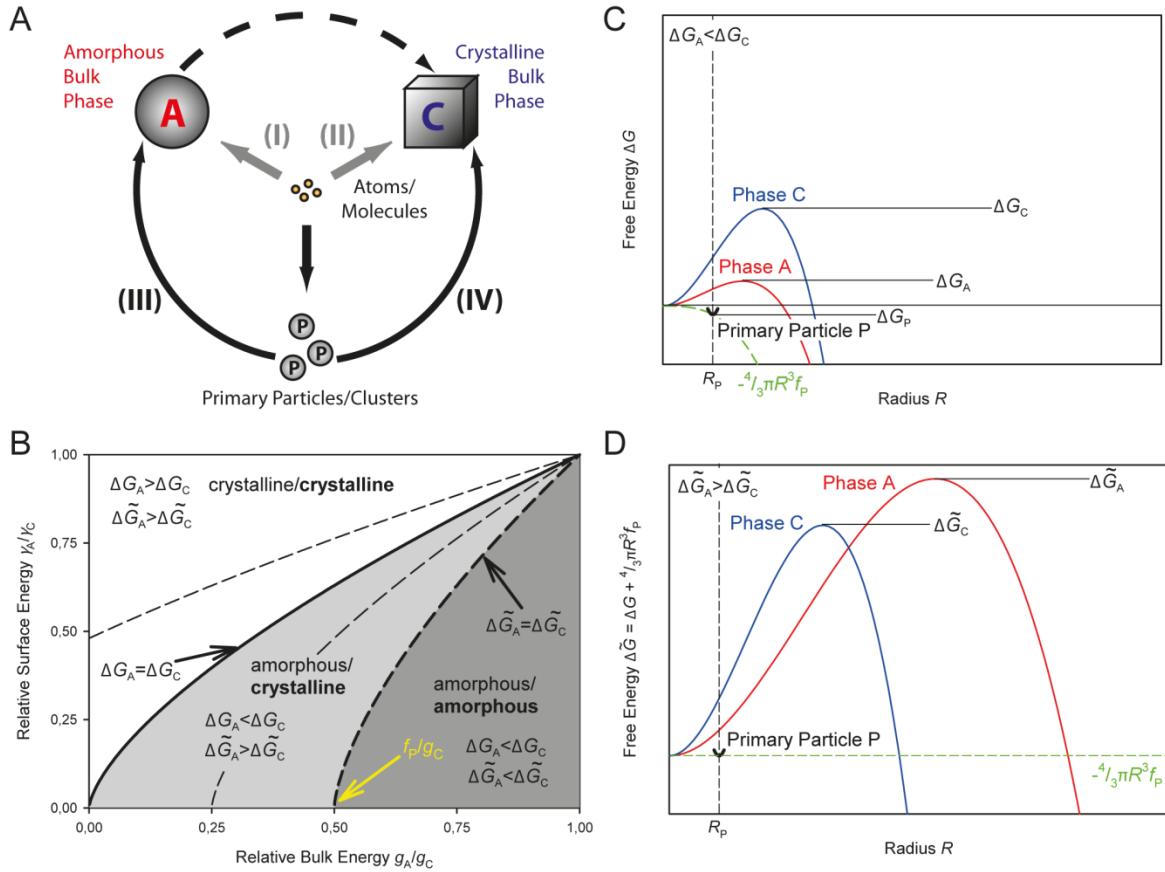


**Figure 33: Model crystallization scenarios from atoms/molecules and primary particles/clusters. (A)** Scheme depicting the different pathways as described in the model. **(B)** Phase diagram showing parameter space for surface ( $\gamma$ ) and bulk ( $g$ ) energy ratios that favour either amorphous (A) or crystalline (C) phase formation. Solid line indicates boundary between phases for atom / molecule accretion scenarios, dashed lines indicate boundaries for primary particle / cluster accretion scenarios based on the stability of the primary particle / cluster ( $f_p$ ) (parameter used:  $f_p / g_c = -0.25$ ,  $f_p / g_c = 0.25$  and  $f_p / g_c = 0.5$ ). The favoured phase by primary particle accretion for a  $f_p / g_c = 0.5$  scenario is given in bold letters, by atomic accretion in regular letters. **(C, D)** Example ( $\gamma_A / \gamma_C = 0.4$ ,  $g_A / g_C = 0.5$ ,  $f_p / g_c = 0.35$ ) in which primary particle stability reverses the energy barrier heights from **(C)** a step rule scenario (amorphous before crystalline) to **(D)** direct crystal formation when forming by primary particle accretion instead of atomic / molecular accretion. Green dashed lines (curve in **(C)**) indicate energy content of the consumed primary particle aggregate ( $-\frac{4}{3}\pi R^3 f_p$ ) which is augmented to the free energy of the bulk phases in **(D)**. Figure from (Baumgartner et al., 2013b).

Based on this generalized framework we investigated the specific conditions in our system of magnetite crystallization with primary particles. In solution chemistry, the driving force for bulk formation is expressed by  $g_v = \frac{k_B T \ln(c/c_s)}{V_m}$ , where  $c$  is solute concentration,  $c_s$  is solubility and  $V_m$  is the atomic / molecular volume that assembles the bulk. We considered in our study the crystalline magnetite to be in competition with a metastable competitor phase for which the poorly ordered iron hydroxide ferrihydrite was the most reasonable candidate. We experimentally added  $0.1 \mu\text{mol min}^{-1}$  Fe to 10 mL total volume water and observed the nucleation of magnetite from primary particles within 6 minutes i.e. for an iron concentration  $c(\text{Fe}) \leq 6 \times 10^{-5}$  M. The solubility of magnetite in this pH and temperature range is reported as  $c_s(\text{Mt}) \approx 5 \times 10^{-8}$  M (Ziemniak et al., 1995). Ferrihydrite has ageing, size and ordering-dependant solubilities in the range of  $c_s(\text{Fh}) \approx 10^{-7} - 10^{-6}$  M<sup>14</sup>. Therefore, we estimated  $g_{\text{Fh}} / g_{\text{Mt}}$  for these two phases to be in the range of 0.58 - 0.90. The surface energy of hydrated magnetite is reported as  $\gamma_{\text{Mt}} = 0.79 \text{ J m}^{-2}$  (Navrotsky et al., 2008). To our

knowledge the surface energy of bulk ferrihydrite has not been determined experimentally, but is estimated to be  $\gamma_{Fh} \approx 0.2 - 0.4 \text{ J m}^{-2}$  (Pinney et al., 2009) resulting in a range for  $\gamma_{Fh} / \gamma_{Mt} = 0.25 - 0.50$ . We plot the respective ranges in Figure 34 (rectangle).

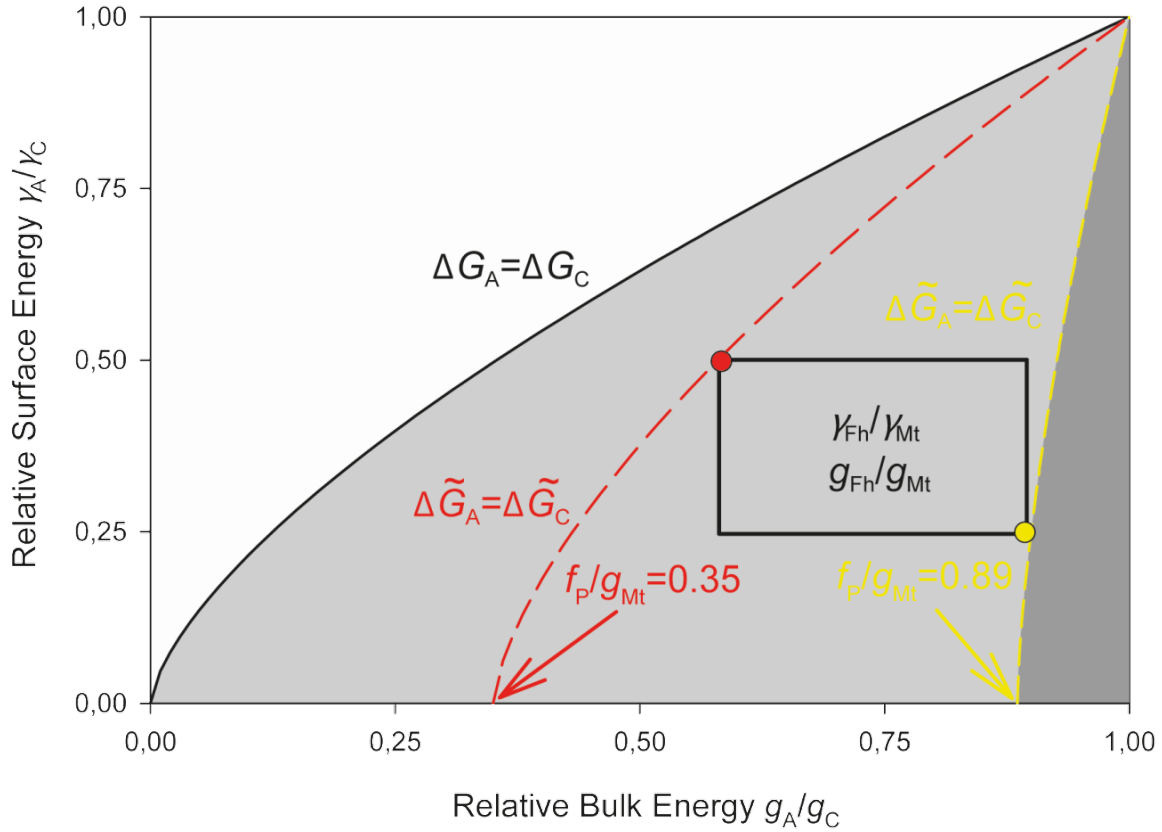


Figure 34: Phase diagram with the estimated surface and bulk energy ratio ranges for ferrihydrite (Fh) / magnetite (Mt) marked as rectangle. The relative primary particle stability  $f_p / g_{Mt}$  must at least surpass 0.35 in order to shift the boundary (solid line) within or beyond this range (red dashed line) to enable magnetite nucleation from primary particles (red point = Fh with lowest stability / highest surface energy in this range). For Fh with the highest stability / lowest surface energy (yellow point) in this range  $f_p / g_{Mt}$  must even be  $> 0.89$  (yellow dashed line). Figure from (Baumgartner et al., 2013b).

The plotted range is situated below the boundary for which the energy barriers for nucleation of amorphous and crystalline phase from atoms are equal (solid line). Therefore, nucleation of a ferrihydrite bulk phase would be favoured over magnetite when formation occurs by accretion of atoms / molecules (Figure 33A, scenario (I)) . Only clusters / primary particles, which are stable with respect to the solution favour the nucleation of magnetite (Figure 33A, scenario IV) as they shift the boundary towards larger  $g_A / g_C$  and smaller  $\gamma_A / \gamma_C$  beyond the plotted range (rectangle). While the broad range of parameters does not allow a precise determination, we estimated the lowest limit for the relative primary particle stability as  $f_p / g_{Mt} > 0.35$  (Figure 34, red dashed line) to achieve magnetite nucleation from this precursor when we assume ferrihydrite' surface energy at the upper and its bulk energy at the lower limit (Figure 34, red dot). For ferrihydrite with small surface energy and comparatively large bulk energy, the primary particles have to even surpass  $f_p / g_{Mt} > 0.89$  (Figure 34, yellow dashed line and dot).

### 3.1.2. MamP enables magnetite formation from ferrous iron alone

Despite early observations of redox control in magnetotactic bacteria (Bell et al., 1987; Frankel and Blakemore, 1984), the management of the iron(II) and iron(III) species required for magnetite formation has remained unsolved. There is indication that some oxidized iron species such as ferrihydrite accumulate before magnetite formation, therefore suggesting the need of a reductive process (Baumgartner et al., 2013c; Fdez-Gubieda et al., 2013b). However, there is also growing evidence that the readily available iron species in the magnetosome is iron(II). Both the presence of numerous and active ferric reductases in magnetotactic bacteria (Zhang et al., 2012) and the predominance of cation diffusion facilitators for iron(II) trafficking (Uebe et al., 2011a) associated with the magnetosome, support this premise. Furthermore, the cellular management of iron(III) is challenging due to its insolubility at physiological pH, likely to be incompatible with magnetite crystal growth.

The search for potential redox proteins within the magnetosome island has led to the identification of four gene products containing at least two tandem *c*-type cytochrome motifs CX<sub>2</sub>CH, recently called magnetochrome domains (Siponen et al.): MamE, MamP, MamT and MamX. Among these magnetochrome-containing proteins, MamE and MamP are conserved in all MTB and, interestingly, deletion mutants of the corresponding genes show defects in the biocrystallisation process (Lohsse et al., 2011; Murat et al., 2010a). However, the multiplicity of this domain leads to difficulties in the phenotypic analyses of a single domain deletion mutant in the *mamE* gene (Quinlan et al., 2011) suggesting that magnetochrome domains are functionally redundant. This magnetochrome domain appears specific to MTB as it is not found in any other species to date, suggesting it may represent a new functional class of cytochrome. In a collaborative effort with the group of David Pignol (CEA, France) and within the doctoral thesis of Marc Widdrat, we provided functional and structural evidence showing that MamP plays a key role in electron transfer reactions and in the management of iron oxidation states inside the magnetosome. The work was centred on crystallographic questions and my group focused on mechanistic aspects of the role of MamP in the formation of magnetite *in vitro*.

We thus observed the role of MamP in a mineralization experiment. Magnetite is indeed typically formed in solution by coprecipitation experiments of iron with the stoichiometric ratio of magnetite (Fe(II) / Fe(III) = 0.5)(Jolivet et al., 2004). We decided to start exclusively with Fe(II) in order to see if any mineral would form in the presence or absence of MamP. In the presence of MamP, we initially observed the formation of ferrihydrite, a Fe(III) oxide, with a progressive evolution of this mineral to magnetite (Figure 6). The control experiment omitting MamP could not allow the detection of any mineral. This mechanism is in line with a process where the Fe(II) is oxidized by the protein to enable the formation of ferrihydrite, a purely ferric iron oxide. Once MamP is fully reduced, the continuous addition of Fe(II) enables the transformation of ferrihydrite to magnetite. Such a mechanism strongly resembles the pathway recently described for the synthetic formation of magnetite from solution I described above .



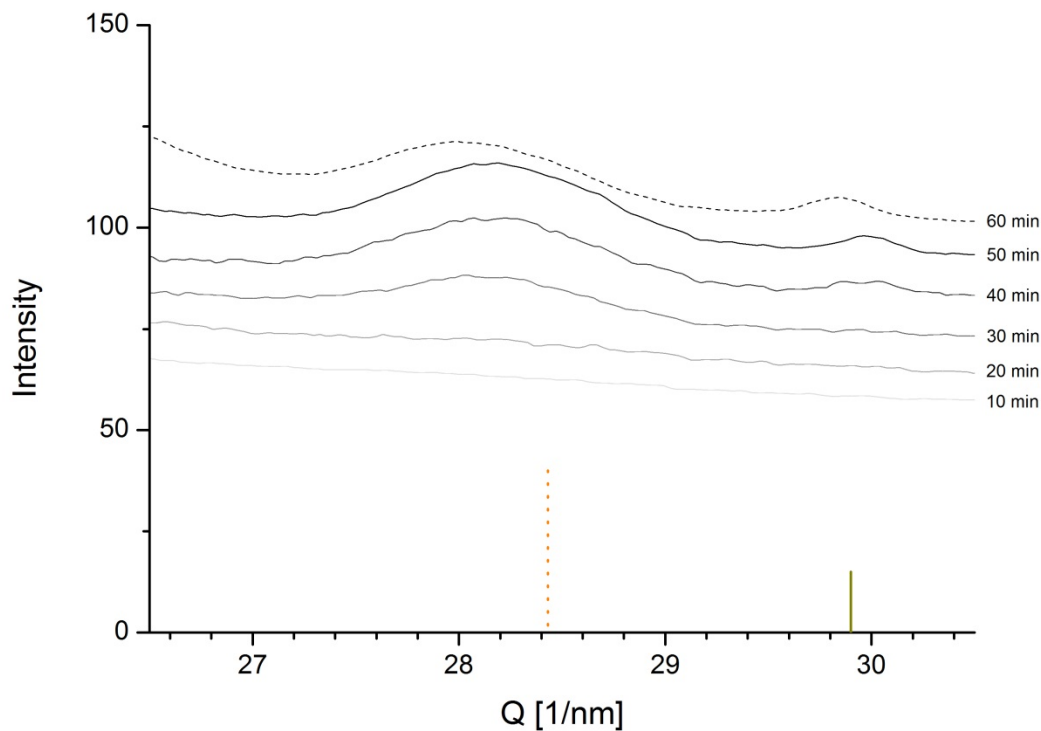


**Figure 35: Time-resolved analysis of the mineralisation synthesis followed by X-ray diffraction. The diffractogram is a closer view in the Q region from 26.5 to 30.5. The peak of 6 lines ferrihydrite ((1 1 2) reference peak in green) increases until 50 minutes whereas the magnetite peak ((4 0 0) reference peak in red) is only visible after 40 minutes and increases then, possibly at the expense of the ferrihydrite precursor.**

Magnetite crystal growth requires a precise Fe(III)/Fe(II) ratio. The MamP properties we revealed underline how the production of the ferrihydrite precursor may be possible thanks to the oxidative properties of the protein. Together with the presence of iron(II), this ferrihydrite would evolve toward magnetite in the magnetosome. This molecular model fits perfectly with sequential events observed for magnetite biomineralisation in MTB (Baumgartner et al., Submitted-b; Fdez-Gubieda et al., 2013a).

### 3.1.3. An alternative strategy to identify biological determinants

Biomineralization is of specific interest to understand the exquisite control of the organisms over materials properties (Dunlop and Fratzl, 2010). Materials scientists in turn try to exploit design principles into the development of biomimetic approaches to synthesize well-defined functional materials under physiological, environmentally-friendly conditions (Nudelman and Sommerdijk, 2012). However, in many biomineralizing systems, it is currently unclear which biological determinant is critical to control a particular materials property, and in the case such molecular player is known, the mechanism by which the biomolecule interacts with the inorganic phase has remained unknown. The identification of such biological molecules was for example performed by

studying proteins or peptides tightly binding to the mineral phase (Arakaki et al., 2003; Kröger and Poulsen, 2008). This technique is clearly limited e.g. to proteins that are resistant to detergents since such chemicals need to be used for the separation of the proteins from the mineral. Recently, biocombinatorial selection of solid-binding peptides has developed into a powerful technique to identify short peptides with specific affinities for dedicated materials (Chen and Rosi, 2010; Schwemmer et al., 2012). In this case, the selection can be performed under near-to-physiological conditions. However, while initially envisaged (Barbas et al., 1993), the combination of biocombinatorial approaches with sequence similarity search within the genome of a sequenced organism has never been achieved experimentally to our knowledge. Using biocombinatorial techniques, Brown and Barbas et al. showed independently that alkaline polypeptides can attach to magnetite (possibly maghemite) crystal surfaces (Barbas et al., 1993; Brown, 1992). However, although the proteomes of several strains of magnetotactic bacteria are known in the meantime (Jogler and Schüler, 2009), we could not identify any similarity between these reported peptides and any proteins from magnetotactic bacteria related to biomineralization.

During this work, accomplished as part of the doctoral work of Jens Baumgartner, we thus performed a biocombinatorial selection based on the M13 phage display to identify 12 amino-acid long peptides that bind to magnetite nanoparticle surfaces (Baumgartner et al., submitted-a). Magnetite nanoparticles were consequently exposed to phages. Phages showing binding affinity to the crystal attached to the surface of the nanoparticles, whereas non-binding viruses stayed in solution. After removal of the non-binders, the bound phages were eluted and re-amplified for further iterative rounds of selection. Finally, a pool of phages with potentially high binding affinity was obtained. DNA sequencing of individual phage clones revealed the displayed peptide sequence.

Table 3 shows the peptide sequences from two independent series of experiments and the best consensus protein for each peptide from the *M. gryphiswaldense* proteome. Sequence similarities to the magnetosome protein MamJ and the supposed magnetotaxis protein MtxA were observed for peptides #19 and #26, respectively. The determined consensus sequence of peptide #19 with MamJ is PVAXLVNR, where X is lysine in the phage sequence and aspartic acid in the protein. The consensus sequence is found twice in MamJ due to its repetitive structure. Sequence alignment of peptide #26 with MtxA gave VPSLTPX<sub>1</sub>AX<sub>2</sub>S as consensus, where X<sub>1</sub> is serine and glycine, and X<sub>2</sub> is histidine and glutamine in peptide and protein, respectively.

**Table 3: Selected sequences from phage display on magnetite particles. Recovered peptide sequences were subjected to a BLAST search on the *M. gryphiswaldense* genome to determine similarities with magnetotactic bacteria proteins. Sequences marked (\*) were obtained twice.**

Phage	Peptide Sequence	Protein with best sequence alignment (BLAST)
1	AHRHPISFLSTL	Fe-S oxidoreductase (CAM76455.1)
2	IPLPPSRPFFK	DNA polymerase III epsilon chain-like protein (CAM77883.1)
3	TLNKPNRALHFN	Enoyl-CoA hydratase/isomerase (CAM74578.1)
4	QAYRSSAFLPPM	adenylate/guanylate cyclase (CAM73978.1)
5	YPAPQPLVTKTS	ABC-type multidrug transport system, ATPase component (CAM76255.1)
6	SPLPSHKSQHTW	Substrate-binding protein of ABC transporter (CAM77924.1)
7	EHLQFSTHGPLR	Hemolysin-type calcium-binding region (CAM77170.1)
8	YHEADPQAYQRT	hypothetical protein MGR_1147 (CAM76617.1)
9	NLTSLTQGSAML	ABC transporter, transmembrane region:ABC transporter (CAM76860.1)
10	NMTKHPLAYTEP	Tral protein (CAM77712.1)
11	TTHPSTVQTPNW	two-component response regulator (CAM78131.1)
12	NPFNQHLHAQHP	hypothetical immunogenic protein (CAM74300.1)
<b>13</b>	<b>SGHQLLLKMPN</b>	<b>extracellular solute-binding protein, family 3 (CAM74369.1)</b>
14	TSASTRPELHYP	conserved hypothetical protein (CAM77493.1)
15	NDNTYANHGIKH	cell cycle protein (CAM74766.1)
16*	GTPPMSPLVSRV	Lysine exporter protein (LYSE/YGGA) (CAM74771.1)
17*	SILSTMSPHGAT	30S ribosomal protein S8 (CAM77762.1)
18	GTPRSHYPAPQV	Hdr-like menaquinol oxidoreductase subunit (CAM75801.1)
<b>19</b>	<b>QFSLPVAKLVNR</b>	<b>magnetosome protein MamJ (CAJ30117.1, CAE12033.1)</b>
20	YSIEQEHPSPFP	conserved hypothetical protein (CAM76297.1)
21	ATTHRQVQNAFR	hypothetical protein (CAJ30057.1)
22	KPLDIHGNNSYW	SmpB protein (CAM76784.1)
23	SPTLSNDEHLRM	Dihydrodipicolinate synthetase (CAM76783.1)
24	ITHPTGFLTSRP	conserved hypothetical protein (CAM78153.1)
25	DLKLETALSNT	Ribonuclease HII (CAM76235.1)
<b>26</b>	<b>VPSLTPSAQSRP</b>	<b>magnetotaxis protein MtxA (CAM74323.1)</b>
27	YSPDPRPWSSRY	conserved hypothetical protein, membrane (CAM74215.1)

The magnetotactic bacterial proteins MamJ and MtxA were recombinantly produced in *E.coli*. MtxA could not be expressed soluble due to a leading N-terminal signal peptide associated with membrane translocation. Therefore, we constructed the soluble protein MtxA $_{\Delta 1-24}$  without the signal peptide for mineralization studies.

Co-precipitation of ferrous and ferric iron (at  $\text{Fe}^{3+} / \text{Fe}^{2+} = 2 / 1$ ) under alkaline conditions at  $\text{pH} \geq 9$  yields crystalline magnetite with grain sizes dependent on the alkalinity. We studied the influence of the selected proteins (MamJ and MtxA $_{\Delta 1-24}$ ) as well as the two peptide polymers poly-L-arginine (polyR) and poly-L-glutamic acid (polyE). polyR serves as a proxy for a potential polycationic biomolecular structure as inferred from the earlier literature reports by Barbas et al. and Brown et al. (Barbas et al., 1993; Brown, 1992). polyE resembles a polyanionic domain found in MamJ (Scheffel et al., 2006b; Scheffel and Schüler, 2007). Apart from structural differences, the proteins / polymers differ primarily in the availability of differently charged groups that can interact with different iron or iron (oxyhydr)oxide species. Acid residues provide binding moieties for cationic  $\text{Fe}^{\text{II/III}}$ , whereas the cationic guanidinium group is able to interact electrostatically with (in alkaline solution) negatively charged iron (oxyhydr)oxide crystal surfaces.

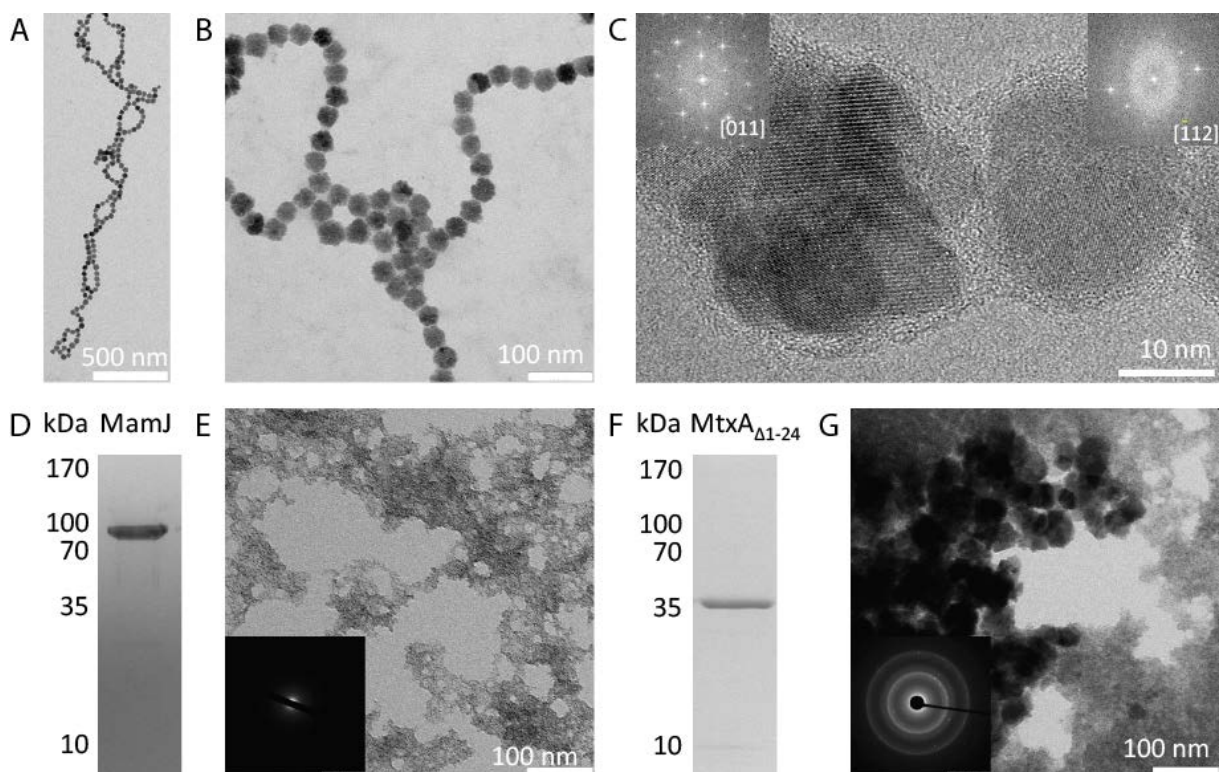


**Figure 36: Precipitation products in the presence of peptide polymer and protein additives. (A-C) Magnetite particles formed in the presence of poly-L-arginine, insets in (C): FFTs of particles indeed indexed as being magnetite. (D) SDS-PAGE of MamJ, (E) precipitation product in the presence of MamJ, inset: electron diffraction does not reveal crystallinity, (F) SDS-PAGE of MtxA $_{\Delta 1-24}$ , (G) precipitation product in the presence of MtxA $_{\Delta 1-24}$ , inset: electron diffraction showing rings, whose distance is typical of magnetite.**

The presence of the additives has a strong effect on phase, crystallinity, particle size, morphology and aggregation of the precipitates in agreement with the interactions with soluble or solid iron species

that either occur prior or after the nucleation of the magnetite phase (Figure 36-37). PolyR affects size, morphology and aggregation behavior of the formed magnetite nanoparticles: in its presence we obtained monodisperse single stable domain-sized nanoparticles of  $35 \pm 5$  nm (Figure 39) that assemble to chain structures in solution (up to several micrometers) (Figure 36A). Despite their irregular morphology, particles are mostly single-crystalline (Figure 36C). MamJ and polyE strongly affect the phase of the formed precipitates by inhibition of magnetite nucleation with increasing additive concentration: in both cases we obtained either amorphous gels or other crystalline phases than magnetite. Only at low additive concentrations ( $0.01 \text{ mg mL}^{-1}$ ) magnetite could be obtained (Figure 37). At pH = 11, in the presence of  $0.01 \text{ mg mL}^{-1}$  MamJ, diffraction patterns are consistent with an extremely small nano-sized magnetite (Figure 4; line features are extremely broadened magnetite peaks, intensity increase towards low q). At pH = 9, we obtained unidentifiable mixtures (Figure 37; peaks at  $q = 19.13, 26.66, 32.57, 34.03, 41.16, 45.42 \text{ nm}^{-1}$ ;  $d = 0.33, 0.24, 0.19, 0.18, 0.15, 0.14 \text{ nm}$ ). With  $0.1 \text{ mg mL}^{-1}$  MamJ we obtained a poorly ordered pattern for pH = 9 (Figure 3; possibly ferrihydrite), and at pH = 11 (Figure 38) a pattern with two distinct peaks at  $q = 15.51 \text{ nm}^{-1}$  ( $d = 0.41 \text{ nm}$ ) and  $q = 25.25 \text{ nm}^{-1}$  ( $d = 0.25 \text{ nm}$ ), which are consistent with goethite ( $\alpha\text{-FeOOH}$ ). Accordingly, in the presence of  $0.1 \text{ mg mL}^{-1}$  polyE we obtained no crystalline material within 1 h: at pH = 9 we obtained an orange amorphous gel-like precipitate by centrifugation from a clear solution, whereas at pH = 11 no pellet could be formed even by centrifugation. At low concentration ( $0.01 \text{ mg mL}^{-1}$ ) polyE has no strong impact on the formed phase (Figure 37). Finally, MtxA $_{\Delta 1-24}$  has only minor influence on the phase of the formed precipitates: in the presence of  $0.1 \text{ mg mL}^{-1}$  MtxA $_{\Delta 1-24}$  at pH = 9 we obtained only amorphous / poorly crystalline material with similar orange gel-like properties, whereas under all other conditions we obtained mixtures of magnetite and amorphous gels (Figure 36G).

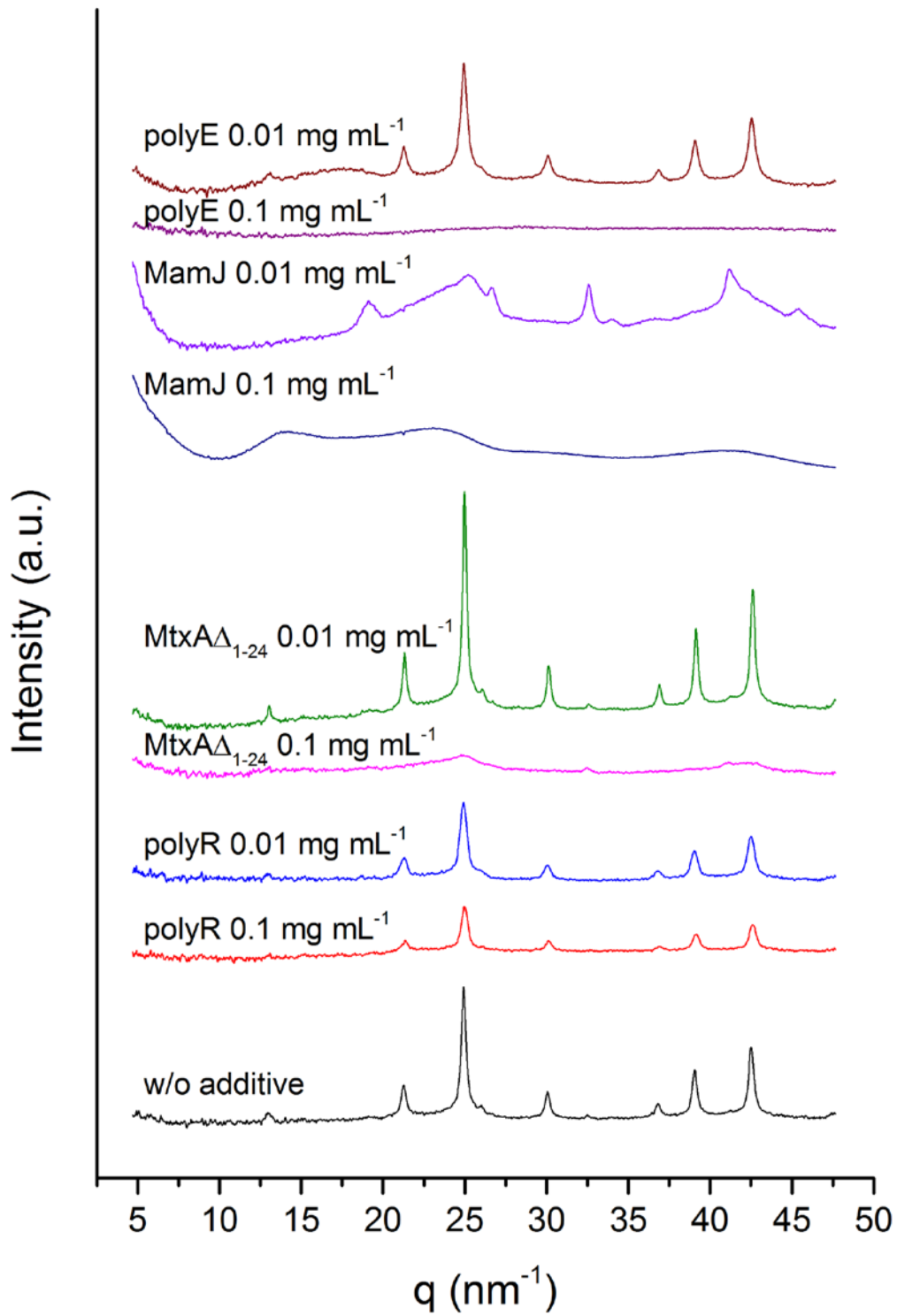


Figure 37: X-ray diffraction patterns of precipitates formed at pH = 9 without additive and in the presence of protein and peptide polymers.

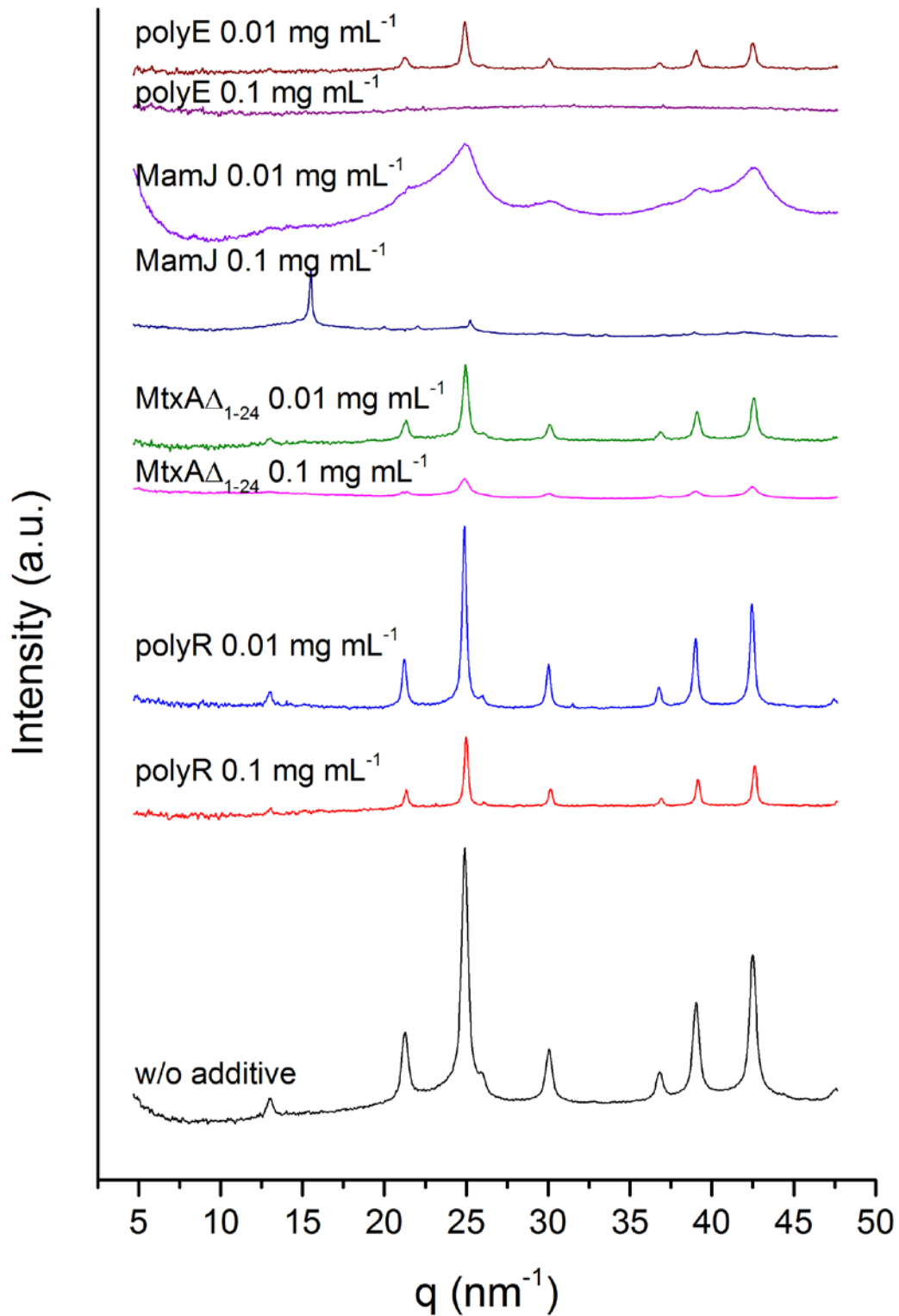


Figure 38: X-ray diffraction patterns of precipitates obtained at pH = 11 from ferrous and ferric iron chloride solution mixtures without and in the presence of protein or polypeptide additives.



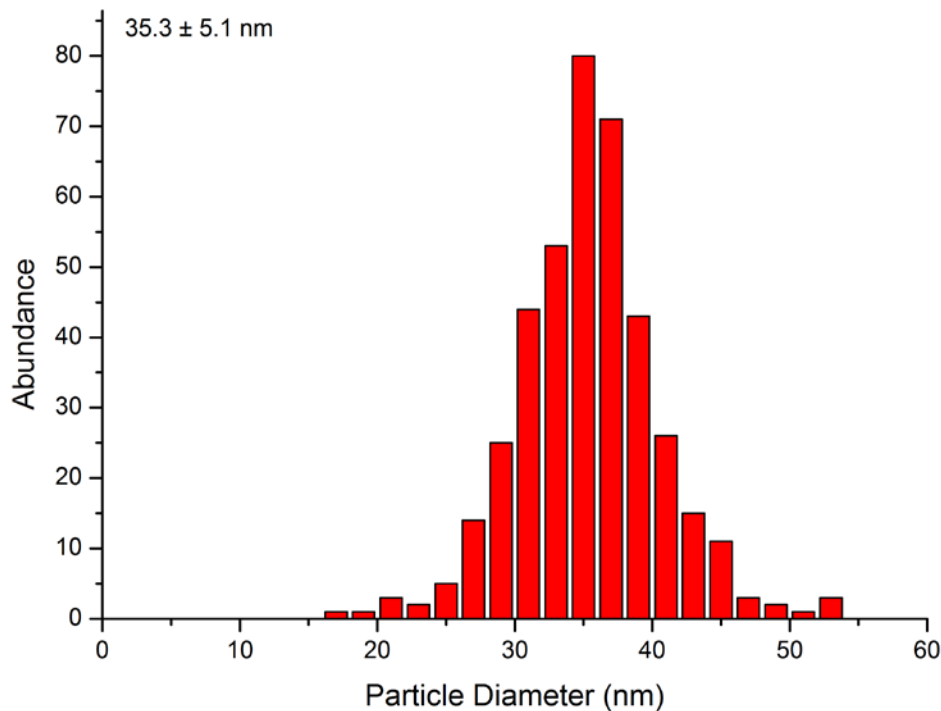


Figure 39: Particle size distribution of magnetite particles formed in the presence of polyR.

MamJ, investigated here, is involved in the magnetosome chain assembly and has been suggested to serve as an anchor to the MamK filament in the cell (Carillo et al., 2013; Scheffel et al., 2006b). The anchoring function is provided exclusively by the N- and C-terminal domains without involvement of a repetitive central sequence stretch rich in glutamic acid (Scheffel and Schüler, 2007). The role of this polyanionic domain has remained unclear, but was initially suspected to take part in biomineralization through binding and accumulation of iron. The found consensus sequence PVA-LVNR can be located twice within this repetitive stretch of unknown function (Table S3; MamJ<sub>83-90</sub> and MamJ<sub>171-178</sub>). However, the inhibitory function with respect to magnetite mineralization *in vitro* appears inconsistent with the formation of the iron oxide both in and without the presence of the protein *in vivo* (Scheffel et al., 2006b; Scheffel and Schüler, 2007); unless a yet unknown regulatory function of mineral formation is required for magnetosome chain formation in the bacteria.

MtxA was identified in or attached to the magnetosome membrane (Tanaka et al., 2006). It has been suggested to play a role in magnetotaxis because of its gene location in an operon encoding signal transduction genes (Richter et al., 2007). However, no experimental evidence has shown the implication of the protein in such a mechanism so far. Our *in vitro* assays suggest that despite the possibility that the protein can bind to magnetite, it will likely have no effect on crystallization of the mineral *in vivo*.

The strong effects of the synthetic peptide polymer polyE on magnetite nucleation inhibition suggest that if an inhibitor exists in the bacteria, it will likely act by iron binding through acidic moieties. The nucleation and colloidal stabilization effects of polyR, leading to particle chain formation *in vitro*, are

consistent with a colloidal stabilization by magnetosome compartmentalization in the bacteria *in vivo*.

Although biocombinatorial approaches and *in vitro* mineralization assays alone cannot infer the role of proteins (or other biomolecules) in biomineralization *in vivo*, they can point towards possible molecular characteristics required by the involved biochemical machinery. Our experiments suggest that in the case of magnetite formation discussed here, proteins, larger complexes or membrane components which are promoting the nucleation *in vivo*, are likely to expose positively charged residues to a negatively charged crystal surface. Components with acidic (negatively charged) functionality are likely inhibitors by stabilization of an amorphous structure through coordination of iron.

### 3.2. Magnetite assembly: actuated nanodevices

Nanorobotics is an emerging interdisciplinary field of research and technology raising new challenges and promising advancements in medicine, biology and industrial manufacturing (Sitti, 2009; Zhang et al., 2011). Nanorobots are devices with overall dimensions at or below the micrometer that are made of nanoscaled building blocks with individual dimensions ranging between 1 and 100 nm. Nanorobots would be able to perform at least one of the following actions: actuation, sensing, signaling, information processing, intelligence, swarm behavior at the nanoscale.

Nanorobots can be used for the fabrication, the manipulation, control and assembly of individual building blocks, as actuator or sensor in biological environments or for operating in human blood vessels or microvasculatures as a medical device (Mavroidis and Ferreira, 2009). In reality, most of the nanorobots are micro-sized, and the only nano-sized robots are protein-based such as systems based on biological motor proteins, cargos and microtubules (Goel and Vogel, 2008). Propelling non-tethered nanorobots, having them swimming within a liquid is a current challenge, as they have to be powered and steered so that their efficiency overcomes Brownian motion.

Flagellated bacteria, on the other hand, effectively swim by rotating thin helical filaments, each driven at its base by a reversible rotary motor, powered by an ion flux (Berg, 2003). A motor is about 45 nm in diameter and is assembled from about 20 different parts. Bacteria themselves were used as microoxen to move microscale loads (Weibel et al., 2005) or to power a microrotary motor (Hiratsuka et al., 2006). However, if bacteria permit an efficient conversion from chemical energy into mechanical work, they can only be used in specific environments, which dramatically reduce their possible use.

The bacterial “motor” develops maximum torque at stall but can spin several hundred Hz (Berg, 2003). It enables the about 3  $\mu\text{m}$  long cells to swim rapidly at possibly more than  $100 \mu\text{m} \times \text{s}^{-1}$  (that is a remarkable 30 body-sizes per second) over several dm (4 to 5 order of magnitude more than the body size). As a comparison, the best marathon runners cannot run faster than about 3 body-sizes per second, i.e. about one order of magnitude less than an average bacterium. Magnetotactic bacteria as explained before in this thesis combine the exploitation of one or several flagella for effective swimming with the use of an internal magnetic dipole for the efficient orientation within

magnetic fields (Frankel et al., 2007). It is therefore logical to develop tomorrow's swimming nanorobots being inspired by such bacterial system.

### **3.2.1. Microdevices based on whole magnetotactic bacteria**

Complex, often hierarchially-structure, biogenic minerals have evolved from naturally optimized processes (Fratzl and Weinkamer, 2007; Mann, 2001). Biopolymeric templates, such as proteins, generally control both mineralization and properties of the inorganic components, because biomineralization processes are genetically driven (Baeuerlein, 2007; Mann, 2001). However, biominerals cannot directly lead to the generation of materials with specific technical properties, therefore further treatment is required to form hybrid functional materials that can be used for a variety of applications (Sanchez et al., 2011).

Magnetotactic bacteria are one example of a biomineralizing organism that form hybrid materials with properties that could so far not be matched by synthetic approaches. Above, the hierarchical structuring of the magnetosome chain starts with the formation of structurally pure magnetite nanoparticles, and follows with the organization of stable single domain-sized magnetic particles in single or multiple chains or clusters; these give rise to enhanced magnetic properties (Fischer et al., 2011)(Chapter 0). The organisms are therefore a paradigm of hierarchical magnetic chains. However, while several bio- and nanotechnological applications have been envisaged for the isolated magnetosomes (Lang et al., 2007; Matsunaga et al., 2007), less have been proposed for the whole cells (Martel et al., 2009), partly because of possible undesirable immunogenic response.

We have thus decided to use magnetotactic bacteria as a template to synthesize a composite material made up of a hierarchically-structured magnetic chain in a hollow silica particle. The bacteria were first grown, then embedded in silica following the Stöber process (Stöber et al., 1968), and the material was then calcined to remove any organic content. The synthetic route formed silica in the shape of long hollow tubes on the order of several microns, which completely covered the bacteria (Figure 40a). This is consistent with the typical dimensions of these bacteria. The average thickness of the silica coating is approximately 100 nm (Figure 40b). The morphology of the chain was not affected as seen from the shape of the silica shell (Figure 40a), and a STEM image of the chain within the shell (Figure 40b).

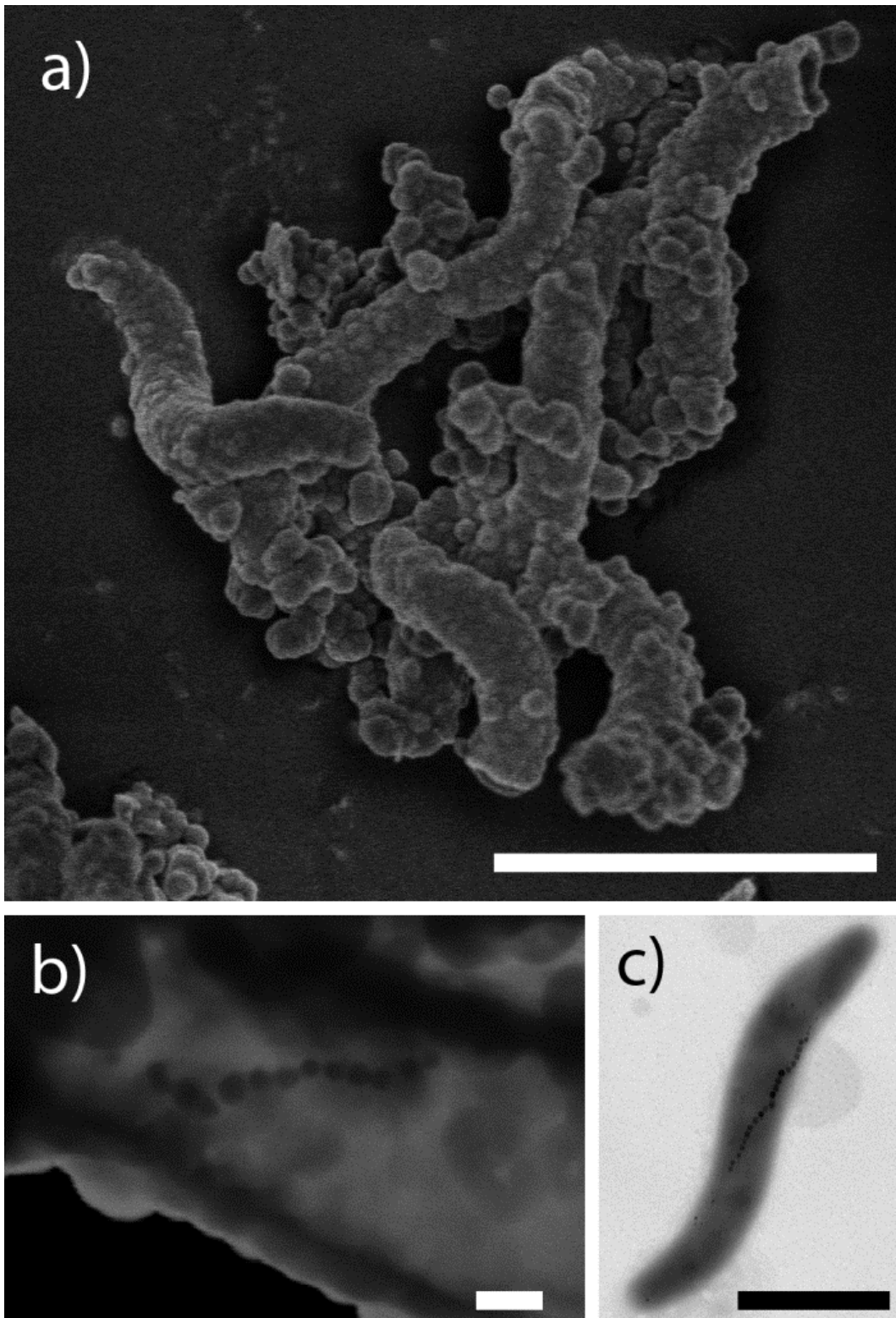


Figure 40: summary of representative electron microscope images (scale bars 1 $\mu$ m in a and c and 100 nm in b). (a) HRSEM image of the materials, (b) STEM image of the materials, (c) TEM image of a magnetotactic bacteria used as template.

Further confirmation for the preservation of chain structure within the silica coating was seen by placing the synthesized material in an external magnetic field. Single isolated magnetosomes should exhibit no preferred orientation of their crystallographic axes within the silica shell, and therefore

should show no preferential alignment. Chains of magnetite, however will display a strong anisotropy that causes them to align with a field. When the material was redispersed in an aqueous solution and placed in a 50 mT field, the long axes of the chain followed the orientation of the external field (Figure 41).

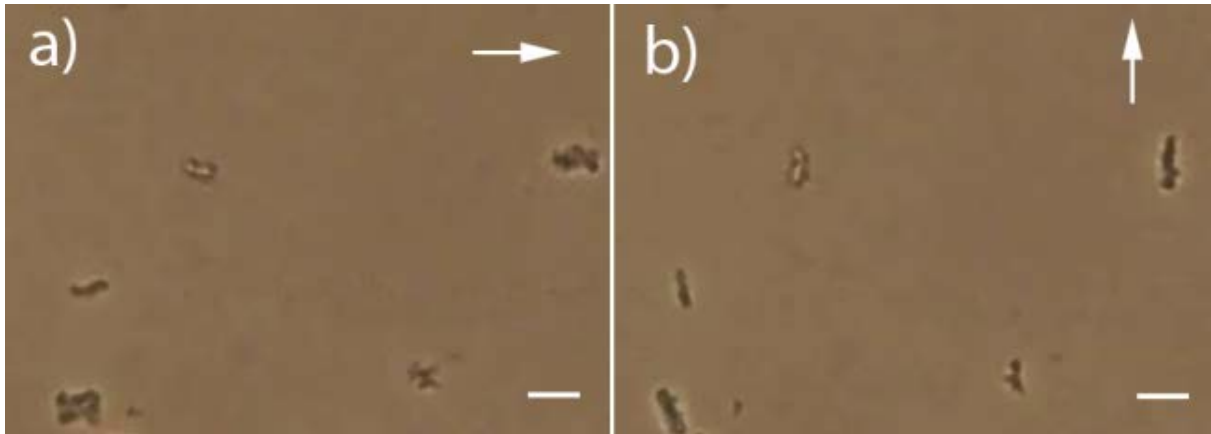


Figure 41: optical microscopy images of the resuspended materials in external fields (direction indicated by the white arrows, scale bars: 5  $\mu\text{m}$ ).

The present work demonstrated the one step synthesis of hybrid hollow silica / magnetic microparticles from a magnetotactic bacteria precursor. The synthesis could be performed in a single stage and did not require the use of an external magnetic field for assembly. In addition, the magnetic dipole consists of a chain of stable single-domain particles with a high remnant magnetization that is more responsive to external fields than superparamagnetic particles. Therefore, these materials are actuators that represented the first step towards more active and responsive materials developed in the following chapters.

### 3.2.2. Bottom-up approaches based on the assembly of magnetic nanoparticles

Micro- and nanostructures typically possess shape-dependent characteristics. The typical approach to producing such structures in large quantities by solution synthesis is based on selection for shape. Reaction conditions and purification schemes are chosen to favor a specific shape. A potentially more economical approach is to select instead for a specific function. This second option is particularly advantageous when the optimal shape is not known, or when a multitude of shapes can fulfill the desired function. We demonstrated this strategy in the doctoral work of Peter Vach by selecting magnetically steerable nanopropellers from a set of carbon coated aggregates of magnetic nanoparticles using weak homogenous rotating magnetic fields (Vach et al., 2013).

Magnetic nanostructures are promising building blocks for the creation of such swimmers since they can be manipulated by external magnetic fields (Fischer and Ghosh, 2011; Zhang et al., 2011). Unlike electric fields, magnetic fields are not screened by dissolved ions and can selectively exert large

forces on magnetic materials. Gradient fields can in principle be used to directly actuate magnetic micro- and nanostructures (Zeeshan et al., 2013), but sufficiently strong gradient fields are difficult to produce and the resulting movement is not a real swimming since the structures are actuated but not self-propelled. The coupling of hydrodynamic forces with magnetic forces has allowed the creation of swimmers and propellers, which can autonomously move in a controlled manner in weak homogenous magnetic fields. Typical examples are elastic structures driven by time-reversible magnetic fields (Benkoski et al., 2011; Dreyfus et al., 2005; Pak et al., 2011) and rigid structures (propellers) driven by non-time-reversible magnetic fields (Ghosh and Fischer, 2009; Zhang et al., 2009b). In fact, as described by the scallop theorem (Purcell, 1977), translatory movement would be impossible if both the actuating magnetic field was time-reversible and the structure rigid.

Previously published nanopropellers employed sophisticated nanofabrication methods (Ghosh and Fischer, 2009; Perez-Gonzalez et al., 2012; Zhang et al., 2009b), which allowed precise control of the propeller nanostructure, but required expensive clean room equipment for their production. Different nanopropellers can be compared using a dimensionless speed, defined as  $U = v/(Lf)$ , where  $v$  is the dimensional speed,  $L$  the largest dimension of the nanopropeller and  $f$  the frequency of the actuating magnetic field (Li et al., 2009). A particularly high dimensionless speed was achieved with the helical nanopropeller by Ghosh and Fischer (Ghosh and Fischer, 2009), with  $U$  up to 130 ( $v = 40 \mu\text{m/s}$ ,  $L = 2 \mu\text{m}$ ,  $f = 150 \text{ Hz}$ ). The propeller of Zhang et al. (Zhang et al., 2009a) propelled with  $U$  up to 21 ( $v = 40 \mu\text{m/s}$ ,  $L = 2 \mu\text{m}$ ,  $f = 150 \text{ Hz}$ ).

The synthesis method is based on hydrothermal carbonization (HTC), which has been used previously to cover iron oxide nanostructures (Winklhofer and Zimanyi, 2006; Ye et al., 2010). Briefly, we suspended iron oxide nanoparticles in glucose solution and heated it to  $180 \text{ }^\circ\text{C}$  for 24 hours. A weak homogenous rotating magnetic field was then used to select nanopropellers from the reaction product by letting them propel to the top of a glass vial (Vach et al., 2013). We observed the movement of the nanopropellers in a custom built optical microscope. The direction of the nanopropeller movement could be controlled, since they always moved parallel to the vector of rotation of the actuating rotating magnetic field. The speed of the nanopropeller movement could also be controlled, by varying the frequency of the actuating field. We investigated the nanostructure of exemplary nanopropellers. The speed and morphology of the propellers is shown below (Figure 42).

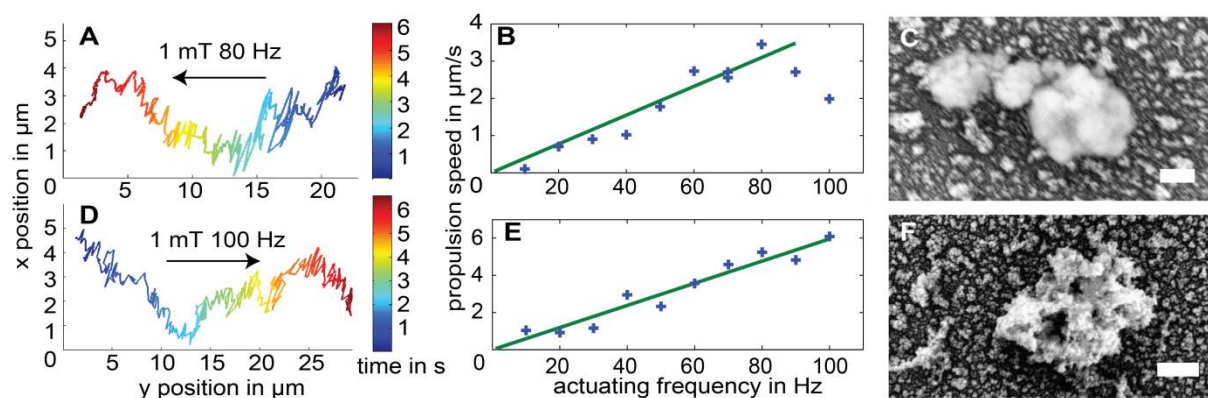


**Figure 42: Study of two exemplary nanopropellers. Traces of these measurements are displayed in A and D. The black arrows indicate the direction of the vector of rotation of the actuating magnetic field. Diffusive and translatory**

movements are superimposed. The propulsion speed depends linearly on the frequency of the actuating magnetic field up to a critical frequency (B and E). (C and F) Backscattered electron microscopy images of the two nanopropellers. Scale bars are 200 nm. The dimensionless speeds are estimated from these measurements as  $U = 33$  for the upper nanopropeller and  $U = 72$  for the lower nanopropeller.

We then developed a simple model describing the movement of a nanopropeller. The full theoretical framework is presented in the manuscript by Vach et al. (Vach et al., 2013). Based on our theoretical work, we expect smaller nanopropellers to have a higher critical frequency. This expectation was confirmed by optical size estimates of propellers that could propel to the upper inner surface of a capillary in rotating magnetic fields of different field strengths (Figure 43A). Indeed, fewer larger structures can propel upwards, against gravity, in a weaker magnetic field. To study the smallest propellers, we acquired backscattered electron micrographs to image structures selected with a reduced magnetic field of 0.5 mT rotating at 100 Hz. We found structures smaller than 1  $\mu\text{m}$  (Figure 43 B), showing that nanopropellers can be selected from our synthesis products. The smallest propellers we observed were around 300 nm in size. For comparison, the smallest propellers previously reported measured about 1.5  $\mu\text{m}$  along their longest dimension (Ghosh and Fischer, 2009).

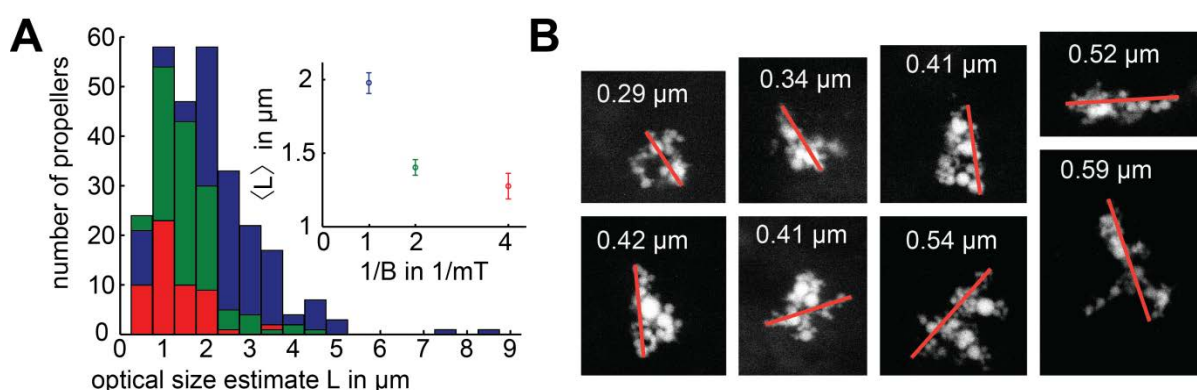


**Figure 43:** (A) Size distribution of propellers selected in different rotating magnetic fields (red 0.25 mT, green 0.5 mT, blue 1 mT, frequency always 100 Hz). The histograms display the total number of structures of a particular size that were found to propel against gravity in the applied rotating magnetic field. As expected from our theory, fewer larger structures can propel upwards in a weaker magnetic field. This is also apparent in the inset, where the mean size is plotted against the inverse magnetic field strength (error bars are standard error). (B) To study the smallest propellers, we acquired backscattered electron images of structures that were selected in a 0.5 mT, 100 Hz magnetic field. Based on the distance travelled and the duration of our selection experiment, we can estimate the dimensionless speed value of a nanopropeller of 1  $\mu\text{m}$  size to be above 10, for propulsion against gravity. The eight smallest structures observed are presented.

Our functionalization technique is versatile and can enable a wide range of applications such as controlled assembly in solution (Dunlop and Fratzi, 2010) or triggered release (Nudelman and Sommerdijk, 2012). Other potential applications include fluid mixing at low Reynolds numbers, and local rheological probes (Fischer and Ghosh, 2011). Production of our nanopropellers is simple, cheap and scalable and thus of particular interest to large scale applications, such as micropatterning of large surfaces (Manesh et al., 2013) and environmental remediation (Alphandéry et al., 2012).

The general idea of selecting from randomness has been previously demonstrated for libraries of chemical compounds (combinatorial chemistry) or viral proteins (phage display), thereby showing great potential. We demonstrated here that this principle can also be used for the selection of nanopropellers with specific properties. Such an approach might also be successfully applied to other combinations of external stimuli and random features.







## 4. Summary and Outlook

In this thesis, the formation of nanometer-sized magnets, their assembly in chain together with their possible use as navigation devices has been studied respectively within a biological and a chemical environment. Besides the simple and visible results, the common thread is clearly the use of high resolution physico-chemical techniques – *in vivo* and *in situ* whenever possible - to understand nanometer-scale processes that create highly functional materials. Obviously, we are not satisfied by only characterizing a material as such but rather aim at understanding what are the principles leading to such properties in order to develop biomimetic strategies towards e.g. greener synthetic processes and efficient functional materials. Having that in mind, the main achievements of this work are:

- First, if magnetotactic bacteria are very effective in controlling the size and morphology of their magnetosomes, their secret – at least with a chemist’s view – might not be connected with the genes and proteins they use but rather with the fact that they are not very effective in transporting the iron to its final destination. Indeed, the bacteria take up the iron at a very high biological pace, but this is of course nothing when compared to a typical coprecipitation experiment where “tons” of iron are mixed simultaneously. Therefore, we simply reduced the addition rate of iron in our synthetic routes, which thereby possibly decreased the supersaturation, and in turn made particle growth energetically possible and particle nucleation less favorable.
- The next bacterial secret is the organization of the magnetosome in a chain. Indeed, a line of magnets should have the tendency to bend and form a circle. We showed that a structural reinforcement technique exists within the bacteria to keep magnetosomes aligned. We even demonstrated that the biological macromolecules are the main factor directing the assembly. Thus, an external support in the form of a template or cross-linked molecules is needed to keep the nanomagnets in a 1D structure. Our first try including the use of burned sugar in a magnetic field could produce magnetically responsive nanodevices with a decent speed when compared to microrobots produced with high costs e.g. but lithography even if the chain pattern was not reproduced with high fidelity.

If these two examples simply depict two main achievements obtained over the years of the work reported in this thesis, they also make clear that there is still a long way to go to fully understand how these simple organisms function and to extract the best of their secrets for further biomimetic

approaches. Indeed, we have not discovered all the enigmas and for example, the following lines of research should be pursued in the future:

- We have started to synthesize magnetite particles larger than about 20 nm, a size never achieved before with such a simple assay. However, we are far away from controlling the size as nicely as the cells are doing it. This is possibly because we are not using compartments as the bacteria do, but also because we might need to use additives as the microorganisms do when using proteins.
- Another feature that is characteristic of the magnetotactic bacteria, at least of some strains, is that they are capable of forming anisotropic particles, which is unexpected for the magnetite crystallizing in the  $Fd3m$  space group. Most of these types of cells first form isotropic crystals that turn anisotropic in shape when they mature. We are currently following different approaches to decipher the possible biological determinants involved in this process of morphological control and understand their chemical properties and roles.
- The use of these magnetic nanoparticles in bio- and nanotechnological applications requires their colloidal stabilization in solution, which is notoriously difficult, specifically for larger particles with permanent magnetic dipole moments. Here also it is possible to learn from the bacteria and their magnetosome membranes since isolated magnetosomes with their membrane are stable as such in solution. Different strategies can be followed here too including the formation of a shell possibly in a 1-step strategy to prevent any agglomeration.
- The formation of magnetic chain in a controlled way will be of further interest not only for the synthesis of more effective swimming devices but also for the formation of large 2D and possibly 3D superstructures. We are using biological and chemical templates to obtain such structures and XRD is a powerful technique to study whether we can properly organize them or not.





## 5. References

- Abracado, L.G. et al., 2010. Magnetosome chain superstructure in uncultured magnetotactic bacteria. *Phys. Biol.*, 7(4): 046016.
- Alexandre, G., Bally, R., Taylor, B.L., Zhulin, I.B., 1999. Loss of cytochrome c oxidase activity and acquisition of resistance to quinone analogs in a laccase-positive variant of *Azospirillum lipoferum*. *Journal of Bacteriology*, 181(21): 6730-6738.
- Alphandéry, E. et al., 2009. Assemblies of Aligned Magnetotactic Bacteria and Extracted Magnetosomes: What Is the Main Factor Responsible for the Magnetic Anisotropy? *ACS Nano*, 3(6): 1539-1547.
- Alphandéry, E., Guyot, F., Chebbi, I., 2012. Preparation of chains of magnetosomes, isolated from *Magnetospirillum magneticum* strain AMB-1 magnetotactic bacteria, yielding efficient treatment of tumors using magnetic hyperthermia. *Int. J. Pharmaceutics*, 434(1–2): 444-452.
- Arakaki, A., Webbs, J., Matsunaga, T., 2003. A Novel Protein Tightly Bound to Bacterial Magnetite particles in *Magnetospirillum magnetotacticum* Strain AMB-1. *J. Biol. Chem.*, 278(10): 8745-8750.
- Baeuerlein, E., 2007. The Biology of Biominerals Structure Formation. *Handbook of Biomineralization*, 1. Wiley-VCH, Weinheim.
- Baeuerlein, E., Behrens, P., 2007. Biomimetic and Bio-Inspired Materials Chemistry. *Handbook of Biomineralization*, 2. Wiley-VCH, Weinheim.
- Baeuerlein, E., Epple, M., 2007. Biomineralization in Medicine. *Handbook of Biomineralization*, 3. Wiley-VCH, Weinheim.
- Barbas, C.F., Rosenblum, J.S., Lerner, R.A., 1993. Direct Selection of Antibodies That Coordinate Metals from Semisynthetic Combinatorial Libraries. *Proc. Natl. Acad. Sci. U.S.A.*, 90(14): 6385-6389.
- Baumgartner, J., Bertinetti, L., Widdrat, M., Hirt, A.M., Faivre, D., 2013a. Formation of Magnetite Nanoparticles at Low Temperature: From Superparamagnetic to Stable Single Domain Particles. *Plos One*, 8(3): e57070.
- Baumgartner, J., Carillo, M.A., Eckes, K., Werner, P., Faivre, D., submitted-a. Biomimetic Magnetite Formation: From Biocombinatorial Approaches to Mineralization Effects
- Baumgartner, J. et al., 2013b. Nucleation and growth of magnetite from solution. *Nat. Mater.*, 12(4): 310-314.
- Baumgartner, J., Faivre, D., 2011. Magnetite Biomineralization in Bacteria. In: Müller, W.E.G. (Ed.), *Molecular Biomineralization*. Prog. Mol. Subcell. Biol. Springer, Berlin Heidelberg, pp. 3-27.
- Baumgartner, J. et al., Submitted-b. Magnetite Biomineralization in Magnetotactic Bacteria.
- Baumgartner, J. et al., 2013c. Magnetotactic bacteria form magnetite from a phosphate-rich ferric hydroxide via nanometric ferric (oxyhydr)oxide intermediates. *Proc. Natl. Acad. Sci. U.S.A.*, 110(37): 14883-14888.
- Bazylinski, D.A., Frankel, R.B., 2004. Magnetosome formation in prokaryotes. *Nat. Rev. Microbiol.*, 2: 217-230.

- Bazylinski, D.A., Schübbe, S., 2007. Controlled Biomineralization by and Applications of Magnetotactic Bacteria. In: Laskin, A.I., Sariaslani, S., Gadd G. M. (Eds.), *Advances in Applied Microbiology*. Academic Press, London, pp. 21-62.
- Bell, P.E., Mills, A.L., Herman, J.S., 1987. Biogeochemical Conditions Favoring Magnetite Formation during Anaerobic Iron Reduction. *Appl Environ Microbiol*, 53(11): 2610–2616.
- Benkoski, J.J. et al., 2011. Dipolar organization and magnetic actuation of flagella-like nanoparticle assemblies. *J. Mater. Chem.*, 21(20): 7314-7325.
- Bennet, M. et al., submitted. A microscopy platform for correlative studies of tactic behaviors of microorganisms.
- Bennet, M., Perez-Gonzalez, T., Wood, D., Faivre, D., 2012. Magnetosomes. In: Rehm, B. (Ed.), *Bionanotechnology: Biological Self-assembly and its Applications*. Horizon Scientific Press, pp. 241-272.
- Berg, H.C., 2003. The rotary motor of bacterial flagella. *Ann. Rev. Biochem.*, 72: 19-54.
- Blakemore, R.P., 1975. Magnetotactic Bacteria. *Science*, 190: 377-379.
- Blakemore, R.P., 1982. Magnetotactic Bacteria. *Ann. Rev. Microbiol.*, 36(1): 217-238.
- Borch, T., Masue, Y., Kukkadapu, R.K., Fendorf, S., 2007. Phosphate imposed limitations on biological reduction and alteration of ferrihydrite. *Environ. Sci. Technol.*, 41(1): 166-172.
- Bremholm, M., Felicissimo, M., Iversen, B.B., 2009. Time-Resolved In Situ Synchrotron X-ray Study and Large-Scale Production of Magnetite Nanoparticles in Supercritical Water. *Angew. Chem. Int. Ed.*, 48(26): 4788-4791.
- Brown, S., 1992. Engineered Iron Oxide-Adhesion Mutants of the Escherichia-Coli Phage-Lambda Receptor. *Proc. Natl. Acad. Sci. U.S.A.*, 89(18): 8651-8655.
- Buseck, P.R. et al., 2001. Magnetite morphology and life on Mars. *Proc. Natl. Acad. Sci. U.S.A.*, 98(24): 13490-13495.
- Byrne, M.E. et al., 2010. *Desulfovibrio magneticus* RS-1 contains an iron- and phosphorus-rich organelle distinct from its bullet-shaped magnetosomes. *Proc. Natl. Acad. Sci. U.S.A.*, 107(27): 12263-12268.
- Carballido-Lopez, R., 2006. The bacterial actin-like cytoskeleton. *Microbiol. Mol. Biol. Rev.*, 70(4): 888-+.
- Carillo, M.A., Bennet, M., Faivre, D., 2013. The Interaction of Proteins Associated to the Magnetosome Assembly in Magnetotactic Bacteria as Revealed by Two-Hybrid Two-Photon Excitation Fluorescence Lifetime Imaging Microscopy Förster Resonance Energy Transfer. *J. Phys. Chem. B*, 117(47): 14642-14648.
- Carillo, M.A., Vach, P., Faivre, D., 2012. Magnetic nanoparticles in bacteria. In: Fratzl, P., Dunlop, J.W.C., Weinkamer, R. (Eds.), *Bio-inspired Materials design: Function through Inner Architecture*. Royal Society of Chemistry, Cambridge, pp. in press.
- Carvalho, C., Hickey, S., Faivre, D., Menguy, N., 2009. Formation of magnetite in *Magnetospirillum gryphiswaldense* studied with FORC diagrams. *Earth Planets Space*, 61: 143-145.
- Charilaou, M. et al., 2011a. Evolution of magnetic anisotropy and thermal stability during nanocrystal-chain growth. *Appl. Phys. Lett.*, 99(18): 182504.
- Charilaou, M., Winklhofer, M., Gehring, A.U., 2011b. Simulation of ferromagnetic resonance spectra of linear chains of magnetite nanocrystals. *J. Appl. Phys.*, 109(9): 093903-6.
- Chen, C.-L., Rosi, N.L., 2010. Peptide-Based Methods for the Preparation of Nanostructured Inorganic Materials. *Angew. Chem. Int. Ed.*, 49(11): 1924-1942.
- Cölfen, H., Antonietti, M., 2005. Mesocrystals: Inorganic Superstructures Made by Highly Parallel Crystallization and Controlled Alignment. *Angew. Chem. Int. Ed.*, 44(35): 5576-5591.
- Cornell, R.M., Schwertmann, U., 2003a. *The Iron Oxides*. Wiley-VCH Verlag GmbH & Co. KGaA, Weinheim.
- Cornell, R.M., Schwertmann, U., 2003b. *The iron oxides (Structure, properties, reactions, occurrences and uses)*. Wiley-VCH, Weinheim.
- Dey, A. et al., 2010. The role of prenucleation clusters in surface-induced calcium phosphate crystallization. *Nat. Mater.*, 9(12): 1010-1014.



- Dey, A. et al., 2011. The role of prenucleation clusters in surface-induced calcium phosphate crystallization. *Nat. Mater.*, 9: 1010-1014.
- Draper, O. et al., 2011. MamK, a bacterial actin, forms dynamic filaments in vivo that are regulated by the acidic proteins MamJ and LimJ. *Mol. Microbiol.*, 82(2): 342-354.
- Dreyfus, R. et al., 2005. Microscopic artificial swimmers. *Nature*, 437(7060): 862-865.
- Dunin-Borkowski, R.E. et al., 1998. Magnetic microstructure of magnetotactic bacteria by electron holography. *Science*, 282: 1868-1870.
- Dunlop, D.J., Özdemir, O., 1997. *Rock magnetism: fundamentals and frontiers*. Cambridge Studies in Magnetism. Cambridge University Press, Cambridge, 596 pp.
- Dunlop, J.W.C., Fratzl, P., 2010. Biological Composites. *Ann. Rev. Mater. Res.*, 40(1): 1-24.
- Eder, S.H.K. et al., 2012. Magnetic characterization of isolated candidate vertebrate magnetoreceptor cells. *Proc. Natl. Acad. Sci. U.S.A.*, 109(30): 12022-12027.
- Evans, J.S., 2003. 'Apples' and 'oranges': comparing the structural aspects of biomineral- and ice-interaction proteins. *Curr. Opin. Coll. Interf. Sci.*, 8: 48--54.
- Faivre, D., Böttger, L.H., Matzanke, B.F., Schüler, D., 2007. Intracellular Magnetite Biomineralization in Bacteria Proceeds by a Distinct Pathway Involving Membrane-Bound Ferritin and an Iron(II) Species. *Angew. Chem. Int. Ed.*, 46: 8495-8499.
- Faivre, D., Fischer, A., Garcia-Rubio, I., Mastrogiacomo, G., Gehring, A.U., 2010. The development of cellular magnetic dipoles. *Biophys J.*, 99: 1268-1273.
- Faivre, D., Menguy, N., Guyot, F., Lopez, O., Zuddas, P., 2005. Morphology of nanomagnetite crystals: Implications for formation conditions. *Am. Mineral.*, 90: 1793-1800.
- Faivre, D., Menguy, N., Pósfai, M., Schüler, D., 2008. Environmental parameters affect the physical properties of fast-growing magnetosomes. *Am. Mineral.*, 93: 463-469.
- Faivre, D., Schüler, D., 2008. Magnetotactic Bacteria and Magnetosomes. *Chem. Rev.*, 108(11): 4875-4898.
- Fdez-Gubieda, M.L. et al., 2013a. Magnetite Biomineralization in *Magnetospirillum gryphiswaldense*: Time-Resolved Magnetic and Structural Studies. *ACS Nano*.
- Fdez-Gubieda, M.L. et al., 2013b. Magnetite Biomineralization in *Magnetospirillum gryphiswaldense*: Time-Resolved Magnetic and Structural Studies. *ACS Nano*, 7(4): 3297-3305.
- Fischer, A., Schmitz, M., Aichmayer, B., Fratzl, P., Faivre, D., 2011. Structural purity of magnetite nanoparticles in magnetotactic bacteria. *J. R. Soc. Interface*, 8: 1011-1018.
- Fischer, H. et al., 2008. Ferromagnetic resonance and magnetic characteristics of intact magnetosome chains in *Magnetospirillum gryphiswaldense*. *Earth Planet. Sci. Lett.*, 270(3-4): 200-208.
- Fischer, P., Ghosh, A., 2011. Magnetically actuated propulsion at low Reynolds numbers: towards nanoscale control. *Nanoscale*, 3(2): 557-563.
- Fleet, M.E., 1984. The Structure of Magnetite - 2 Annealed Natural Magnetites, Fe<sub>3</sub>O<sub>4</sub> and Fe<sub>2</sub>.96mg0.04o<sub>4</sub>. *Acta Cryst. C*, 40(SEP): 1491-1493.
- Fleissner, G. et al., 2003. Ultrastructural analysis of a putative magnetoreceptor in the beak of homing pigeons. *Journal of Comparative Neurology*, 458(4): 350-360.
- Frankel, R.B., Bazylinski, D.A., Johnson, M.S., Taylor, B.L., 1997. Magneto-Aerotaxis in Marine Coccoid Bacteria. *Biophys. J.*, 73: 994-1000.
- Frankel, R.B., Blakemore, R., Wolfe, R.S., 1979. Magnetite in Freshwater Magnetotactic Bacteria. *Science*, 203: 1355-1356.
- Frankel, R.B., Blakemore, R.P., 1984. Precipitation of Fe<sub>3</sub>O<sub>4</sub> in Magnetotactic Bacteria *Philosophical Transactions of the Royal Society of London* 567-573.
- Frankel, R.B., Papaefthymiou, G.C., Blakemore, R.P., O'Brien, W., 1983. Fe<sub>3</sub>O<sub>4</sub> Precipitation in Magnetotactic Bacteria. *Biochim. Biophys. Acta*, 763: 147-159.
- Frankel, R.B., Williams, T.J., Bazylinski, D.A., 2007. Magneto-Aerotaxis. In: Schüler, D. (Ed.), *Magnetoreception and magnetosomes in bacteria*. Microbiology Monographs. Springer, Heidelberg, pp. 1-24.

- Fratzl, P., 2007. Biomimetic materials research: what can we really learn from nature's structural materials? *J. R. Soc. Interface*, 4: 1-6.
- Fratzl, P., Weinkamer, R., 2007. Nature's hierarchical materials. *Prog. Mater. Sci.*, 52(8): 1263-1334.
- Friedmann, E.I., Wierzchos, J., Ascaso, C., Winklhofer, M., 2001. Chains of magnetite crystals in the meteorite ALH84001: Evidence of biological origin. *Proc. Natl. Acad. Sci. U.S.A.*, 98(5): 2176-2181.
- Gebauer, D., Volkel, A., Cölfen, H., 2008. Stable Prenucleation Calcium Carbonate Clusters. *Science*, 322(5909): 1819-1822.
- Ghosh, A., Fischer, P., 2009. Controlled Propulsion of Artificial Magnetic Nanostructured Propellers. *Nano Lett.*, 9(6): 2243-2245.
- Goel, A., Vogel, V., 2008. Harnessing biological motors to engineer systems for nanoscale transport and assembly. *Nat. Nanotechnol.*, 3(8): 465-475.
- Gorby, Y.A., Beveridge, T.J., Blakemore, R., 1988. Characterization of the Bacterial Magnetosome Membrane. *J. Bacteriol.*, 170(2): 834-841.
- Grünberg, K., Wawer, C., Tebo B. M., Schüler, D., 2001. A large gene cluster encoding several magnetosome proteins is conserved in different species of magnetotactic bacteria. *Appl. Environ. Microbiol.*, 67(10): 4573-4582.
- Hanzlik, M., Winklhofer, M., Petersen, N., 2002. Pulsed-field-remnance measurements on individual magnetotactic bacteria. *J. Magn. Magn. Mater.*, 248(2): 258-267.
- Hartung, A., , et al., 2007. Labeling of macrophages using bacterial magnetosomes and their characterization by magnetic resonance imaging. *J. Magn. Magn. Mater.*, 311: 454-459.
- Hiratsuka, Y., Miyata, M., Tada, T., Uyeda, T.Q.P., 2006. A microrotary motor powered by bacteria. *Proc. Natl. Acad. Sci. U.S.A.*, 103(37): 13618-13623.
- Hu, Q. et al., 2012. The thermodynamics of calcite nucleation at organic interfaces: Classical vs. non-classical pathways. *Faraday Discuss.*, 159(0): 509-523.
- Jogler, C., Schüler, D., 2009. Genomics, Genetics, and Cell Biology of Magnetosome Formation. *Annu. Rev. Microbiol.*, 63(1): 501-521.
- Jolivet, J.P., Chaneac, C., Tronc, E., 2004. Iron oxide chemistry. From molecular clusters to extended solid networks. *Chem Commun (Camb)*(5): 481-7.
- Katzmann, E., Scheffel, A., Gruska, M., Plitzko, J.M., Schüler, D., 2010. Loss of the actin-like protein MamK has pleiotropic effects on magnetosome formation and chain assembly in *Magnetospirillum gryphiswaldense*. *Mol. Microbiol.*, 77(1): 208-224.
- Kemp, M., Go, Y.-M., Jones, D.P., 2008. Nonequilibrium thermodynamics of thiol/disulfide redox systems: A perspective on redox systems biology. *Free Radical Biology and Medicine*, 44(6): 921-937.
- Kirschvink, J.L., 1992. On the magnetostatic control of crystal orientation and iron accumulation in magnetosomes. *Automed.*, 14: 257-269.
- Klumpp, S., Faivre, D., 2012. Interplay of Magnetic Interactions and Active Movements in the Formation of Magnetosome Chains. *Plos One*, 7(3): e33562.
- Komeili, A., 2007a. Cell Biology of Magnetosome Formation. In: Schüler, D. (Ed.), *Magnetoreception and magnetosomes in bacteria*. Microbiology Monographs. Springer, Heidelberg.
- Komeili, A., 2007b. Molecular Mechanisms of Magnetosome Formation. *Ann. Rev. Biochem.*, 76(1): 351-366.
- Komeili, A., 2012. Molecular mechanisms of compartmentalization and biomineralization in magnetotactic bacteria. *FEMS Microbiol. Rev.*, 36(1): 232-255.
- Komeili, A., Li, Z., Newman, D.K., Jensen, G.J., 2006. Magnetosomes are cell membrane invaginations organized by the actin-like protein MamK. *Science*, 311(5758): 242-245.
- Komeili, A., Vali, H., Beveridge, T.J., Newman, D., 2004. Magnetosome vesicles are present prior to magnetite formation and MamA is required for their activation. *Proc. Natl. Acad. Sci. U.S.A.*, 101(11): 3839-3844.
- Kopp, R.E., Kirschvink, J.L., 2008. The identification and biogeochemical interpretation of fossil magnetotactic bacteria. *Earth Sci. Rev.*, 86(1-4): 42-61.

- Kopp, R.E. et al., 2006a. Ferromagnetic resonance spectroscopy for assessment of magnetic anisotropy and magnetostatic interactions: A case study of mutant magnetotactic bacteria. *J. Geophys. Res.*, 111: B12S25.
- Kopp, R.E. et al., 2006b. Chains, clumps, and strings: Magnetofossil taphonomy with ferromagnetic resonance spectroscopy. *Earth Planet. Sci. Lett.*, 247(1-2): 10-25.
- Körnig, A., Faivre, D., 2012. Magnetic Nanoparticles in Magnetosomes. In: Barnard, A.S., Guo, H. (Eds.), *Nature's Nanostructures*. Pan Stanford, Singapore, pp. 249-271.
- Körnig, A. et al., 2013. Magnetite crystal orientation in magnetosome chains. *Adv. Funct. Mater.*, submitted.
- Kröger, N., Poulsen, N., 2008. Diatoms- From Cell Wall Biogenesis to Nanotechnology. *Annu. Rev. Genet.*, 42(1): 83-107.
- Lang, C., Schüler, D., 2008. Expression of Green Fluorescent Protein Fused to Magnetosome Proteins in Microaerophilic Magnetotactic Bacteria. *Appl. Environ. Microbiol.*, 74(15): 4944-4953.
- Lang, C., Schüler, D., Faivre, D., 2007. Synthesis of Magnetite Nanoparticles for Bio- and Nanotechnology: Genetic Engineering and Biomimetics of Bacterial Magnetosomes. *Macromol. Biosci.*, 7(2): 144-151.
- Laurent, S. et al., 2008. Magnetic Iron Oxide Nanoparticles: Synthesis, Stabilization, Vectorization, Physicochemical Characterizations, and Biological Applications. *Chem. Rev.*, 108(6): 2064-2110.
- Lefèvre, C.T., Bazylinski, D.A., 2013. Ecology, Diversity, and Evolution of Magnetotactic Bacteria. *Microbiol. Mol. Biol. Rev.*, 77(3): 497-526.
- Li, J. et al., 2013. A strong angular dependence of magnetic properties of magnetosome chains: Implications for rock magnetism and paleomagnetism. *Geochem. Geophys. Geosyst.*: n/a-n/a.
- Li, J.H. et al., 2009. Magnetite magnetosome and fragmental chain formation of *Magnetospirillum magneticum* AMB-1: transmission electron microscopy and magnetic observations. *Geophys. J. Int.*, 177(1): 33-42.
- Li, J.H. et al., 2010. Biomineralization, crystallography and magnetic properties of bullet-shaped magnetite magnetosomes in giant rod magnetotactic bacteria. *Earth Planet. Sci. Lett.*, 293(3-4): 368-376.
- Lins, U., Keim, C.N., Evans, F.F., Farina, M., Buseck, P.R., 2007. Magnetite (Fe<sub>3</sub>O<sub>4</sub>) and greigite (Fe<sub>3</sub>S<sub>4</sub>) crystals in multicellular magnetotactic prokaryotes. *Geomicrobiol. J.*, 24(1): 43-50.
- Lins, U., McCartney, M.R., Farina, M., Frankel, R.B., Buseck, P.R., 2005. Habits of Magnetosome Crystals in Coccoid Magnetotactic Bacteria. *Appl. Environ. Microbiol.*, 71(8): 4902-4905.
- Lohse, A. et al., 2011. Functional analysis of the magnetosome island in *Magnetospirillum gryphiswaldense*: the mamAB operon is sufficient for magnetite biomineralization. *PLoS One*, 6(10): e25561.
- Lohße, A. et al., 2011. Functional Analysis of the Magnetosome Island in *Magnetospirillum gryphiswaldense*: The mamAB Operon Is Sufficient for Magnetite Biomineralization. *Plos One*, 6(10): e25561.
- Lowenstam, H.A., 1981. Minerals formed by organisms. *Science*, 211(4487): 1126-1131.
- Lu, A.-H., Salabas, E.L., Schüth, F., 2007. Magnetic Nanoparticles: Synthesis, Protection, Functionalization, and Application. *Angew. Chem. Int. Ed.*, 46(8): 1222-1244.
- Manesh, K.M. et al., 2013. Nanomotor-based biocatalytic patterning of helical metal microstructures. *Nanoscale*, 5(4): 1310-1314.
- Mann, S., 2001. *Biomineralization: Principles and Concepts in Bioinorganic Materials Chemistry*. Oxford Chemistry Masters, 5. Oxford University Press, Oxford, 198 pp.
- Mann, S., Frankel, R.B., Blakemore, R.P., 1984. Structure, morphology and crystal growth of bacterial magnetite. *Nature*, 310: 405-407.
- Mann, S., Sparks, N.H.C., Frankel, R.B., Bazylinski, D.A., Jannasch, H.W., 1990. Biomineralization of ferrimagnetic greigite (Fe<sub>3</sub>S<sub>4</sub>) and iron pyrite (FeS<sub>2</sub>) in a magnetotactic bacterium. *Nature*, 343(6255): 258-261.

- Maratea, D., Blakemore, R.P., 1981. Aquaspirillum-Magnetotacticum Sp-Nov, a Magnetic Spirillum. *Int. J. Syst. Bacteriol.*, 31(4): 452-455.
- Martel, S., 2012. Bacterial microsystems and microrobots. *Biomed. Microdev.*, 14(6): 1033-1045.
- Martel, S., Mohammadi, M., Felfoul, O., Lu, Z., Pouponneau, P., 2009. Flagellated Magnetotactic Bacteria as Controlled MRI-trackable Propulsion and Steering Systems for Medical Nanorobots Operating in the Human Microvasculature. *Int. J. Robot. Res.*, 28(4): 571-582.
- Massart, R., 1981. Preparation of aqueous magnetic liquids in alkaline and acidic media. *IEEE Trans. Magn.*, 17(2): 1247-1248.
- Matsuda, T., Endo, J., Osakabe, N., Tonomura, A., Arii, T., 1983. Morphology and structure of biogenic magnetite particles. *Nature*, 302: 411-412.
- Matsunaga, T., Suzuki, T., Tanaka, M., Arakaki, A., 2007. Molecular analysis of magnetotactic bacteria and development of functional bacterial magnetic particles for nano-biotechnology. *Trends Biotechnol.*, 25(4): 182-188.
- Mavroidis, C., Ferreira, A., 2009. Special Issue on Current State of the Art and Future Challenges in Nanorobotics. *Int. J. Robot. Res.*, 28(4): 419-420.
- Mazzag, B.C., Zhulin, I.B., Mogilner, A., 2003. Model of bacterial band formation in aerotaxis. *Biophysical Journal*, 85(6): 3558-3574.
- Meldrum, F.C., Mann, S., Heywood, B.R., Frankel, R.B., Bazylinski, D.A., 1993. Electron-Microscopy Study of Magnetosomes in a Cultured Coccoid Magnetotactic Bacterium. *Proc. R. Soc. Lond. B*, 251(1332): 231-236.
- Murat, D. et al., 2012. The magnetosome membrane protein, MmsF, is a major regulator of magnetite biomineralization in *Magnetospirillum magneticum* AMB-1. *Mol. Microbiol.*, 85(4): 684-699.
- Murat, D., Quinlan, A., Vali, H., Komeili, A., 2010a. Comprehensive genetic dissection of the magnetosome gene island reveals the step-wise assembly of a prokaryotic organelle. *Proc Natl Acad Sci U S A*, 107(12): 5593-8.
- Murat, D., Quinlan, A., Vali, H., Komeili, A., 2010b. Comprehensive genetic dissection of the magnetosome gene island reveals the step-wise assembly of a prokaryotic organelle. *Proc. Natl. Acad. Sci. U.S.A.*, 107(12): 5593-5598.
- Navrotsky, A., Mazeina, L., Majzlan, J., 2008. Size-Driven Structural and Thermodynamic Complexity in Iron Oxides. *Science*, 319: 1635-1638.
- Nudelman, F., Sommerdijk, N.A.J.M., 2012. Biomineralization as an Inspiration for Materials Chemistry. *Angew. Chem. Int. Ed.*, 51(27): 6582-6596.
- Pak, O.S., Gao, W., Wang, J., Lauga, E., 2011. High-speed propulsion of flexible nanowire motors: Theory and experiments. *Soft Matter*, 7(18): 8169-8181.
- Pan, Y.H. et al., 2009. 3D morphology of the human hepatic ferritin mineral core: New evidence for a subunit structure revealed by single particle analysis of HAADF-STEM images. *J. Struct. Biol.*, 166(1): 22-31.
- Perez-Gonzalez, T., Bennet, M., D., W., D., F., 2012. Magnetosomes. In: A., R.B.H. (Ed.), *Biological self-assembly and its applications* Horizon Scientific, Hethersett, pp. in press.
- Peyer, K.E., Zhang, L., Nelson, B.J., 2013. Bio-inspired magnetic swimming microrobots for biomedical applications. *Nanoscale*, 5(4): 1259-1272.
- Philippe, N., Wu, L.-F., 2010. An MCP-Like Protein Interacts with the MamK Cytoskeleton and Is Involved in Magnetotaxis in *Magnetospirillum magneticum* AMB-1. *J. Mol. Biol.*, 400(3): 309-322.
- Philipse, A.P., Maas, D., 2002. Magnetic Colloids from Magnetotactic Bacteria: Chain Formation and Colloidal Stability. *Langmuir*, 18: 9977-9984.
- Pinney, N., Kubicki, J.D., Middlemiss, D.S., Grey, C.P., Morgan, D., 2009. Density Functional Theory Study of Ferrihydrite and Related Fe-Oxyhydroxides. *Chem. Mater.*, 21(24): 5727-5742.
- Pokroy, B. et al., 2006a. Anisotropic lattice distortions in biogenic calcite induced by intra-crystalline organic molecules. *J. Struct. Biol.*, 155(1): 96-103.

- Pokroy, B., Fitch, A.N., Zolotoyabko, E., 2006b. The microstructure of biogenic calcite: A view by high-resolution synchrotron powder diffraction. *Adv. Mater.*, 18(18): 2363-2368.
- Pokroy, B., Quintana, J.P., Caspi, E.N., Berner, A., Zolotoyabko, E., 2004. Anisotropic lattice distortions in biogenic aragonite. *Nat. Mater.*, 3(12): 900-902.
- Pósfai, M. et al., 2006. Properties of intracellular magnetite crystals produced by *Desulfovibrio magneticus* strain RS-1. *Earth Planet. Sci. Lett.*, 249(3-4): 444-455.
- Pouget, E.M. et al., 2009. The Initial Stages of Template-Controlled CaCO<sub>3</sub> Formation Revealed by Cryo-TEM. *Science*, 323(5920): 1455-1458.
- Pradel, N., Santini, C.-L., Bernadac, A., Fukumori, Y., Wu, L.-F., 2006a. Biogenesis of actin-like bacterial cytoskeletal filaments destined for positioning prokaryotic magnetic organelles. *Proc. Natl. Acad. Sci. U.S.A.*, 103(46): 17485-17489.
- Pradel, N., Santini, C.-L., Bernadac, A., Fukumori, Y., Wu, L.-F., 2006b. Biogenesis of actin-like bacterial cytoskeletal filaments destined for positioning prokaryotic magnetic organelles. *Proceedings of the National Academy of Sciences of the United States of America*, 103(46): 17485-17489.
- Prozorov, T. et al., 2007. Protein-mediated synthesis of uniform superparamagnetic magnetite nanocrystals. *Adv. Funct. Mater.*, 17(6): 951-957.
- Purcell, E.M., 1977. Life at low Reynolds number. *Am. J. Phys.*, 45(1): 3-11.
- Quinlan, A., Murat, D., Vali, H., Komeili, A., 2011. The HtrA/DegP family protease MamE is a bifunctional protein with roles in magnetosome protein localization and magnetite biomineralization. *Mol Microbiol*, 80(4): 1075-87.
- Quintana, C., Cowley, J.M., Marhic, C., 2004. Electron nanodiffraction and high-resolution electron microscopy studies of the structure and composition of physiological and pathological ferritin. *J. Struct. Biol.*, 147(2): 166-178.
- Readman, P.W., Oreilly, W., 1972. Magnetic Properties of Oxidized (Cation-Deficient) Titanomagnetites (Fe, Ti, Block)<sub>3</sub>O<sub>4</sub>. *J. Geomagn. Geoelectr.*, 24(1): 69-&.
- Reddy, L.H., Arias, J.L., Nicolas, J., Couvreur, P., 2012. Magnetic Nanoparticles: Design and Characterization, Toxicity and Biocompatibility, Pharmaceutical and Biomedical Applications. *Chem. Rev.*, 112(11): 5818-5878.
- Richter, M. et al., 2007. Comparative Genome Analysis of Four Magnetotactic Bacteria Reveals a Complex Set of Group-Specific Genes Implicated in Magnetosome Biomineralization and Function. *J. Bacteriol.*, 189(13): 4899-4910.
- Rioux, J.B. et al., 2010. A Second Actin-Like MamK Protein in *Magnetospirillum magneticum* AMB-1 Encoded Outside the Genomic Magnetosome Island. *Plos One*, 5(2): 12.
- Rohrer, J.S., Islam, Q.T., Watt, G.D., Sayers, D.E., Theil, E.C., 1990. Iron environment in ferritin with large amounts of phosphate, from *Azotobacter vinelandii* and horse spleen, analyzed using extended X-ray absorption fine-structure (EXAFS). *Biochemistry*, 29(1): 259-264.
- Rose, J., Manceau, A., Bottero, J.-Y., Masion, A., Garcia, F., 1996. Nucleation and Growth Mechanisms of Fe Oxyhydroxide in the Presence of PO<sub>4</sub> Ions. 1. Fe K-Edge EXAFS Study. *Langmuir*, 12(26): 6701-6707.
- Sanchez, C., Shea, K.J., Kitagawa, S., 2011. Recent progress in hybrid materials science. *Chem. Soc. Rev.*, 40(2): 471-472.
- Scheffel, A., Gärdes, A., Grünberg, K., Wanner, G., Schüler, D., 2008. The major magnetosome proteins MamGFDC are not essential for magnetite biomineralization in *Magnetospirillum gryphiswaldense*, but regulate the size of magnetosome crystals. *J. Bacteriol.*, 190(1): 377-386.
- Scheffel, A. et al., 2006a. An acidic protein aligns magnetosomes along a filamentous structure in magnetotactic bacteria. *Nature*, 440(7080): 110-114.
- Scheffel, A. et al., 2006b. An acidic protein aligns magnetosomes along a filamentous structure in magnetotactic bacteria. *Nature*, 440(7080): 110-115.
- Scheffel, A., Poulsen, N., Shian, S., Kröger, N., 2011. Nanopatterned protein microrings from a diatom that direct silica morphogenesis. *Proc. Natl. Acad. Sci. U.S.A.*

- Scheffel, A., Schueler, D., 2007. The acidic repetitive domain of the *Magnetospirillum gryphiswaldense* MamJ protein displays hypervariability but is not required for magnetosome chain assembly. *Journal of Bacteriology*, 189(17): 6437-6446.
- Scheffel, A., Schüler, D., 2007. The Acidic Repetitive Domain of the *Magnetospirillum gryphiswaldense* MamJ Protein Displays Hypervariability but Is Not Required for Magnetosome Chain Assembly. *J. Bacteriol.*, 189(17): 6437-6446.
- Schleifer, K.-H. et al., 1991a. The genus *Magnetospirillum* gen. nov., description of *Magnetospirillum gryphiswaldense* sp. nov. and transfer of *Aquaspirillum magnetotacticum* to *Magnetospirillum magnetotacticum* comb. nov. *Syst. Appl. Microbiol.*, 14: 379-385.
- Schleifer, K.H. et al., 1991b. The Genus *Magnetospirillum* gen. nov. Description of *Magnetospirillum gryphiswaldense* sp. nov. and Transfer of *Aquaspirillum magnetotacticum* to *Magnetospirillum magnetotacticum* comb. nov. *Systematic and Applied Microbiology*, 14(4): 379-385.
- Schmitz, M., 2010. High-resolution synchrotron x-ray scattering reveals the difference in the ultrastructure of biogenic and abiotic magnetite nanoparticles, Humboldt Universität zu Berlin, Berlin, 40 pp.
- Schüler, D., 1999. Formation of Magnetosomes in Magnetotactic Bacteria. *J. Mol. Microbiol. Biotechnol.*, 1(1): 79-86.
- Schüler, D., 2008. Genetics and cell biology of magnetosome formation in magnetotactic bacteria. *FEMS Microbiol. Rev.*, 32(4): 654-672.
- Schüler, D., Baeuerlein, E., 1996. Iron-limited growth and kinetics of iron uptake in *Magnetospirillum gryphiswaldense*. *Arch. Microbiol.*, 166: 301-307.
- Schüler, D., Baeuerlein, E., 1998. Dynamics of Iron Uptake and Fe<sub>3</sub>O<sub>4</sub> Biomineralization during Aerobic and Microaerobic Growth of *Magnetospirillum gryphiswaldense*. *J. Bacteriol.*, 180(1): 159-162.
- Schüler, D., Köhler, M., 1992. The isolation of a new magnetic spirillum. *Zentralbl. Mikrobiol.*, 147: 150-151.
- Schüler, D., Uhl, R., Baeuerlein, E., 1995. A simple light scattering method to assay magnetism in *Magnetospirillum gryphiswaldense*. *FEMS Microbiol. Lett.*, 132: 139-145.
- Schultheiss, D., Schüler, D., 2003. Development of a genetic system for *Magnetospirillum gryphiswaldense*. *Archives Microbiol.*, 179: 89-94.
- Schwemmer, T., Baumgartner, J., Faivre, D., Börner, H.G., 2012. Peptide-Mediated Nanoengineering of Inorganic Particle Surfaces: A General Route toward Surface Functionalization via Peptide Adhesion Domains. *J. Am. Chem. Soc.*, 134(4): 2385-2391.
- Seto, J. et al., 2012. Structure-property relationships of a biological mesocrystal in the adult sea urchin spine. *Proc. Natl. Acad. Sci. U.S.A.*, 109(10): 3699-3704.
- Siponen, M.I., Adryanczyk, G., Ginet, N., Arnoux, P., Pignol, D., 2012. Magnetochrome: a c-type cytochrome domain specific to magnetotactic bacteria. *Biochem Soc Trans*, 40(6): 1319-23.
- Sitti, M., 2009. Miniature devices: Voyage of the microrobots. *Nature*, 458(7242): 1121-1122.
- Smith, M.J. et al., 2006a. Quantifying the magnetic advantage in magnetotaxis. *Biophysical Journal*, 91(3): 1098-1107.
- Smith, M.J. et al., 2006b. Quantifying the Magnetic Advantage in Magnetotaxis. *Biophys. J.*, 91: 1098-1107.
- Sonkaria, S. et al., 2012. Insight into the Assembly Properties and Functional Organisation of the Magnetotactic Bacterial Actin-like Homolog, MamK. *Plos One*, 7(5): e34189.
- Staniland, S., Ward, B., Harrison, A., van der Laan, G., Telling, N., 2007. Rapid magnetosome formation shown by real-time x-ray magnetic circular dichroism. *Proc. Natl. Acad. Sci. U.S.A.*, 104(49): 19524-19528.
- Stöber, W., Fink, A., Bohn, E., 1968. Controlled growth of monodisperse silica spheres in the micron size range. *J. Coll. Interf. Sci.*, 26(1): 62-69.

- Tanaka, M., Mazuyama, E., Arakaki, A., Matsunaga, T., 2011. Mms6 Protein Regulates Crystal Morphology during Nano-sized Magnetite Biomineralization in Vivo. *J. Biol. Chem.*, 286(8): 6386-6392.
- Tanaka, M. et al., 2006. Origin of magnetosome membrane: Proteomic analysis of magnetosome membrane and comparison with cytoplasmic membrane. *Proteomics*, 6(19): 5234-5247.
- Taoka, A., Asada, R., Wu, L.F., Fukumori, Y., 2007. Polymerization of the actin-like protein MamK, which is associated with magnetosomes. *J. Bacteriol.*, 189(23): 8737-8740.
- Taylor, A.P., Barry, J.C., Webb, R.I., 2001. Structural and morphological anomalies in magnetosomes: possible biogenic origin for magnetite in ALH84001. *J. Microsc.*, 201(1): 84-106.
- Thar, R., Fenchel, T., 2005. Survey of motile microaerophilic bacterial morphotypes in the oxygen gradient above a marine sulfidic sediment. *Applied and Environmental Microbiology*, 71(7): 3682-3691.
- Uebe, R. et al., 2011a. The cation diffusion facilitator proteins MamB and MamM of *Magnetospirillum gryphiswaldense* have distinct and complex functions, and are involved in magnetite biomineralization and magnetosome membrane assembly. *Mol Microbiol*, 82(4): 818-835.
- Uebe, R. et al., 2011b. The cation diffusion facilitator proteins MamB and MamM of *Magnetospirillum gryphiswaldense* have distinct and complex functions, and are involved in magnetite biomineralization and magnetosome membrane assembly. *Mol. Microbiol.*, 82: 818-835.
- Uebe, R. et al., 2010. Deletion of a fur-Like Gene Affects Iron Homeostasis and Magnetosome Formation in *Magnetospirillum gryphiswaldense*. *J. Bacteriol.*, 192(16): 4192-4204.
- Ullrich, S., Kube, M., Schübbe, S., Reinhardt, R., Schüler, D., 2005. A Hypervariable 130-Kilobase Genomic Region of *Magnetospirillum gryphiswaldense* Comprises a Magnetosome Island Which Undergoes Frequent Rearrangements during Stationary Growth. *J. Bacteriol.*, 187(21): 7176-7184.
- Vach, P. et al., 2013. Selecting for function: Solution synthesis of magnetic nanopropellers. *Nano Lett.*, 13(11): 5373-5378.
- Vayssières, L., Chanéac, C., Tronc, E., Jolivet, J.P., 1998. Size Tailoring of Magnetite Particles Formed by Aqueous Precipitation : An Example of thermodynamic Stability of Nanometric Oxide Particles. *J. Col. Interf. Sci.*, 205: 205-212.
- Voegelin, A., Kaegi, R., Frommer, J., Vantelon, D., Hug, S.J., 2010. Effect of phosphate, silicate, and Ca on Fe(III)-precipitates formed in aerated Fe(II)- and As(III)-containing water studied by X-ray absorption spectroscopy. *Geochim. Cosmochim. Acta*, 74(1): 164-186.
- Waldo, G.S. et al., 1995. Formation of the ferritin iron mineral occurs in plastids - an X-ray-absorption spectroscopy study. *Plant Physiology*, 109(3): 797-802.
- Weibel, D.B. et al., 2005. Microoxen: Microorganisms to move microscale loads. *Proc. Natl. Acad. Sci. U.S.A.*, 102(34): 11963-11967.
- Weiner, S., Addadi, L., 2011. Crystallization Pathways in Biomineralization. *Ann. Rev. Mater. Sci.*, 41(1): 21-40.
- Weiss, B.P. et al., 2004a. Ferromagnetic resonance and low-temperature magnetic tests for biogenic magnetite. *Earth Planet. Sci. Lett.*, 224: 73-89.
- Weiss, B.P. et al., 2004b. Magnetic tests for magnetosome chains in Martian meteorite ALH84001. *Proc. Natl. Acad. Sci. U.S.A.*, 101(22): 8281-8284.
- Wilke, M., Farges, F., Petit, P.-E., Brown, G.E., Martin, F., 2001. Oxidation state and coordination of Fe in minerals: An Fe K-XANES spectroscopic study. *Am. Mineral.*, 86(5-6): 714-730.
- Winklhofer, M., Petersen, N., 2007. Paleomagnetism and Magnetic Bacteria. In: Schüler, D. (Ed.), *Magnetoreception and magnetosomes in bacteria*. Microbiology Monographs. Springer, Heidelberg, pp. 255-273.
- Winklhofer, M., Zimanyi, G.T., 2006. Extracting the intrinsic switching field distribution in perpendicular media: A comparative analysis. *J. Appl. Phys.*, 99(8).

- Ye, M.M. et al., 2010. Self-assembly of superparamagnetic magnetite particles into peapod-like structures and their application in optical modulation. *J. Mater. Chem.*, 20(37): 7965-7969.
- Yijun, H., Weijia, Z., Wei, J., Chengbo, R., Ying, L., 2007. Disruption of a fur-like gene inhibits magnetosome formation in *magnetospirillum gryphiswaldense* MSR-1. *Biochem.-Moscow*, 72(11): 1247-+.
- Yuwono, V.M., Burrows, N.D., Soltis, J.A., Penn, R.L., 2010. Oriented Aggregation: Formation and Transformation of Mesocrystal Intermediates Revealed. *J. Am. Chem. Soc.*, 132(7): 2163-2165.
- Zeeshan, M.A. et al., 2013. Iron Nanowires: Graphite Coating of Iron Nanowires for Nanorobotic Applications: Synthesis, Characterization and Magnetic Wireless Manipulation (*Adv. Funct. Mater.* 7/2013). *Adv. Funct. Mater.*, 23(7): 782-782.
- Zhang, C. et al., 2012. Two Bifunctional Enzymes with Ferric Reduction Ability Play Complementary Roles during Magnetosome Synthesis in *Magnetospirillum gryphiswaldense* MSR-1. *J. Bacteriol*, 195(4): 876-85.
- Zhang, L. et al., 2009a. Artificial bacterial flagella: Fabrication and magnetic control. *Appl. Phys. Lett.*, 94(6): 064107-3.
- Zhang, L. et al., 2009b. Characterizing the Swimming Properties of Artificial Bacterial Flagella. *Nano Lett.*, 9(10): 3663-3667.
- Zhang, L., Peyer, K.E., Nelson, B.J., 2011. Artificial bacterial flagella for micromanipulation. *Lab Chip*, 10(17): 2203-2215.
- Ziemniak, S.E., Jones, M.E., Combs, K.E.S., 1995. Magnetite Solubility and Phase Stability in Alkaline Media at Elevated Temperatures. *J. Solution Chem.*, 24(9): 837-877.







## 6. List of publications

### 6.1. Publications in scientific journals or magazines

Hereafter are listed the manuscript published after the doctoral thesis with scientific abstract for publications about primary research. The other works are reviews or “news and views”.

1. Vach P., Brun N., Bennet M., Bertinetti L., Widdrat M., Baumgartner J., Klumpp S., Fratzl P., and **Faivre D.**, Selecting for function: A combinatorial approach to magnetic nanopropellers, *Nano Letters*, available online.

**Abstract:** We show that we can select magnetically steerable nanopropellers from a set of carbon coated aggregates of magnetic nanoparticles using weak homogeneous rotating magnetic fields. The carbon coating can be functionalized, enabling a wide range of applications. Despite their arbitrary shape, all nanostructures propel parallel to the vector of rotation of the magnetic field. We use a simple theoretical model to find experimental conditions to select nanopropellers which are predominantly smaller than previously published ones.

2. Carillo M. A., Bennet M. A., and Faivre D., The interaction of proteins associated to the magnetosome assembly in magnetotactic bacteria as revealed by 2-hybrid 2-photon excitation FLIM-FRET, *The Journal of Physical Chemistry B*, available online.

**Abstract:** Bacteria have recently revealed an unexpected complex level of intracellular organization. Magnetotactic bacteria represent a paradigm with the presence of the magnetosome organelles organized along the magnetosome filament. Although the role of individual magnetosomes-associated proteins has started to be unraveled, their interaction has not been addressed with current state-of-the-art optical microscopy techniques, effectively leaving models of the magnetotactic bacteria protein assembly arguable. Here we report on the use of FLIM-FRET to assess the interaction of MamK (actin-like protein) and MamJ, two magnetosome membrane associated proteins essential to the assembly of magnetosomes in a chain. We used a host organism (*E. coli*) to express eGFP\_MamJ and MamK\_mCherry, the latest expectedly forming a filament. We found that in the presence of MamK, the fluorescence of eGFP\_MamJ is distributed along the MamK filament. FRET analysis using the fluorescence lifetime of the donor, eGFP, revealed a spatial proximity of MamK\_mCherry and eGFP\_MamJ typical of a stable physical interaction between two proteins. Our study effectively led to the reconstruction of part of the magnetotactic apparatus in vivo.

3. Siponen M. I., Legrand P., Widdrat M., Jones S. R., Chang M. C. Y., **Faivre D.**, Arnoux P., and Pignol D. (2013), Structural insight into magnetochrome-mediated magnetite biomineralization, *Nature*, **502**, 681-684.

**Abstract:** Magnetotactic bacteria align along the Earth's magnetic field using an organelle called the magnetosome, a biomineralized magnetite ( $\text{Fe(II)Fe(III)}_2\text{O}_4$ ) or greigite ( $\text{Fe(II)Fe(III)}_2\text{S}_4$ ) crystal embedded in a lipid vesicle. Although the need for both iron(II) and iron(III) is clear, little is known about the biological mechanisms controlling their ratio. Here we present the structure of the magnetosome-associated protein MamP and find that it is built on a unique arrangement of a self-plugged PDZ domain fused to two magnetochrome domains, defining a new class of c-type cytochrome exclusively found in magnetotactic bacteria. Mutational analysis, enzyme kinetics, co-crystallization with iron(II) and an *in vitro* MamP-assisted magnetite production assay establish MamP as an iron oxidase that contributes to the formation of iron(III) ferrihydrite eventually required for magnetite crystal growth *in vivo*. These results demonstrate the molecular mechanisms of iron management taking place inside the magnetosome and highlight the role of magnetochrome in iron biomineralization.

4. Baumgartner J., Morin G., Menguy N., Perez Gonzalez T., Widdrat M., Cosmidis J., and **Faivre D.** (2013), Magnetotactic bacteria form magnetite from a phosphate-rich ferric hydroxide via nanometric ferric (hydr)oxide intermediates, *Proceedings of the National Academy of Science of the USA* **110** (37), 14883-14888.

**Abstract:** The iron oxide mineral magnetite ( $\text{Fe}_3\text{O}_4$ ) is produced by various organisms to exploit magnetic and mechanical properties. Magnetotactic bacteria have become one of the best model organisms for studying magnetite biomineralization, as their genomes are sequenced and tools are available for their genetic manipulation. However, the chemical route by which magnetite is formed intracellularly within the so-called magnetosomes has remained a matter of debate. Here we used X-ray absorption spectroscopy at cryogenic temperatures and transmission electron microscopic imaging techniques to chemically characterize and spatially resolve the mechanism of biomineralization in those microorganisms. We show that magnetite forms through phase transformation from a highly disordered phosphate-rich ferric hydroxide phase, consistent with prokaryotic ferritins, via transient nanometric ferric (oxyhydr)oxide intermediates within the magnetosome organelle. This pathway remarkably resembles recent results on synthetic magnetite formation and bears a high similarity to suggested mineralization mechanisms in higher organisms.

5. Baumgartner J., Dey A., Bomans P. H. H., Le Coadou C., Fratzl P., Sommerdijk N. A. J. M., and Faivre D. (2013), Nucleation and growth of magnetite from solution, *Nature Materials* **12**, 310-314.

**Abstract:** The formation of crystalline materials from solution is usually described by the nucleation and growth theory, where atoms or molecules are assumed to assemble directly from solution. For numerous systems, the formation of the thermodynamically stable crystalline phase is additionally

preceded by metastable intermediates. More complex pathways have recently been proposed, such as aggregational processes of nanoparticle precursors or pre-nucleation clusters, which seem to contradict the classical theory. Here we show by cryogenic transmission electron microscopy that the nucleation and growth of magnetite—a magnetic iron oxide with numerous bio- and nanotechnological applications—proceed through rapid agglomeration of nanometric primary particles and that in contrast to the nucleation of other minerals, no intermediate amorphous bulk precursor phase is involved. We also demonstrate that these observations can be described within the framework of classical nucleation theory.

6. Baumgartner J., Bertinetti L., Widdrat M., Hirt A., and **Faivre D.** (2013) Growth Kinetics of the Formation of Synthetic Magnetite Nanoparticles and its Biological Relevance, *PLoS ONE* **8**, e57070.

**Abstract:** The room temperature co-precipitation of ferrous and ferric iron under alkaline conditions typically yields superparamagnetic magnetite nanoparticles below a size of 20 nm. We show that at pH = 9 this method can be tuned to grow larger particles with single stable domain magnetic (> 20-30 nm) or even multi-domain behavior (> 80 nm). The crystal growth kinetics resembles surprisingly observations of magnetite crystal formation in magnetotactic bacteria. The physicochemical parameters required for mineralization in these organisms are unknown, therefore this study provides insight into which conditions could possibly prevail in the biomineralizing vesicle compartments (magnetosomes) of these bacteria.

7. Baumgartner J., Lesevic P., Kumari M., Halbmaier K., Bennet M., Körnig A., Widdrat M., Andert J., Wollgarten M., Bertinetti L., Strauch P., Hirt A., and **Faivre D.** (2012), From magnetotactic bacteria to hollow spirilla-shaped silica containing a magnetic chain, *RSC Advances* **2** (21), 8007-8009.

**Abstract:** Magnetotactic bacteria produce chains of magnetite nanoparticles, which are called magnetosomes and are used for navigation purposes. We use these cells as a biological template to prepare a hollow hybrid material based on silica and magnetite, and show that the synthetic route is non-destructive as the material conserves the cell morphology as well as the alignment of the magnetic particles. The hybrid material can be resuspended in aqueous solution, and can be shown to orient itself in an external magnetic field. We anticipate that chemical modification of the silica can be used to functionalize the materials surface in order to obtain multifunctional materials with specialized applications, e.g. targeted drug delivery.

8. Murat D., Falahati V., Bertinetti L., Csencsits R., Downing K., **Faivre D.**, and Komeili A. (2012), The magnetosome membrane protein, MmsF, is a major regulator of magnetite biomineralization in *Magnetospirillum magneticum* AMB-1, *Molecular Microbiology* **85** (4), 684-699.

**Abstract:** Magnetotactic bacteria (MTB) use magnetosomes, membrane-bound crystals of magnetite or greigite, for navigation along geomagnetic fields. In *Magnetospirillum magneticum* sp. AMB-1, and

other MTB, a magnetosome gene island (MAI) is essential for every step of magnetosome formation. An 8-gene region of the MAI encodes several factors implicated in control of crystal size and morphology in previous genetic and proteomic studies. We show that these factors play a minor role in magnetite biomineralization *in vivo*. In contrast, MmsF, a previously uncharacterized magnetosome membrane protein encoded within the same region plays a dominant role in defining crystal size and morphology and is sufficient for restoring magnetite synthesis in the absence of the other major biomineralization candidates. In addition, we show that the 18 genes of the *mamAB* gene cluster of the MAI are sufficient for the formation of an immature magnetosome organelle. Addition of MmsF to these 18 genes leads to a significant enhancement of magnetite biomineralization and an increase in the cellular magnetic response. These results define a new biomineralization protein and lay down the foundation for the design of autonomous gene cassettes for the transfer of the magnetic phenotype in other bacteria.

9. Sonkaria S., Fuentes G., Verma C., Narang R., Khare V., Fischer A., and **Faivre D.** (2012), Insight into the assembly properties and functional organisation of the magnetotactic bacterial actin-like homolog MamK, *PLoS ONE* **7** (5), e34189.

**Abstract:** Magnetotactic bacteria (MTB) synthesize magnetosomes, which are intracellular vesicles comprising a magnetic particle. A series of magnetosomes arrange themselves in chains to form a magnetic dipole that enables the cell to orient itself along the Earth's magnetic field. MamK, an actin-like homolog of MreB has been identified as a central component in this organisation. Gene deletion, fluorescence microscopy and *in vitro* studies have yielded mechanistic differences in the filament assembly of MamK with other bacterial cytoskeletal proteins within the cell. With little or no information on the structural and behavioural characteristics of MamK outside the cell, the *mamK* gene from *Magnetospirillum gryphiswaldense* was cloned and expressed to better understand the differences in the cytoskeletal properties with its bacterial homologues MreB and actin. Despite the low sequence identity shared between MamK and MreB (22%) and actin (18%), the behaviour of MamK monitored by light scattering broadly mirrored that of its bacterial cousin MreB primarily in terms of its pH, salt, divalent metal-ion and temperature dependency. The broad size variability of MamK filaments revealed by light scattering studies was supported by transmission electron microscopy (TEM) imaging. Filament morphology however, indicated that MamK conformed to linearly orientated filaments that appeared to be distinctly dissimilar compared to MreB suggesting functional differences between these homologues. The presence of a nucleotide binding domain common to actin-like proteins was demonstrated by its ability to function both as an ATPase and GTPase. Circular dichroism and structural homology modelling showed that MamK adopts a protein fold that is consistent with the 'classical' actin family architecture but with notable structural differences within the smaller domains, the active site region and the overall surface electrostatic potential.

10. Klumpp S., and **Faivre D.** (2012), Interplay of magnetic interactions and active movements in the formation of magnetosome chains, *PLoS ONE* **7** (3), e33562.

**Abstract:** Magnetotactic bacteria assemble chains of magnetosomes, organelles that contain magnetic nano-crystals. A number of genetic factors involved in the controlled biomineralization of

these crystals and the assembly of magnetosome chains have been identified in recent years, but how the specific biological regulation is coordinated with general physical processes such as diffusion and magnetic interactions remains unresolved. Here, these questions are addressed by simulations of different scenarios for magnetosome chain formation, in which various physical processes and interactions are either switched on or off. The simulation results indicate that purely physical processes of magnetosome diffusion, guided by their magnetic interactions, are not sufficient for the robust chain formation observed experimentally and suggest that biologically encoded active movements of magnetosomes may be required. Not surprisingly, the chain pattern is most resembling experimental results when both magnetic interactions and active movement are coordinated. We estimate that the force such active transport has to generate is compatible with forces generated by the polymerization or depolymerization of cytoskeletal filaments. The simulations suggest that the pleiotropic phenotypes of *mamK* deletion strains may be due to a defect in active motility of magnetosomes and that crystal formation in magnetosome vesicles is coupled to the activation of their active motility in *M. gryphiswaldense*, but not in *M. magneticum*.

11. Schwemmer T., Baumgartner J., **Faivre D.**, and Börner H. (2012), Peptide-mediated nanoengineering of inorganic particle surfaces: A general route toward surface functionalization via peptide adhesion domains, *Journal of the American Chemical Society* **134** (4), 2385-2391.

**Abstract:** The peptide-mediated functionalization of inorganic particle surfaces is demonstrated on gadolinium oxide (GdO) particles, revealing specific means to functionalize nano- or microparticles. Phage display screening is exploited to select 12mer peptides, which exhibit sequence-specific adhesion onto surfaces of GdO particles. These peptide adhesion domains are exploited to effectively decorate GdO particles with fluorescently labeled poly(ethylene oxide) (PEO), proving to result in a stable surface modification as shown by significant reduction of protein adsorption by 80%, compared to nonfunctionalized particles. Peptide adhesion and stability of the noncovalent coating are investigated by adsorption/elution experiments and Langmuir isotherms. Fluorescence microscopy, contact angle, and energy dispersive X-ray (EDX) measurements confirmed the sequence specificity of the interactions by comparing adhesion sequences with scrambled peptide sequences. Noncovalent, but specific modification of inorganic particle surfaces represents a generic strategy to modulate functionality and function of nano- or microparticle surfaces.

12. Charilaou M., Sahu K. K., **Faivre D.**, Fischer A., Garcia-Rubio I., and Gehring A. (2011), Evolution of magnetic anisotropy and thermal stability during nanocrystal-chain growth, *Applied Physics Letters* **99**, 182504.

**Abstract:** We compare measurements and simulations of ferromagnetic resonance spectra of magnetite nanocrystal-chains at different growth-stages. By fitting the spectra, we extracted the cubic magnetocrystalline anisotropy field and the uniaxial dipole field at each stage. During the growth of the nanoparticle-chain assembly, the magnetocrystalline anisotropy grows linearly with increasing particle diameter. Above a threshold average diameter of  $D \approx 23$  nm, a dipole field is generated, which then increases with particle size and the ensemble becomes thermally stable.

These findings demonstrate the anisotropy evolution on going from nano to mesoscopic scales and the dominance of dipole fields over crystalline fields in one-dimensional assemblies.

13. Fischer A., Schmitz M., Aichmayer B., Fratzl P., and **Faivre D.** (2011) Structural purity of magnetite nanoparticles in magnetotactic bacteria, *Journal of the Royal Society Interface* **8**, 1011-1018.

**Abstract:** Magnetosome biomineralization and chain formation in magnetotactic bacteria are two processes that are highly controlled at the cellular level in order to form cellular magnetic dipoles. However, even if the magnetosome chains are well characterized, controversial results about the microstructure of magnetosomes were obtained and its possible influence in the formation of the magnetic dipole is to be specified. For the first time, the microstructure of intracellular magnetosomes was investigated using high-resolution synchrotron X-ray diffraction. Significant differences in the lattice parameter were found between intracellular magnetosomes from cultured magnetotactic bacteria and isolated ones. Through comparison with abiotic control materials of similar size, we show that this difference can be associated with different oxidation states and that the biogenic nanomagnetite is stoichiometric, i.e. structurally pure whereas isolated magnetosomes are slightly oxidized. The hierarchical structuring of the magnetosome chain thus starts with the formation of structurally pure magnetite nanoparticles that in turn might influence the magnetic property of the magnetosome chains.

14. **Faivre D.** (2010) Multifunctional materials: Dry but flexible magnetic materials, *Nature Nanotechnology* **5**, 562-563. (News and Views)

15. **Faivre D.**, Fischer A., Garcia-Rubio I., Mastrogiacomo G., and Gehring A. U. (2010) The development of cellular magnetic dipoles, *Biophysical Journal* **99**, 1268-1273.

**Abstract:** Magnetotactic bacteria benefit from their ability to form cellular magnetic dipoles by assembling stable single-domain ferromagnetic particles in chains as a means to navigate along Earth's magnetic field lines on their way to favorable habitats. We studied the assembly of nano-sized membrane-encapsulated magnetite particles (magnetosomes) by ferromagnetic resonance spectroscopy using *Magnetospirillum gryphiswaldense* cultured in a time-resolved experimental setting. The spectroscopic data show that 1), magnetic particle growth is not synchronized; 2), the increase in particle numbers is insufficient to build up cellular magnetic dipoles; and 3), dipoles of assembled magnetosome blocks occur when the first magnetite particles reach a stable single-domain state. These stable single-domain particles can act as magnetic docks to stabilize the remaining and/or newly nucleated superparamagnetic particles in their adjacencies. We postulate that docking is a key mechanism for building the functional cellular magnetic dipole, which in turn is required for magnetotaxis in bacteria.



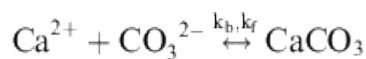
16. Boettger L., **Faivre D.**, Schüler D., Trautwein A. X., and Matzanke B. (2010) Magnetite formation via membrane-bound ferritin and an iron(II) species at the cytoplasmic membrane and in magnetosomes of *Magnetospirillum gryphiswaldense*, *Journal of Physics: Conference Series* **217**, 012020.

**Abstract:** Growth and cell fractions of the magnetic bacterium *Magnetospirillum gryphiswaldense* were studied by Mössbauer spectroscopy. In isolated magnetosomes only magnetite particles were observed. The membrane fraction of *Magnetospirillum gryphiswaldense* contains a ferritin-like component and a Fe<sup>2+</sup> species and also magnetite particles smaller than those observed in the magnetosomes fraction. In the cytosol only ferritin was identified.

17. Lopez O., Zuddas P., and **Faivre D.** (2009) The influence of temperature and seawater composition on calcite crystal growth mechanisms and kinetics: Implications for Mg incorporation in calcite lattice, *Geochimica et Cosmochimica Acta* **73** (2), 337-347.

**Abstract:** The composition of carbonate minerals formed in past and present oceans is assumed to be significantly controlled by temperature and seawater composition. To determine if and how temperature is kinetically responsible for the amount of Mg incorporated in calcite, we quantified the influence of temperature and specific dissolved components on the complex mechanism of calcite precipitation in seawater. A kinetic study was carried out in artificial seawater and NaCl–CaCl<sub>2</sub> solutions, each having a total ionic strength of 0.7 M. The constant addition technique was used to maintain [Ca<sup>2+</sup>] at 10.5 mmol kg<sup>-1</sup> while [CO<sub>3</sub><sup>2-</sup>] was varied to isolate the role of this variable on the precipitation rate of calcite.

Our results show that the overall reaction of calcite precipitation in both seawater and NaCl–CaCl<sub>2</sub> solutions is dominated by the following reaction:



where  $k_f$  and  $k_b$  are the forward and backward reaction rate constants, respectively, while the net precipitation rate  $R$ , can be described at any temperature by

$$R = k_f (a_{\text{Ca}^{2+}})^{n_1} (a_{\text{CO}_3^{2-}})^{n_2} - k_b$$

or in its logarithmic form

$$\text{Log}(R + k_b) = \text{Log} K_f + n_2 \text{Log}[\text{CO}_3^{2-}]$$

where  $n_i$  are the partial reaction orders with respect to the participating ions,  $a$  the ion activity,  $\gamma$  the activity coefficients, and  $K_f = k_f (a_{\text{Ca}^{2+}})^{n_1} (\gamma \text{CO}_3^{2-})^{n_2}$  is a constant at a given temperature.

We find that, irrespective of the presence of Mg, SO<sub>4</sub>, and other specific seawater components known calcite reaction rate inhibitors, the partial reaction order with respect to carbonate ion concentration changes from 2 to 5 while the rate constant  $K_f$ , increases by 3–4 orders of magnitude when temperature varies from 5 to 70 °C. The observed variations of the kinetic mechanism resulting from the temperature changes are correlated with the variable amount of Mg incorporated in the

formed calcites. Moreover, at a given temperature, the increase in the saturation state enhances the rate of calcite precipitation without influencing the reaction mechanism and without changing the amount of Mg incorporated in the growing lattice.

Thus, the results of this experimental study are consistent with present-day abiotic marine carbonates where low-Mg calcite cements are mainly associated with cool water while high-Mg carbonates are dominantly found in warm-water environments. This suggests that the apparent inverse relationship between the global average paleo-temperature and the Mg/Ca ratio in past formed marine carbonate may correspond to major changes in seawater saturation state or (Mg/Ca) ratios that in turn should reflect significant changes in the relative seawater geochemical cycles of these cations.

18. Carvallo C., Hickey S., **Faivre D.**, and Menguy N. (2009) Formation of magnetite in *Magnetospirillum gryphiswaldense* studied with FORC diagrams, *Earth, Planets and Space* **61** (1), 143-150.

**Abstract:** In order to study the formation of magnetite in magnetotactic bacteria, FORC diagrams were measured on a set of cultured *Magnetospirillum gryphiswaldense*, following an assay in which the iron uptake is used only for magnetite formation and not for cell growth. This enabled us to follow the magnetite formation independently of growth. The FORC diagrams showed a clear evolution from a size-distribution with a majority of superparamagnetic grains, to a distribution dominated by stable, single-domain grains, but still containing some superparamagnetic particles. TEM observations confirm this evolution. According to the saturation isothermal remanent magnetization cooling and warming curves, the Verwey transition can only be seen in the most mature samples, and slightly below 120 K. This suggests that the samples may have suffered from some partial oxidation.

19. **Faivre D.** and Schüler D. (2008) Magnetotactic Bacteria and Magnetosomes, *Chemical Reviews* **108** (11), 4875-4898. ([Review](#))

20. **Faivre D.**, Menguy N., Pósfai M., and Schüler D. (2008) Environmental parameters affect the physical properties of fast-growing magnetosomes, *American Mineralogist* **93**, 463-469.

**Abstract:** Magnetotactic bacteria are known to mediate the formation of intracellular magnetic nanoparticles in organelles called magnetosomes. These magnetite crystals are formed through a process called biologically controlled mineralization, in which the microorganisms exert a strict control over the formation and development of the mineral phase. By inducing magnetite nucleation and growth in resting, Fe-starved cells of *Magnetospirillum gryphiswaldense*, we have followed the dynamics of magnetosome development. By studying the properties of the crystals at several steps of maturity, we observed that freshly induced particles lacked a well-defined morphology. More surprisingly, although the mean particle size of mature magnetosomes is similar to that of magnetosomes formed by constantly growing and Fe-supplemented bacteria, we found that other physical properties such as crystal-size distribution, aspect ratio, and morphology significantly differ.

Correlating these results with measurements of Fe uptake rates, we suggest that the expression of different faces is favored for different growth conditions. These results imply that the biological control over magnetite biomineralization by magnetotactic bacteria can be disturbed by environmental parameters. Specifically, the morphology of magnetite crystals is not exclusively determined by biological intervention through vectorial regulation at the organic boundaries or by molecular interaction with the magnetosome membrane, but also by the rates of Fe uptake. This insight may contribute to better define biomarkers and to an improved understanding of biomineralizing systems.

21. **Faivre D.**, Boettger L., Matzanke B., and Schüler D. (2007) Intracellular magnetite biomineralization in bacteria proceeds via a distinct pathway involving membrane-bound ferritin and ferrous iron, *Angewandte Chemie International Edition* **46**, 8495-8499 and *Angewandte Chemie* **119**, 8647-8652.

**Abstract:** A time-resolved study of magnetite formation in magnetotactic bacteria has shown that magnetite biomineralization proceeds first by coprecipitation of  $\text{Fe}^{2+}$  and  $\text{Fe}^{3+}$  ions and then via small magnetite crystallites (see picture) within invaginating magnetosomes associated with the cell membrane, which further develop into mature crystals after magnetosome vesicles are released from the cell membrane.

22. Lang C., Schüler D., and **Faivre D.** (2007) Synthesis of Magnetite Nanoparticles for Bio- and Nanotechnology: Genetic Engineering and Biomimetics of Bacterial Magnetosomes, *Macromolecular Bioscience* **7**, 144-151. ([Feature Article](#))

23. Scheffel A., Gruska M., **Faivre D.**, Linaroudis A., Plitzko J. M., and Schüler D. (2006) An acidic protein aligns magnetosomes along a filamentous structure in magnetotactic bacteria, *Nature* **440** (7080), 110-114.

**Abstract:** Magnetotactic bacteria are widespread aquatic microorganisms that use unique intracellular organelles to navigate along the Earth's magnetic field. These organelles, called magnetosomes, consist of membrane-enclosed magnetite crystals that are thought to help to direct bacterial swimming towards growth-favouring microoxic zones at the bottom of natural waters. Questions in the study of magnetosome formation include understanding the factors governing the size and redox-controlled synthesis of the nano-sized magnetosomes and their assembly into a regular chain in order to achieve the maximum possible magnetic moment, against the physical tendency of magnetosome agglomeration. A deeper understanding of these mechanisms is expected from studying the genes present in the identified chromosomal 'magnetosome island', for which the connection with magnetosome synthesis has become evident. Here we use gene deletion in *Magnetospirillum gryphiswaldense* to show that magnetosome alignment is coupled to the presence of the *mamJ* gene product. MamJ is an acidic protein associated with a novel filamentous structure, as revealed by fluorescence microscopy and cryo-electron tomography. We suggest a mechanism in which MamJ interacts with the magnetosome surface as well as with a cytoskeleton-like structure.

According to our hypothesis, magnetosome architecture represents one of the highest structural levels achieved in prokaryotic cells.

24. Hirt A. M., Brem F., Hanzlik M., and **Faivre D.** (2006) Anomalous Magnetic Properties of Brain Tissue at Low Temperature: 50 K Anomaly, *Journal of Geophysical Research* **111**, B12S06.

**Abstract:** A low-coercivity phase, identified as magnetite and/or maghemite, is the main iron oxide in brain tissue. Measurement of susceptibility as a function of temperature ( $\chi - T$ ) in brain tissue samples does not show a Verwey transition but instead shows a perturbation around 50 K. A susceptibility anomaly has been reported at this temperature in several studies of multidomain magnetite crystals, which, however, also display a Verwey transition. We have investigated the magnetic characteristics of this 50 K anomaly further in brain and tumor tissue. The magnetic measurements consist of  $\chi - T$  curves, measured after cooling in zero field (ZFC) or in a field (FC), as well as hysteresis loops. The 50 K anomaly is expressed as a bump in  $\chi - T$  curves over a 20 K temperature range, with a peak between 44 and 58 K. The magnetic intensity of the samples is weak; however, the anomaly signal is an order of magnitude larger than known effects related to the magnetic ordering of oxygen at 43 K. A phase transition, or magnetic ordering of another phase, does not seem a likely explanation, because both the ZFC and FC curves follow the perturbation, rather than showing a bifurcation at peak susceptibility. This explanation also precludes magnetic blocking of a superparamagnetic component. Hysteresis loops at temperature of the peak perturbation show a splitting of the descending and ascending limbs at the maximum starting field. The magnetic behavior observed in these experiments is consistent with a change in electron activity.

## 6.2. Book chapters

1. Zuddas P., **Faivre D.**, Duhamel J.-R. (2012) Magnetite minerals in the Human brain : what is their role, in *Medical Geochemistry* (ed. P. Censi), 91-99, Springer, Heidelberg.
2. Carillo M. A., Vach P., and **Faivre D.** (2012) Magnetic nanoparticles in bacteria, in *Bio-inspired Materials design: Function through Inner Architecture* (ed. P. Fratzl, J.W.C. Dunlop, and R. Weinkamer) 235-255, RSC Publishing, Cambridge.
3. Perez-Gonzalez T., Bennet M., Wood D. and **Faivre D.** (2012) Magnetosomes, in *Biological self-assembly and its applications* (ed. B. H. A. Rehm), 241-272, Horizon Scientific Press, Hethersett.
4. Körnig A., and **Faivre D.** (2012) Nanoparticles in magnetotactic bacteria, in *Nature's Nanostructures* (ed. A.S. Barnard and H. Guo), 249-271, Pan Stanford Publishing, Singapore.
5. Baumgartner J., and **Faivre D.** (2011) Magnetite Biomineralization in Bacteria, in *Progress in Molecular and Subcellular Biology* (Vol. 30), *Molecular Biomineralization: Aquatic Organisms Forming Extraordinary Materials* (ed. W.E.G. Müller), 3-27, Springer, Heidelberg.

6. **Faivre D.** (2007) Biomimetic Formation of Magnetite Nanoparticles, in *Handbook of Biomineralization (Vol. 2): Biomimetic and Bio-inspired Materials Chemistry* (ed. E. Bäuerlein and P. Behrens), 159-172, Wiley-VCH, Weinheim.
7. **Faivre D.** and Zuddas P. (2007) Mineralogical and isotopic properties of biogenic nanocrystalline magnetites, in *Microbiology Monographs (Vol. 3), Magnetoreception and Magnetosomes in Bacteria* (ed. D. Schüler), 175-196, Springer, Heidelberg.